

# **Intensity dynamics of slow-inversion lasers**

**Proefschrift**

ter verkrijging van  
de graad van Doctor aan de Universiteit Leiden,  
op gezag van de Rector Magnificus Dr. W. A. Wagenaar,  
hoogleraar in de faculteit der Sociale Wetenschappen,  
volgens besluit van het College voor Promoties  
te verdedigen op donderdag 21 november 2002  
te klokke 14.15 uur

door

**Yngve Lien**

geboren te Trondheim, Noorwegen op 26 oktober 1974

**Promotiecommissie:**

Promotor:	Prof. dr. J. P. Woerdman
Copromotores:	Dr. M. P. van Exter
	Dr. N. J. van Druten
Referent:	Prof. dr. K-J. Boller
Leden:	Dr. E. R. Eliel
	Prof. dr. D. Lenstra
	Prof. dr. G. Nienhuis
	Prof. dr. P. H. Kes

The work presented in this book is a part of the research programme of “Stichting voor Fundamenteel Onderzoek der Materie” (FOM), which is financially supported by the “Nederlandse Organisatie voor Wetenschappelijk Onderzoek” (NWO).

# Contents

---

<b>1</b>	<b>Introduction</b>	<b>3</b>
<b>2</b>	<b>Laser quantum noise</b>	<b>5</b>
2.1	Introduction . . . . .	5
2.2	The laser classes . . . . .	5
2.3	Rate equations and relaxation oscillations . . . . .	6
2.4	Extreme class B lasers . . . . .	7
<b>3</b>	<b>Nd<sup>3+</sup>:YVO<sub>4</sub> characteristics</b>	<b>9</b>
3.1	Spectroscopic properties . . . . .	9
3.2	Parameter nomenclature . . . . .	10
3.3	Measurement of inversion decay . . . . .	10
3.4	Pumping of Nd <sup>3+</sup> :YVO <sub>4</sub> crystals . . . . .	12
3.5	Birefringence and temperature . . . . .	13
3.6	The effect of temperature on gain . . . . .	15
3.7	Overview Nd <sup>3+</sup> :YVO <sub>4</sub> characteristics . . . . .	17
<b>4</b>	<b>The thresholdless laser</b>	<b>19</b>
4.1	Introduction . . . . .	19
4.2	The threshold definition . . . . .	20
4.3	Thresholdless oscillation . . . . .	21
4.4	The slow inversion condition . . . . .	23
4.5	Damping due to the lower-level decay . . . . .	24
4.6	Noise sources . . . . .	26
4.7	Experimental setup . . . . .	26
4.8	Experimental Results: Thresholdless oscillations . . . . .	28
4.9	Experimental results: Changing parameters . . . . .	31
4.10	Discussion and conclusion . . . . .	32
4.11	Appendix . . . . .	34
<b>5</b>	<b>Photon statistics</b>	<b>37</b>
5.1	Background . . . . .	37
5.2	The intensity statistics . . . . .	38
5.3	The pseudo energy . . . . .	39
5.4	Setup . . . . .	39
5.5	Experimental results . . . . .	41
5.6	Discussion and conclusion . . . . .	41
5.7	Acknowledgements . . . . .	43
<b>6</b>	<b>The laser as a Toda oscillator</b>	<b>45</b>

## 2 CONTENTS

---

6.1	Introduction . . . . .	45
6.2	The “anharmonic” oscillator . . . . .	46
6.3	Pseudo energy . . . . .	47
6.4	Damping and oscillation rate . . . . .	49
6.5	The setup and experimental parameters . . . . .	49
6.6	Experimental results . . . . .	51
6.7	Concluding discussion . . . . .	55
<b>7</b>	<b>Ring modes -Combining gain and index guiding</b>	<b>57</b>
7.1	Introduction . . . . .	57
7.2	Theoretical model . . . . .	58
7.3	Mirror reflectivity and guiding . . . . .	61
7.4	Experimental setup . . . . .	63
7.5	Results . . . . .	65
7.6	Discussion . . . . .	73
7.7	Summary and Conclusions . . . . .	75
<b>8</b>	<b>Excess noise due to combined gain and index guiding</b>	<b>77</b>
8.1	Introduction . . . . .	77
8.2	Experimental configuration . . . . .	78
8.3	Laser modes and wave guiding . . . . .	80
8.4	Self pulsing at mode crossings . . . . .	84
8.5	Excess quantum noise . . . . .	86
8.6	Concluding discussion . . . . .	89
	<b>Bibliography</b>	<b>91</b>
	<b>Samenvatting</b>	<b>95</b>
	<b>Sammendrag</b>	<b>99</b>
	<b>Curriculum Vitae</b>	<b>103</b>
	<b>Acknowledgements</b>	<b>105</b>

# Chapter 1

---

## Introduction

Quantum noise is due to the discrete nature of the energy-carrying particles. In lasers, this noise source takes the form of spontaneous emission photons, whose random nature causes both phase and intensity fluctuations. Although these fluctuations are relatively small, the near absence of thermal noise in lasers makes quantum noise the primary source of intensity noise as well as phase noise (this phase noise sets the Schawlow-Townes frequency linewidth of the emitted light). The weakness of the thermal noise is due to the low frequency nature of thermal radiation as compared to the oscillation frequencies of common lasers. As given by Planck's law, the number of thermal photons in each mode  $1/(e^{h\nu/kT} - 1)$  becomes very small once  $kT$  drops below  $h\nu$ ; conversely, there is always *one* quantum noise photon in a laser mode. This is a fundamental noise limit that cannot be removed by cooling or by vibrational stabilisation such as in the case of thermal or vibrational noise. However, since the number of noise photons is always equal to one, its effect will depend on the total number of photons in the cavity and hence the laser size. As a result, small lasers show a tendency towards more fluctuations.

In this thesis we address the effects of quantum noise on lasers with slow inversion decay. These lasers are known as class B lasers and they show very different dynamic properties from class A lasers. While the latter laser class has inversion decay rates that are fast enough to be adiabatically eliminated, the relatively slow inversion of class B lasers allows for quantum-noise-driven relaxation oscillations. These oscillations become particularly extreme in the case of very small lasers because of the increased effect of quantum noise (see also chapter 2). Interestingly, owing to the continuing trend of miniaturisation in optoelectronics, these small devices are becoming more and more commonplace. We will therefore focus on quantum noise in these extreme class B lasers where the fluctuations can be as large as the average intensity (see chapter 4).

The class B laser class is probably the largest of the laser classes. One typical example of this group, namely the semiconductor laser, is found in all kinds of devices from communication systems to sensing applications. In such applications, the presence of noise can be highly adverse since it reduces the attainable data transfer rate or the sensitivity of spectroscopic measurements. To counteract these effects, a good understanding of class B dynamics may be critical.

To study class B lasers, we have chosen to use  $\text{Nd}^{3+}:\text{YVO}_4$  (Neodymium doped Yttrium Vanadate) crystals for use as gain medium. These crystals lend themselves well to very small systems because of their large absorption cross-section at the pump wavelength so that small crystals can furnish relatively large gain, even when pumped with low power pumps. In addition, at  $77 \mu\text{s}$  (see chapter 3), the upper level decay rate of  $\text{Nd}^{3+}:\text{YVO}_4$  is extremely

slow as compared to the decay rate in semiconductor lasers, which is typically 1 ns. This makes it relatively easy to use  $\text{Nd}^{3+}:\text{YVO}_4$  crystals to build lasers with the desired class B properties. From an instrumental point of view, another advantage is that the slow dynamics of the system simplifies the experiment greatly when compared, for instance, to the case of a semiconductor laser.

To put this thesis into context, all the work described here was conducted in the Quantum Optics group at Leiden University. The group has been involved with quantum noise for a number of years but most of the work has been concentrated on the phase diffusion of laser light. This thesis, on the other hand, only concerns itself with the intensity noise.

Several of this thesis' chapters correspond to independently published articles, which although written as separate entities, are presented here as parts of a whole. As a consequence, some aspects will be repeated in several of the chapters.

*Chapter 2* gives a brief discussion of the quantum noise and its effect on lasers with slow inversion (class B lasers). We will introduce the rate equations and link them to the relaxation oscillations.

*Chapter 3* will introduce the reader to the properties of the  $\text{Nd}^{3+}:\text{YVO}_4$  laser. In particular, we will focus on heating and birefringence properties as well as absorption and emission.

In *Chapter 4* we consider the definition of a laser threshold and we show how the slow inversion decay of the  $\text{Nd}^{3+}:\text{YVO}_4$  laser can lead to some surprising threshold characteristics which are usually only seen in microlasers with a few modes. While laser output does still show a sudden increase at threshold, the output remains very noisy for a laser of its size. The starting point for our analysis is the rate equations, which we linearise to produce a simple but powerful model of the dynamics.

*Chapter 5* examines the photon statistics of a slow-inversion laser. Because of its noisy behaviour, such a laser display quite different statistics from its more quiet class A laser counterpart with fast inversion decay. Our experimental data is compared with a model based on the Toda oscillator that is intrinsically nonlinear.

*Chapter 6* makes use of the Toda oscillator model to go beyond the framework of linearisation of chapter 4 to study such properties as the anharmonicity of the relaxation oscillations and the effect of the oscillation amplitude on the oscillation frequency.

*Chapter 7* pertains to a slightly different subject, namely the gain and index guiding in a  $\text{Nd}^{3+}:\text{YVO}_4$  chip. We will focus on the case where the two guiding effects become equally large. Intriguingly, this guiding can give rise to a far field modal profile that has zero intensity in the middle and a near-Gaussian shape in the near field. This is in contrast to "normal" Gaussian modes, which are similar in the far and near fields. The experimental configuration described in this chapter is commonly found in commercial solid state systems.

*Chapter 8* discusses the consequences of mixed guiding on the noise properties. Here we observe large increases in intensity fluctuations when tuning the laser towards mode crossings. A related increase in relaxation oscillation damping shows that this is due to excess noise.

## Chapter 2

---

### Laser quantum noise

*Fluctuations in the emitted light of lasers is caused by spontaneous emission photons, a form of quantum noise. Here, we review the quantum noise concept and its effect on the various laser classes. Our focus is on lasers with strong class B properties, whose display of strong relaxation-oscillation behaviour is directly linked to their slow inversion decay.*

#### 2.1 Introduction

Quantum noise is present in all lasers, but its effect is largest in lasers with small cavities. This is due to the fact that there is on average exactly one spontaneous emission photon in the lasing mode above threshold, independent of laser size (this photon is often known as the “extra photon” since it is the only photon emitted through spontaneous emission [1]). To compare, the number of *stimulated* emission photons  $n$  in the laser increases with size:

$$n = \frac{1}{2\beta} \left[ (M - 1) + \sqrt{(M - 1)^2 + 4\beta M} \right], \quad (2.1)$$

where  $M$  is the pump intensity normalised by the threshold value. The fraction of spontaneous emission going into the lasing mode,  $\beta$ , is the inverse of the number of spontaneous emission modes  $p$ . The connection to size is straightforward as  $p$  is proportional to the volume of the laser cavity [2].

Spontaneous emission affects the phase as well as the intensity of the laser since the spontaneously emitted photons do not have the same phase as the photons in the lasing mode. Figure 2.1 shows a vector diagram with the optical electric field of the laser. While any perturbation tangential to the circle perturbs the phase of the intra-cavity field, the perturbations normal to the circle affects the intensity. Because the laser dynamics are independent of the optical phase, this phase will perform an undamped random walk around the circle in Fig. 2.1, (resulting in the Schawlow-Townes linewidth). The intensity perturbations, however, are driven back to equilibrium, giving rise to relaxation oscillations in the case of weak damping. In this thesis we concentrate on the intensity fluctuations.

#### 2.2 The laser classes

It is often convenient to group the various lasers into different classes, where each set has a few properties in common [3, 4]. In lasers, the defining characteristics of a laser class are usually the relative sizes of the following decay rates: the decay of the upper lasing level  $\gamma_1$ ,

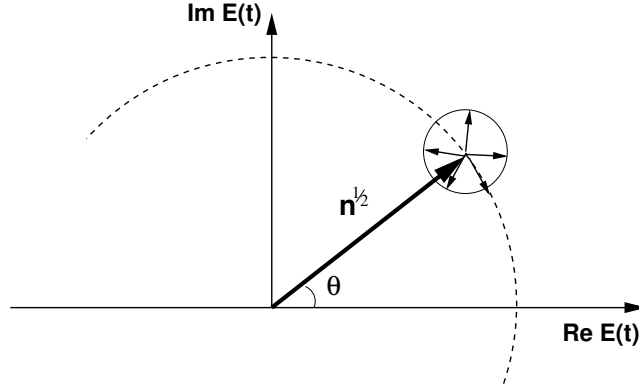


**Figure 2.1:** Figure showing the effect of spontaneous emission on the optical field. As indicated by the small arrows and the circle, spontaneous emission leads to a perturbation of one unit in any direction. In these units the amplitude of the optical field is  $\sqrt{n}$ , while  $\theta$  is the phase.

the decay of the atomic polarisation  $\gamma_{\perp}$ , and the cavity decay rate  $\Gamma_c$  (note that, as discussed in section 3.2, this naming convention tends to differ between articles and publications). In both class A and class B lasers,  $\gamma_{\perp}$  is much faster than the other cavity parameters like the cavity decay rate, and the atomic polarisation can therefore be adiabatically eliminated. This is the good cavity approximation. In class A lasers also the inversion can be adiabatically eliminated so that the dynamics can be formulated in terms of the photon number only [3]. Class B lasers, on the other hand, have photon and inversion numbers that couple to give rise to relaxation oscillations. In addition to class A and class B lasers, more exotic lasers such as the class C laser exists. In this type of laser, all three parameters  $\gamma_1$ ,  $\gamma_{\perp}$  and  $\Gamma_c$  are approximately equally large, allowing for very complex or even chaotic behaviour [4].

### 2.3 Rate equations and relaxation oscillations

As mentioned above, quantum noise leads to relaxation oscillations in class B lasers. These oscillations are described using the laser intensity rate equations to which a few approximations have been applied. One (very good) assumption is that the laser is operated in the good cavity regime. Another assumption is that the laser medium ( $\text{Nd}^{3+}:\text{YVO}_4$  in our case) is a perfect four-level medium; in this case the lower level population can be neglected. The rate equations are now written as

$$\dot{n} = -\Gamma_c n + \beta\gamma_1 N n + N\beta\gamma_1 + f_n, \quad (2.2a)$$

$$\dot{N} = P - \gamma_1 N - \beta\gamma_1 N n, \quad (2.2b)$$

where  $n$  is the intra-cavity photon number,  $N$  is the inversion and  $P$  is the pump rate.  $\beta$  is the fraction of spontaneous emission that goes into the lasing mode. Both  $\Gamma_c$  and  $\gamma_1$  are defined above. The term  $f_n$  in Eq. 2.2a satisfies  $\langle f_n(t)f_n(t') \rangle = 2\beta\gamma_1 N n \delta(t-t')$  in the Langevin description of the quantum noise. The inversion noise source  $f_N$  can be assumed



to be negligible because of the low frequency of this noise contribution [5]. Note that in class A lasers, the adiabatic elimination sets the inversion term  $\dot{N}$  equal to zero.

It is the coupling of the two rate equations 2.2a and 2.2b that gives rise to relaxation oscillations. To find the rate of these oscillations, the photon number and inversion are rewritten in terms of the deviation from the steady state values  $n_0$  and  $N_0$  (these values are both found by setting  $\dot{n}$  and  $\dot{N}$  equal to zero, while  $N_0 = (\Gamma_c n_0)/(\beta\gamma_1(n_0 + 1))$ ,  $n_0$  is defined by Eq. 2.1, i.e.  $n = n_0 + \delta n$  and  $N = N_0 + \delta N$ . Thus when linearising about steady state,

$$\dot{\delta n} = -\gamma_n \delta n + \gamma_1 \beta (n_0 + 1) \delta N + f_n, \quad (2.3a)$$

$$\dot{\delta N} = -\gamma_1 N_0 \beta \delta n - \gamma_N \delta N, \quad (2.3b)$$

where  $\gamma_N = \gamma_1(1 + \beta n_0)$  is known as the inversion damping. It is noteworthy that the photon damping  $\gamma_n = \Gamma_c/(n_0 + 1)$  has its origin in the spontaneous emission, which is, as described above, also the driving force of the relaxation oscillations. Usually this damping is quite weak above threshold, but in the case of very slow inversion decay, its impact will nevertheless be significant due to the weakness of the inversion damping.

Using the linearised rate equations of Eq. 2.3 we obtain the noise spectrum by performing a Fourier transform on the two equations and by inverting the resulting matrix,

$$\langle \delta n^2(\omega) \rangle = \frac{2(\omega^2 + \gamma_N^2)N\beta\gamma_1 n_0}{(\omega_{ro}^2 + \gamma_n\gamma_N - \omega^2)^2 + 4\omega^2\gamma_{ro}^2}, \quad (2.4)$$

where  $\langle \delta n^2(\omega) \rangle$  is the double-sided spectral density of the intensity fluctuations;  $\gamma_{ro}$  and  $\omega_{ro}$  are the decay and oscillation rates of the relaxation oscillations respectively. For a more thorough discussion, see chapter 4.

## 2.4 Extreme class B lasers

Even though relaxation oscillations are observed in *all* class B lasers, they are usually weak as the oscillation damping tends to be strong. However, once lasers are made smaller, the fraction of spontaneous emission into the lasing mode  $\beta$  increases and the laser soon reaches the limit

$$\gamma_1 \lesssim \Gamma_c \beta, \quad (2.5)$$

where the inversion damping rate becomes as weak as the typical photon damping rate, allowing for very deep anharmonic oscillations (this is discussed in chapters 3-6).

Another interesting aspect of this regime are the threshold characteristics. In most lasers the threshold is very clearly defined as the point where output power increases sharply with an accompanying sharp drop in the noise levels. This bears some similarities to the very smallest cavities with only a few modes (our lasers in comparison have approximately  $10^5$  modes) where the threshold is ill-defined both intensity- and noise-wise. In extreme class B lasers however, we do see the clear intensity threshold but the noise remains very high until far above threshold. This is discussed in more detail in chapter 4.

It is the dynamics of these extreme class B lasers that is the main theme of this thesis. In the following chapters we will not only discuss the effect of slow inversion decay, but also the generation of excess quantum noise in  $\text{Nd}^{3+}:\text{YVO}_4$  lasers.



## Chapter 3

---

### Nd<sup>3+</sup>:YVO<sub>4</sub> characteristics

*The very slow upper level decay rate and the large absorption cross-section of neodymium vanadate (Nd<sup>3+</sup>:YVO<sub>4</sub>) make it ideal for the study of small class B lasers. Here, the characteristics of the Nd<sup>3+</sup>:YVO<sub>4</sub> crystal will be investigated; we focus on the atomic levels, the decay rates and the effect of temperature on the birefringence and gain. The crystal temperature is measured by observing its effect on the crystal's birefringence.*

#### 3.1 Spectroscopic properties

Neodymium, a rare earth metal, is used as dopant in a variety of host materials, among which amorphous glass, crystalline yttrium aluminium garnet (YAG) and yttrium orthovanadate (YVO<sub>4</sub>) are the most common. In all these materials, the neodymium is triply ionised with three electrons bonding to neighbouring host atoms. As a dopant in YVO<sub>4</sub> and YAG, the Nd<sup>3+</sup> ion substitutes a Y<sup>3+</sup> atom, and the Nd<sup>3+</sup> ions are hence hosted in a nearly identical environment, ensuring homogeneously broadened transitions at room temperature. Upon cooling, however, the inhomogeneous spectrum becomes apparent as the homogeneous spectrum narrows (the emission line at 1064 nm narrows to typically 30 GHz full-width-half-max as compared to the homogeneous width of 215 GHz at room temperature). There is more than one laser transition and the crystal is operated at 914 nm and 1342 nm as well as at the more common 1064 nm transition.

In all our experiments, we use the 1064 nm transition which corresponds to a four-level configuration. Here the <sup>4</sup>I<sub>9/2</sub> state is the ground state and, as shown in Fig. 3.1, the atoms are excited from this state to two closely spaced high energy states (<sup>4</sup>H<sub>9/2</sub> and <sup>4</sup>F<sub>5/2</sub>) using a pump of 809 nm [8]. Once excited, the atoms relax to the lower <sup>4</sup>F<sub>3/2</sub> state. This is the upper laser level. The <sup>4</sup>F<sub>3/2</sub> state decays primarily to either the lowest of the <sup>4</sup>I<sub>11/2</sub> states [7] or to the <sup>4</sup>I<sub>9/2</sub> level with branching ratios 0.467 for the <sup>4</sup>F<sub>3/2</sub>→<sup>4</sup>I<sub>11/2</sub> transition and 0.420 for the <sup>4</sup>F<sub>3/2</sub>→<sup>4</sup>I<sub>9/2</sub> transition. Lasing around 1064 nm is readily achieved as the <sup>4</sup>I<sub>11/2</sub> level decays relatively quickly to the ground state (the rate is estimated to be  $\gamma_2 = 1 - 2 \times 10^9 \text{ s}^{-1}$  [9, 10]) whereas the decay time of upper lasing level is as long as 77  $\mu\text{s}$  (see section 3.3).

The extremely long lifetime of the upper level implies that essentially all Nd<sup>3+</sup>:YVO<sub>4</sub> lasers are class B lasers. Also, it makes Nd<sup>3+</sup> and other Nd<sup>3+</sup> lasers particularly suited for frequency doubling. In this process, Q-switching is often used to enhance the efficiency for frequency doubling. It is the relatively slow dynamics of Nd<sup>3+</sup>:YVO<sub>4</sub> lasers that allow for this.

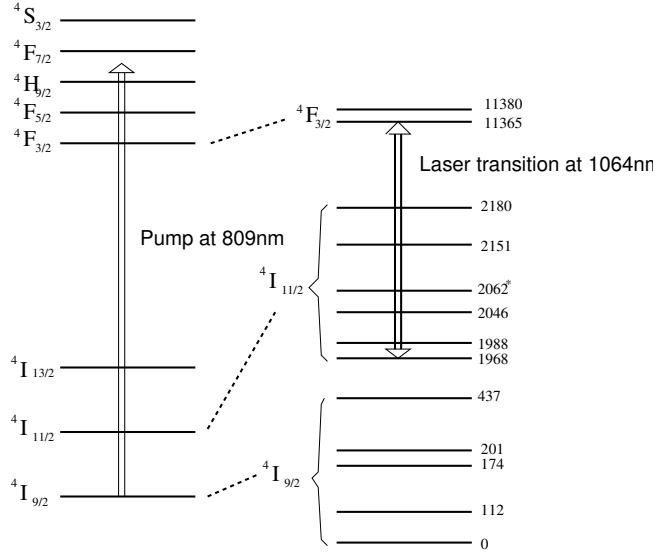


**Figure 3.1:** Energy level diagram of  $\text{Nd}^{3+}:\text{YVO}_4$  at room temperature. As the diagram indicates, the crystal is pumped at 809 nm and the most common lasing transition is the 1064 nm  ${}^4\text{F}_{3/2} \rightarrow {}^4\text{I}_{11/2}$  transition. The numbers refer to the energy of the level and is denoted in  $\text{cm}^{-1}$ . In addition to the laser transition at 1064 nm, the  ${}^4\text{F}_{3/2}$  decays to the  ${}^4\text{I}_{9/2}$  level, emitting light at  $\approx 890$  nm. This figure was compiled from Refs. [6, 7]. All the measurements were conducted at 300 K except for the measurement marked with an asterisk; this was measured at 85 K [7].

## 3.2 Parameter nomenclature

Lasers physics is at the crossroads of many disciplines such as quantum mechanics, atomic physics, material science and solid state physics, and as a result of this diversity, nomenclature tends to differ from publication to publication. As well as depending on the discipline, parameter names also depend on considerations such as convenience (and logic) when applied in a specific model. Hence, this thesis' decay rate of the upper lasing level,  $\gamma_1$ , can be denoted as  $\gamma_a$  [5, 11],  $\gamma_{\parallel}$  [12, 13] or  $\gamma_2$  [1]. Similarly, we denote the lower level decay rate as  $\gamma_2$ , while other authors use  $\gamma_b$  [5, 11] and  $\gamma_1$  [1]. The cavity decay rate  $\Gamma_c$  is sometimes also denoted as  $\gamma_c$  [1], or (rather inconveniently)  $K$  [12].

## 3.3 Measurement of inversion decay

The intriguing noise behaviour that is the central point of this thesis is caused by the slow upper level decay rate of the  $\text{Nd}^{3+}:\text{YVO}_4$  crystal. This decay rate is directly dependent on the properties of the  $\text{Nd}^{3+}$  ion and is only mildly affected by the  $\text{YVO}_4$  host. The decay rate can be found by measuring the fluorescence decay when exposing the crystal to a pulsed or a chopped pump. Fig. 3.3 shows such a measurement using a 0.23(3) mm thick CASIX crystal being pumped with a chopped 1 mW Ti:Sapph laser. The pump laser had a Gaussian beam profile and was focussed onto the crystal where the beam had a width of 14  $\mu\text{m}$  (FWHM) .

Since the amount of fluorescence is proportional to the population of the upper lasing level, this graph also allows one to determine the inversion decay rate. Measuring a small batch

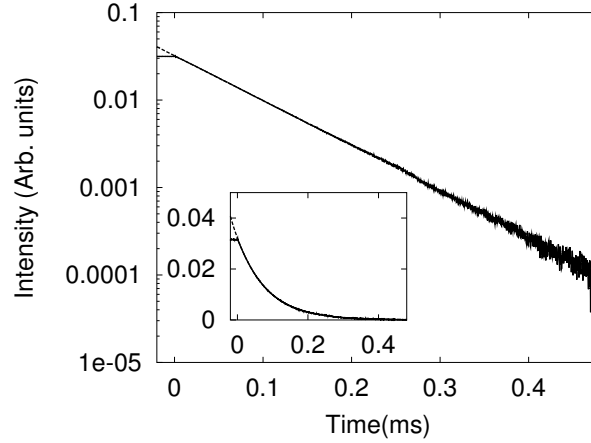


**Figure 3.2:** Fluorescence decay in a Nd<sup>3+</sup>:YVO<sub>4</sub> crystal. The pump laser (with a power of 1 mW) is switched off at the point  $t = 0$  s. The inset shows the same decay on a linear scale. The fit (broken curve) in the figure corresponds to a population decay rate of  $1.18 \times 10^4 \text{ s}^{-1}$ .

of crystals from different manufacturers and with different levels of neodymium doping we found that the results were consistent with  $\gamma_1 = 1.18(3) \times 10^4 \text{ s}^{-1}$  for a doping of 1%. However, the doping level affected the decay rate which was found to be  $3.70(5) \times 10^4 \text{ s}^{-1}$  for crystals with 3 % doping (these crystals were not, however, used in the experiments). The increased population decay rate at higher doping levels is due to non-radiative decay in Nd<sup>3+</sup>:YVO<sub>4</sub> crystals with impurities. The non-radiative decay is often preceeded by diffusion of the excitation from one neodymium ion to another and then to an impurity, leading to ion-pair relaxation [7]. This process is greatly enhanced at a larger concentration of neodymium ions. Another effect worth mentioning is that the pump intensity was observed to affect the decay rate. The value of  $\gamma_1 = 1.18(3) \times 10^4 \text{ s}^{-1}$  reported above was obtained using a pump of 1 mW. For a 120 mW pump a higher decay rate of  $1.40(5) \times 10^4 \text{ s}^{-1}$  was found. The observed increase is most probably due to crystal heating as this leads to enhanced relaxation through phonon-assisted radiative transitions [14] and pure multiphonon transitions [15, 16]. The pump strength applied in our experiments would typically be somewhere between 1 mW and 120 mW; we therefore chose to use an average decay rate of  $1.3(1) \times 10^4 \text{ s}^{-1}$  for the upper laser level in the following chapters.

To gauge the magnitude of the various relaxation effects, we compare our measurements with the results of Lomheim and DeShazer [8] who measured the lifetime of the upper laser level in Nd<sup>3+</sup>:YVO<sub>4</sub> crystals with 0.412 % neodymium doping. At this level of neodymium doping, the effect of ion-pair relaxation is thought to be negligible [8]. The decay rate was found to be equal to  $0.91 \times 10^4 \text{ s}^{-1}$  in these crystals with low doping. Judd-Ofelt theory [17, 18] gives an indication of what the relaxation rate would be with neither multiphonon nor ion-pair relaxation effects. The theory was applied [8] to calculate a decay rate of  $0.66 \times 10^4 \text{ s}^{-1}$  for the neodymium doping ion. When compared to our own measurements ( $\gamma_1 = 1.18(3) \times 10^4 \text{ s}^{-1}$ ), the results suggest that both ion-pair and phonon-related relaxation influence the

upper level decay rate of the crystal significantly at a 1 % doping level.

### 3.4 Pumping of $\text{Nd}^{3+}:\text{YVO}_4$ crystals

Unlike semiconductor lasers,  $\text{Nd}^{3+}$  type solid state lasers need to be pumped optically since the host crystal is an insulator. While using a flashlamp is possible, it is more convenient to use another laser because of the comparatively well-defined properties and the high intensities of such a laser pump. In commercial applications,  $\text{Nd}^{3+}:\text{YVO}_4$  crystals are usually pumped by semiconductor diode lasers. These diode lasers have the advantage that they are pumped electrically; two disadvantages of these lasers, however, are their poor spatial properties and comparatively wide emission spectrum. This is especially true in the case of a diode array, where the emission spectrum comprises many relatively broad resonance peaks, with each peak being produced by a separate diode.

Single laser diodes are often the most convenient way to pump  $\text{Nd}^{3+}:\text{YVO}_4$  crystals and they are in common use for both research and commercial purposes. They are of small size and they are easy to operate. However, these devices do not scale well and they deliver relatively little output power (maximum output power seldomly reaches more than 200 mW). As a result they are mostly found in compact devices with low intensity requirements.

Because of the intensity restrictions of the single diodes, we have used both a diode array and a titanium sapphire laser to pump our  $\text{Nd}^{3+}:\text{YVO}_4$  crystal. These two lasers are presented below. In sections 3.5 and 3.6 some peculiarities of the high power diode array will be discussed.

High pump powers can be reached by stacking many laser diodes to make a diode array. An example of such an array suitable for pumping  $\text{Nd}^{3+}:\text{YVO}_4$  crystals is the TSA30-0808-0600 fiber-outcoupled diode pump from *Spectra Physics*. This pump has an specified output power of 30 W that is delivered through a fiber (OPCFS 637 1M LOH) with a core diameter of 600  $\mu\text{m}$ . As commonly seen in fiber-outcoupled laser diodes, the outcoupled light has an inconvenient top-hat beam profile and a beam cone with strong divergence (in this case 25 degrees full angle). The emission spectrum is also typically wide, even compared to the absorption linewidth of the gain medium, effectively wasting some of the pump light. Fig. 3.3 compares the emission spectra of our diode array with the absorption of  $\text{Nd}^{3+}:\text{YVO}_4$ . In addition to the relatively width of the diode array spectrum (curve a), the reader should note that the absorption is surprisingly weak when compared to measurements using a low-intensity beam (curve c), even within the absorption profile (which has a width of approximately 600 GHz). This is partially a result of the mixed polarisation of the pump beam: approximately 5 % of the light is polarised along the ordinary axis which has a relatively small absorption cross-section as compared to the extraordinary axis. The low absorption also indicates other problems such as heating, which broadens the absorption profile and lowers the peak absorption. We will return to this issue later in section 3.5.

In contrast to diode type lasers, optically pumped lasers such as Coherent's 899-01 Titanium Sapphire ring laser have intracavity etalons that limits the bandwidth of the emitted light to below 10 MHz. At 809 nm this is equivalent to a width of  $2.2 \times 10^{-5}$  nm, and is thus negligible as compared to the emission spectrum of diode lasers as well as the absorption linewidth of  $\text{Nd}^{3+}:\text{YVO}_4$  crystals. The narrow emission spectrum makes Titanium:Sapphire lasers very efficient pumps as they can be tuned to the absorption maximum of the pumped medium. This is especially important in frequency doubling applications where a narrow

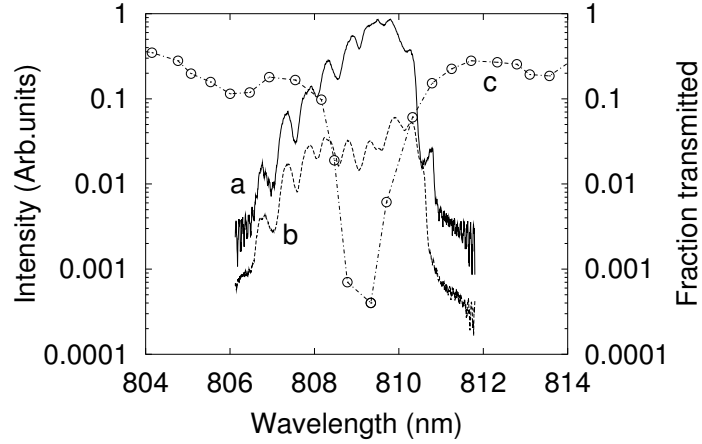


**Figure 3.3:** The output spectrum of our fiber-outcoupled diode array (Model TSA30-0808-0600 from Spectra Physics) at an output setting of 21.2 W in relation to the absorption spectrum of a 1 mm thick CASIX Nd<sup>3+</sup>:YVO<sub>4</sub> crystal. The full curve (a) shows the spectrum of the incoming light, while curve (b) shows the spectrum of light transmitted through 1 mm of crystal. The third curve (c) shows the absorption spectrum of the crystal as measured with a tunable Titanium:Sapphire laser (right hand scale shows transmitted fraction). Curve (c) was measured by J. Dingjan. The separate points represent steps of 225 GHz.

pump spectrum is a necessity. The *Coherent* 899-01 Titanium:Sapphire ring laser, does however have the disadvantage that it has to be pumped by another laser. In our case the Titanium Sapphire laser was pumped at 532 nm by either a 5 W Verdi or a 5 W Millennia. The Titanium Sapphire then produces a collimated Gaussian output beam with intensity noise as low as 0.1 % when used in combination with a “noise eater”.

### 3.5 Birefringence and temperature

One well-known property of the YVO<sub>4</sub> host crystal is its uniaxial geometry which leads to birefringence. This property ensures that lasers using *c-cut* Nd<sup>3+</sup>:YVO<sub>4</sub> crystals have a linear output polarisation that does not change with time<sup>1</sup>. Since both input and output beams are linearly polarised along the c-axis, the birefringence does not affect the beam. Even though birefringence plays no role in normal laser action, the effect can nevertheless be utilised for measurement purposes. If for instance a beam is transmitted through the crystal with field components along both polarisation axes, the difference in phase shift along the two axes will generally change the beam’s ellipticity. As we will show below, such a phase shift is also influenced by temperature changes. This makes a good tool for the measurement of heating in the crystal in a non-contact, very local way.

It is relatively straightforward to find the relationship between the relative phase shift  $\phi$  between the a- and c-components and ellipticity  $\chi$  of the transmitted beam. An incoming

<sup>1</sup>To be more precise, this is not a direct result of the birefringence itself but of the related increase in absorption and stimulated emission for light polarised along the c-axis (this is known as dichroism).

beam which is linearly polarised at  $45^\circ$  to the ordinary (a) and extraordinary (c) axes has the electric field  $\vec{E} = \vec{e}_{45} E_0 = \frac{1}{\sqrt{2}} (\vec{e}_a + \vec{e}_c) E_0$ , where  $\vec{e}_a$  and  $\vec{e}_c$  are unit vectors along the ordinary and extraordinary axes, respectively, and  $\vec{e}_{\pm 45}$ , are the two unit vectors oriented at  $45^\circ$  and  $-45^\circ$  to the ordinary axis. Then for the output light

$$\begin{aligned}\vec{E} &= E_0 (\vec{e}_a + e^{i\phi} \vec{e}_c) / \sqrt{2} \equiv E_0 (e^{-i\phi/2} \vec{e}_a + e^{i\phi/2} \vec{e}_c) e^{i\phi/2} / \sqrt{2} \\ &= E_0 [\cos(\phi/2) (\vec{e}_a + \vec{e}_c) - i \sin(\phi/2) (\vec{e}_a - \vec{e}_c)] e^{i\phi/2} / \sqrt{2} \\ &= E_0 [\cos(\phi/2) \vec{e}_{45} - i \sin(\phi/2) \vec{e}_{-45}] e^{i\phi/2}.\end{aligned}\quad (3.1)$$

From this we see that the polarisation direction is unaffected by the phase change while the ellipticity is given by  $\chi = \phi/2$ .

In the experiment, a commercial diode-pumped neodymium laser (*CrystaLaser* model IRCL-1064-100-S) was used to produce the 1064 nm incident beam polarised at  $45^\circ$  with respect to both the ordinary and extraordinary axes of our  $\text{Nd}^{3+}:\text{YVO}_4$  crystal. A 1 mm thick  $\text{Nd}^{3+}:\text{YVO}_4$  crystal with 1064 nm anti-reflective coatings on both facets was mounted inside a compartment that could be heated or cooled. The polarisation of the light behind the crystal was analysed with a combination of a rotatable quarter-waveplate followed by a half-waveplate in front of a polariser. The transmitted light was detected with a silicon photodiode (*Centronic* OSD15-0) in combination with an adjustable current converter. By minimising the transmitted light using the rotatable waveplates, it was found that the polarisation remained the same while the ellipticity changed linearly with temperature. Fig. 3.4 shows the measured ellipticity of a transmitted beam as a function of temperature.

A temperature change is expected to affect the refractive indices and  $n_a$  and  $n_c$  as well as the thickness of the crystal  $L$ . The relative phase shift  $\phi$  is thus given by

$$\frac{d\phi}{dT} = 2 \frac{d\chi}{dT} = \frac{2\pi}{\lambda} \left[ L \left( \frac{dn_a}{dT} - \frac{dn_c}{dT} \right) + (n_a - n_c) \frac{dL}{dT} \right] \quad (3.2)$$

The manufacturer (CASIX) specifies that the refractive indices are  $n_a = 1.97$  and  $n_c = 2.19$  for our probe beam at 1064 nm. The thermo-optical coefficients are specified to be  $dn_a/dT = 8.5 \cdot 10^{-6} \text{ K}^{-1}$  and  $dn_c/dT = 3.0 \cdot 10^{-6} \text{ K}^{-1}$ , while  $(1/L_a)(dL_a/dT) = 4.43 \cdot 10^{-6} \text{ K}^{-1}$ . Using these specifications we expect that  $d\phi/dT = 1.55^\circ/\text{K}$  for a 1 mm thick crystal. Our own measurements gave a comparable although slightly higher value with  $d\phi/dT = 1.70^\circ/\text{K}$  (see Fig. 3.4).

The phase change can now be used to measure the actual temperature inside the crystal when the laser is being pumped with the diode array. Using the same probe beam and the same crystal (which has no AR-coating for light at 1064 nm), we find that the crystal centre experiences a temperature increase of 64 K/W (see Fig. 3.5) when pumped with the diode array. The output power of the pump was controlled by adjusting the diode current. The 600  $\mu\text{m}$  wide fiber output was focussed onto the crystal using two composite lenses with focal length 29.5 mm. The lens next to the laser output was placed with its focus on the fiber tip, thereby ensuring that the image on the crystal was about the same size as that of the fiber output. Between the two lenses we placed a beamsplitter and a wedge in order to deposit excessive pump light in an absorber. If no wedges or beamsplitters were to be used, pump intensity would reach  $2.7 \times 10^7 \text{ W/m}^2$  at the maximum diode array output of 30 W.

The crystal birefringence is thus a very convenient diagnostics tool to measure the temperature inside the crystal. In the following section we will report shortly on how heating affects the gain.



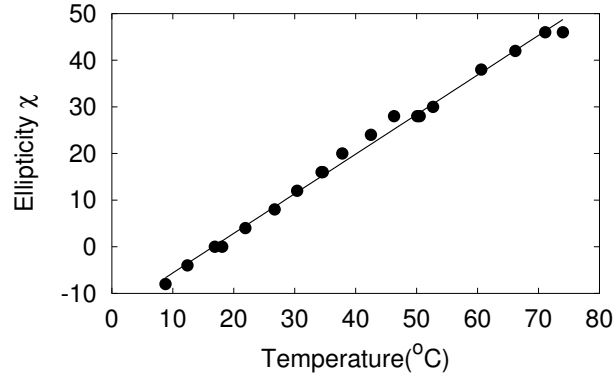


**Figure 3.4:** Ellipticity change as a function of temperature. The reference  $\chi = 0^\circ$  value is zero at room temperature (16 °C).

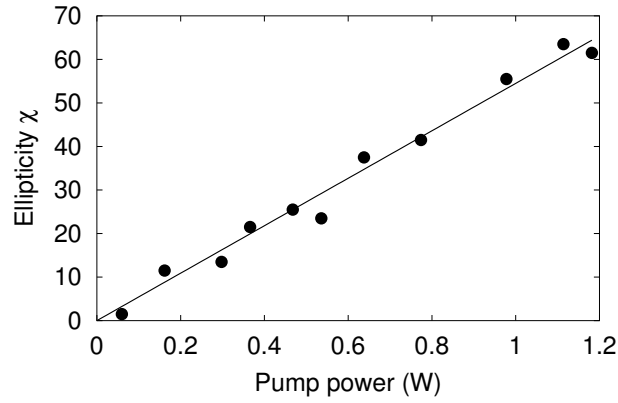


**Figure 3.5:** Ellipticity change of the transmitted beam as a function of the pump power delivered. The change in  $\chi$  has a reference value of zero for no pumping.

### 3.6 The effect of temperature on gain

One of the main limitations of Nd<sup>3+</sup>:YVO<sub>4</sub> crystals is probably their tendency to overheat. Keeping in mind the large absorption cross-section of the neodymium ions in the crystal, this is not surprising, especially when considering the modest thermal conduction coefficient of the host lattice ( $K \approx 5.1 - 5.2 \text{ Wm}^{-1}\text{K}^{-1}$  in YVO<sub>4</sub> as compared to  $38 \text{ Wm}^{-1}\text{K}^{-1}$  for LiNbO<sub>3</sub>). Heat generation is caused by the absorption of low-energy photons or phonons that originate from transitions other than the direct optical transitions of pump and output light<sup>2</sup>. Overheating can lead to damage in the crystal surface or to significantly reduced gain.

We expect this gain depreciation to be due to thermal broadening of both the absorption

<sup>2</sup>While most low-energy emissions are actually phonons (at least when their energy is less than  $2500 \text{ cm}^{-1}$  [15]), it does occur that low-energy photons are emitted. This is the case when the lower laser level of Nd : YAG crystals decays. Here photons are emitted only to be absorbed by the host lattice [6] and converted to heat.

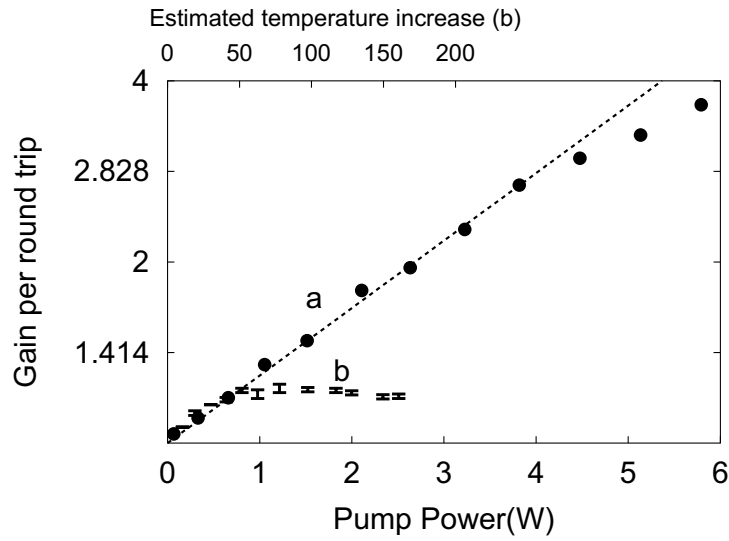


**Figure 3.6:** Gain as a function of pump power. The filled circles (a) shows the gain when using a chopped pump with the crystal fixed to a heat sink; the crosses (b) were measured with a continuous pump without any thermal management. The curve in (a) has been added to guide the eye. Note that the y-axis is plotted as a logarithmic scale. The top x-axis denotes the estimated heating in curve (b).

and emission spectra, as this broadening also reduces the peak absorption and emission coefficients. As it is the pump itself that heats the medium, Fig. 3.6 depicts the gain as a function of pump power. For this experiment we used our most powerful pump, the diode array, to compare two different configurations. The points (b) were measured having fixed the crystal with (our standard) non-conducting resin to the crystal holder while the medium was pumped continuously. The points (a) were measured using a “chopped” pump, illuminating the crystal only 1/20 of a cycle. The chopping frequency was about 10 Hz, long enough to allow inversion and photon number to reach “steady state” (for which 5 ms was available), but still fast enough to limit heat generation during the illumination period. Instead of fixing the crystal to its metal holder using non-conducting resin as in (b), indium was used (see (a)). Also the size of the holder was much larger, giving it a double function of a thermal heatsink. As Fig. 3.6 shows, the temperature has a massive impact on the attainable gain per round trip.

### 3.7 Overview Nd<sup>3+</sup>:YVO<sub>4</sub> characteristics

This section provides the reader with some general properties of the Nd<sup>3+</sup>:YVO<sub>4</sub> crystal.

Atomic density with a 1.1 % Neodymium concentration <sup>a</sup>	$1.37 \times 10^{20}$ atoms/cm <sup>3</sup>
Thermal expansion coefficient <sup>ab</sup>	Ordinary axis: $\frac{1}{L} \frac{dL_o}{dT} = 4.43 \times 10^{-6} \text{ K}^{-1}$ Extraordinary axis: $\frac{1}{L} \frac{dL_e}{dT} = 11.37 \times 10^{-6} \text{ K}^{-1}$
Thermal conductivity coefficient <sup>a</sup>	$5.2 \pm 0.1 \text{ Wm}^{-1}\text{K}^{-1}$
Refractive index <sup>ab</sup>	$n_o = 1.957, n_e = 2.1652$ @ 1064 nm $n_o = 1.972, n_e = 2.186$ @ 809 nm.
Thermal optical coefficient <sup>ab</sup>	$\frac{dn_o}{dT} = 8.5 \times 10^{-6} \text{ K}^{-1},$ $\frac{dn_e}{dT} = 3.0 \times 10^{-6} \text{ K}^{-1}$
Absorption length <sup>a</sup>	0.32 mm @ 809 nm
Gain bandwidth <sup>ac</sup>	Casix specifications: 257 GHz @ 1064 nm (equivalent to 0.96 nm ) Measured: 215 GHz @ 1064 nm
Absorption bandwidth: (see Fig. 3.3)	700(100) GHz
Decay rate upper lasing level (see sec. 3.3)	$1.3(1) \times 10^4 \text{ s}^{-1}$
Decay rate lower lasing level (see chapter 6)	$1 - 2 \times 10^9 \text{ s}^{-1}$

<sup>a</sup>These specifications can be found in the '99 crystal guide of the manufacturer, *Fujian JDSU CASIX, Inc.* [19].

<sup>b</sup>These numbers were used in section 3.5. Good agreement with the experimental results was obtained.

<sup>c</sup>In addition to the Casix specification, the gain bandwidth was measured by J. Dingjan.



## Chapter 4

### The thresholdless laser<sup>1</sup>

*Lasers with slow inversion show weak damping of quantum noise; this leads to strong relaxation oscillations and super-Poissonian statistics until far above threshold. Thus, even though the thresholds of these lasers are well-defined in terms of average output power, diffuse fluctuation thresholds are observed, and in this respect, the laser is thresholdless. Here, we outline the generic properties of thresholdless lasers and we show the importance of the condition  $\beta\Gamma_c/\gamma_1 \gtrsim 1$  for thresholdless fluctuations.*

#### 4.1 Introduction

In chapter 2 we discussed the laser properties in terms of the laser classes [3, 4]. It was shown that if the inversion decay is too slow to be adiabatically eliminated, then standard class A theory becomes insufficient to describe the laser intensity dynamics. Instead of this theory [11, 20, 21], we therefore employ the more complex class B theory [22, 23] to show that lasers with slow inversion decay (which are also known as slow-inversion lasers) have very different threshold characteristics from textbook class A lasers. This is the focus of the present chapter. We start by outlining the defining properties of laser thresholds.

The threshold of *macroscopic* class A lasers is marked by a sudden increase of output power and an abrupt quenching of the laser's quantum noise as the laser switches from chaotic lamp-like emission to coherent laser-like output [20]. The switch takes place within a very well-defined threshold region with a relative width of  $\beta^{1/2}$  [20], where  $\beta$  is the fraction of spontaneous emission going into the lasing mode [24, 2].

*Microscopic* class A lasers, i.e. lasers with only a few intracavity modes ( $\beta$  approaches 1) show very different behaviour from macroscopic lasers of the same class. For these micro-lasers the threshold is poorly defined both in terms of the intensity and the fluctuations. This is not surprising considering that the relative threshold width  $\beta^{1/2}$  becomes of order unity for  $\beta \approx 1$  and such lasers are hence commonly referred to as thresholdless lasers [24]. However, microscopic class A lasers are interesting mostly from a theoretical point of view as they are very rare in practice.

In this chapter, we will show that small class B lasers differ from both laser types outlined above. While the intensity threshold is well-defined like in macroscopic class A lasers, the fluctuation threshold becomes diffuse due to strong noise-driven relaxation oscillations. In fact, the behaviour of the fluctuation threshold is similar to that of the thresholdless microscopic ( $\beta \rightarrow 1$ ) class A lasers.

<sup>1</sup>N. J. van Druten, Y. Lien, C. Serrat, M. P. van Exter, and J. P. Woerdman, "Laser with thresholdless intensity fluctuations", Phys. Rev. A **62**, 3808-3816 (2000).

Our study of threshold properties of small class B lasers has been limited to the intensity dynamics. Using the rate equations, we focus on the effect of laser size as quantified by the spontaneous emission factor  $\beta$ . We have shown that the intensity threshold in class B lasers may disappear even when  $\beta \ll 1$ . Linearised theory was applied successfully to describe the intensity dynamics and to derive a condition for extreme class B behaviour.

Most results presented in this chapter were published in *Physical Review A* [5]. An exception is section 4.9, which contains unpublished experiments and a short discussion on the laser behaviour when the emission factor  $\beta$  and the cavity decay rate  $\Gamma_c$  is varied. Also the appendix (section 4.11) has been added later.

## 4.2 The threshold definition

The laser's intensity threshold is easily recognised in both class A and class B lasers. In macroscopic lasers, this threshold is observed as a clear “kink” in the input-output curve as the laser switches from spontaneous to stimulated emission. To identify the fluctuation threshold, however, a measure for the fluctuation strength has to be defined first.

The fluctuations threshold is often [20] defined in terms of the sudden drop in the reduced factorial moment  $Q_2$  when the laser starts oscillating.  $Q_2$  is defined as

$$Q_2 = g_2(0) - 1 \approx \frac{\langle n^2 \rangle}{\langle n \rangle^2} - 1 = \frac{\langle \delta n^2 \rangle}{\langle n \rangle^2}, \quad (4.1)$$

where  $g_2(0)$  is the second-order correlation function,  $n$  is the intra-cavity photon number, and  $\delta n = n - n_0$ , with  $n_0$  the steady state photon number. In the thermal regime below threshold,  $Q_2$  is equal to 1, but it drops to 0 once the system stabilises above threshold. The approximation sign in Eq. 4.1 (and later in Eq. 4.2) is related to the ordering of the creation and annihilation operators, and is irrelevant for the macroscopic ( $\langle n \rangle \gg 1$ ) lasers described here.

An alternative criterion for the fluctuation threshold is the Fano factor as suggested by Rice and Carmichael [24]. It is defined by

$$F = \frac{\langle \delta n^2 \rangle}{\langle n \rangle} \approx \langle n \rangle \times Q_2 = \langle n \rangle \times (g_2(0) - 1) \quad (4.2)$$

In a macroscopic class A laser, the Fano factor exhibits a sharp peak with a height of  $\approx 2\beta^{-1/2}$  on the fluctuation threshold. The peak has a relative width of  $\beta^{1/2}$ , which is the same width as in the case of the  $Q_2$  and the average-intensity definitions. The Fano factor is equal to one both below and above threshold. When compared to the reduced factorial moment, the Fano factor has the advantage that it scales with system size. The Fano factor is used in squeezing experiments, where it allows ready comparison with coherent light, which has a Fano factor equal to 1. For super-Poissonian light the factor is greater than one, and for sub-Poissonian light, it is smaller than one.

Both the reduced factorial moment and the Fano factor are used as (fluctuation-) threshold criteria in this chapter.

### 4.3 Thresholdless oscillation

The manner in which quantum noise gives rise to relaxation oscillations was discussed briefly in section 2.3. In the present section, we will elaborate further on the ideas presented there. The analysis is based on the treatments of McCumber [23] and Lax [22] but it has been expanded to include the consequences of class B behaviour on the fluctuation threshold.

We start with the intensity rate equations. These have been derived from the laser Maxwell-Bloch equations [23, 25],

$$\dot{n} = -\Gamma_c n + \beta\gamma_1 N n + R_{sp} + f_n(t), \quad (4.3a)$$

$$\dot{N} = P - \gamma_1 N - \beta\gamma_1 N n + f_N(t), \quad (4.3b)$$

where  $P$  is the pump rate and  $R_{sp} = N\beta\gamma_1$  is the spontaneous emission rate.  $N = N_1 - N_2$  is the inversion number, with  $N_1$  and  $N_2$  representing the upper and lower level populations, respectively.  $\Gamma_c$  is the cavity decay rate and  $\gamma_1$  the upper level decay rate. The dynamics of the atomic polarisation are of no concern to us as they can be adiabatically eliminated (the polarisation decay rate,  $\gamma_\perp = 690(60) \times 10^9 \text{ s}^{-1}$  is much greater than the cavity decay rate,  $\Gamma_c$ , which is typically  $\approx 10^9 - 10^{10} \text{ s}^{-1}$ ). The makeup of Eqs. 4.3 can be explained as follows: The first two terms of Eq. 4.3a represent the cavity decay rate and stimulated emission respectively. The second term of Eq. 4.3b denotes the spontaneous emission into all modes, while the third term is stimulated emission. The two noise terms  $f_n(t)$  and  $f_N(t)$  are discussed in section 4.6.

Note that the rate equations given in Eqs. 4.3 correspond to those of an ideal four-level laser. In such a laser, the lower level depopulates quickly and the lower-level population can thus be neglected. For the laser dynamics, this approximation is valid only when the lower-level decay rate,  $\gamma_2$ , is much greater than the cavity decay rate,  $\Gamma_c$ . The non-ideal case will be considered in section 4.5.

If one assumes that there is no noise present in the system, the system will reach a steady state. This state is given by

$$N_0 = \frac{\Gamma_c}{\beta\gamma_1} \frac{n_0}{n_0 + 1}, \quad (4.4a)$$

$$\frac{M}{1 + \beta n_0} = \frac{n_0}{n_0 + 1}, \quad (4.4b)$$

where  $n_0$  and  $N_0$  are the steady state intracavity photon and the inversion numbers, respectively, and  $M = P\beta/\Gamma_c$  is known as the pump parameter. Note that Eq. 4.4b is equivalent to Eq. 2.1.

To obtain the fluctuations in the frequency domain, we linearise around steady state and write  $n = n_0 + \delta n$  and  $N = N_0 + \delta N$ , where  $\delta n$  and  $\delta N$  are the deviations from this state. This yields new, linearised rate equations:

$$\dot{\delta n} = -\gamma_n \delta n + \gamma_1 \beta (n_0 + 1) \delta N + f_n(t), \quad (4.5a)$$

$$\dot{\delta N} = -\gamma_1 N_0 \beta \delta n - \gamma_N \delta N + f_N(t), \quad (4.5b)$$

which are equivalent to Eq. 2.3 of chapter 2 except for the inversion noise term. After linearisation, we perform a Fourier transform on the rate equations. An expression for the

photon-number fluctuations as a function of frequency,  $\delta n(\omega)$ , is obtained the easiest by subsequently applying Cramer's rule,

$$\delta n(\omega) = \frac{(-i\omega + \gamma_n)f_n(\omega) - \beta\gamma_1(n_0 + 1)f_N(\omega)}{(-i\omega + \gamma_N)(-i\omega + \gamma_n) - \omega_{ro}^2}, \quad (4.6)$$

where  $\omega_{ro}$  is the relaxation oscillation frequency, which is given by

$$\omega_{ro}^2 = \gamma_1^2 N_0 \beta^2 (n_0 + 1) = \gamma_1 \Gamma_c \beta n_0. \quad (4.7)$$

In Eq. 4.6, the two damping rates,  $\gamma_n$  and  $\gamma_N$ , are especially significant .

$$\gamma_n = \Gamma_c / (n_0 + 1) \quad (4.8)$$

works directly on the photon number  $n$  and is known as the “photonic damping”. Since it is inversely proportional to  $(n_0 + 1)$ , this term decreases rapidly once the intensity threshold is crossed. Still, the very large value of  $\Gamma_c$  ensures that  $\gamma_n$  remains important until far above threshold. The “inversion damping”

$$\gamma_N = \gamma_1 (1 + \beta n_0), \quad (4.9)$$

however, increases with the intracavity photon number. This damping is weak in class B lasers, where  $\gamma_1$  is small.

Although it is relatively straightforward to show how the damping mechanisms arise from the rate equations, their physical origins are more subtle. The photonic damping  $\gamma_n$  is due to the difference between the stimulated emission rate into the lasing mode and the cavity loss rate from this mode, i.e.,  $\gamma_n = -\Gamma_c + \beta\gamma_1 N = \Gamma_c / (n_0 + 1)$ . This difference creates an effective photon loss which is made up by spontaneous emission. The inversion damping,  $\gamma_N = \gamma_1 (1 + \beta n_0)$ , is due to two effects: one is related to stimulated emission into the lasing mode (the  $\beta\gamma_1 n_0$  term), the second is due to spontaneous emission into all other modes ( $\beta\gamma_1$  term). The naming convention, i.e., photonic and inversion damping, is related to how these damping effects enter the rate equations (Eqs. 4.5).

It is important to realise that Eq. 4.6 gives resonant behaviour for  $\omega \approx \omega_{ro}$  since the relationship  $\omega_{ro} \gg \gamma_n, \gamma_N$  applies to all class B lasers operated not too close to the lasing threshold. Spectrally wide quantum noise drives relaxation oscillations at the resonance frequency.

As discussed later in section 4.6, we can generally neglect the  $f_N$  noise term. The double-sided spectral density is then

$$\langle \delta n^2(\omega) \rangle = \frac{2(\omega^2 + \gamma_N^2)R_{sp}n_0}{(\omega_{ro}^2 + \gamma_n\gamma_N - \omega^2)^2 + 4\omega^2\gamma_{ro}^2}, \quad (4.10)$$

where we have  $\gamma_{ro} = (\gamma_N + \gamma_n)/2$  and where  $\langle f_n^2(\omega) \rangle = 2R_{sp}n_0$  (see page 2.3). Eq. 4.10 can now be integrated over all positive and negative frequencies [26], resulting in a reduced factorial moment  $Q_2$  that equals

$$\begin{aligned} Q_2 &= \left( \frac{\gamma_n}{\gamma_n + \gamma_N} \right) \left( 1 + \frac{\gamma_N^2}{\omega_{ro}^2 + \gamma_n\gamma_N} \right) \\ &= 1 - \left( \frac{\gamma_N}{\gamma_n + \gamma_N} \right) \left( \frac{\omega_{ro}^2}{\omega_{ro}^2 + \gamma_n\gamma_N} \right). \end{aligned} \quad (4.11)$$



This expression for fluctuations in class B lasers is the main result of this chapter. From Eq. 4.11 we see that the reduced factorial moment remains high as long as  $\gamma_N < \gamma_n$ , since the condition  $\omega_{ro}^2 > \gamma_n \gamma_N$  is fulfilled for most lasers with  $M > 1$ . The mentioned condition  $\gamma_N < \gamma_n$  shows that the fluctuations will only damp out when the atomic damping is larger than the photonic damping. Although this relation is surprising, its explanation is straightforward as both the photonic damping and the oscillation driving force are due to the same spontaneous emission. Hence, when considering the laser dynamics, the fraction  $\gamma_N/\gamma_n$  is central. It can be written as

$$\frac{\gamma_N}{\gamma_n} \approx \frac{\gamma_1(1 + \beta n_0)n_0}{\Gamma_c} \approx \frac{\gamma_1 M(M-1)}{\beta \Gamma_c}, \quad (4.12)$$

where the approximation  $n_0 \approx (1/\beta)(M-1)$  was used (see Eq. 2.1). The stabilising effect of the pump is reflected in the fact that  $\gamma_N/\gamma_n$  becomes larger with increasing  $M$ . How quickly the output is stabilised depends on the relative strength of the parameters  $\beta$ ,  $\Gamma_c$  and  $\gamma_1$ . This is discussed in the section below.

## 4.4 The slow inversion condition

It is convenient to distinguish three different categories of lasers on the basis of Eq. 4.12. The three categories are known as the macroscopic, mesoscopic and the microscopic regime and they are equivalent to those outlined by Hofmann and Hess in Ref. [27]. The boundaries of these categories depend on the factor  $\beta$ , and the ratio  $\Gamma_c/\gamma_1$ , which are two dimensionless parameters for the cavity size and the “relative slowness” of the inversion decay, respectively. Hence the names macroscopic, mesoscopic and microscopic, and the term “slow-inversion laser”.

The macroscopic regime is defined by

$$\beta \lesssim (\gamma_1/\Gamma_c)^2, \quad (4.13)$$

which is valid for large class B lasers and all class A lasers. This is the textbook example of a laser with strong inversion damping and well-defined thresholds. In this regime  $\gamma_N > \gamma_n$  as soon as  $M > 1$ . Hence, we assume that  $\gamma_N/(\gamma_n + \gamma_N) \approx 1$  in Eq. 4.11, yielding a new, simplified expression for  $Q_2$ :

$$Q_2 \approx \frac{\gamma_n \gamma_N}{\omega_{ro}^2 + \gamma_n \gamma_N}, \quad (4.14)$$

where all the  $\Gamma_c$  and  $\gamma_1$  factors cancel out when Eqs. 4.7-4.9 are inserted, leaving only  $n_0$  and  $\beta$ . It can thus be shown that the fluctuation level  $Q_2$  always drops from 1 to 0 within a narrow region of width  $\approx \beta^{-1/2}$ .

The microscopic regime is the opposite of the macroscopic regime. These lasers are true slow-inversion lasers with very distinct class B properties. The definition for this regime is

$$\beta \gtrsim \gamma_1/\Gamma_c, \quad (4.15)$$

where quantum noise is very weakly damped, resulting in very deep relaxation oscillations that persist until far above threshold. The approximation  $\omega_{ro}^2 \gg \gamma_n \gamma_N$  is used (and should be valid except very close to the intensity threshold) to yield

$$Q_2 \approx \frac{\gamma_n}{\gamma_n + \gamma_N}. \quad (4.16)$$

Since photonic damping  $\gamma_n$  remains much smaller than the inversion damping  $\gamma_N$  in this regime,  $Q_2 = 1/2$  is only reached at  $M \approx 1/2 + (\Gamma_c \beta / \gamma_1)^{1/2} \gtrsim 2$  (where the approximation holds unless the laser is operated very close to  $M = 1$ ). The Fano factor peaks at the same point. The fluctuation threshold not only shifts, it also becomes much more diffuse. This is discussed together with our experimental results in sections 4.8 and 4.9

In addition to these regimes, the mesoscopic regime is naturally defined as

$$\gamma_1 / \Gamma_c \lesssim \beta \lesssim (\gamma_1 / \Gamma_c)^2, \quad (4.17)$$

marking the intermediate case between the two opposing regimes outlined above. It has many of the same fluctuation properties as the microscopic regime, but to a lesser extent.

## 4.5 Damping due to the lower-level decay

Until now, we have assumed that the lower-level population has a negligible effect on the laser dynamics. This assumption holds true for lasers known as ideal four-level lasers. In such lasers the lower-level decay rate is very fast as compared to the photon dynamics of the system. Although the decay rate of the lower lasing level  $\gamma_2$  in  $\text{Nd}^{3+}:\text{YVO}_4$  is generally considered to be very fast ( $\gamma_2 = 1 - 2 \times 10^9 \text{ s}^{-1}$  as compared to  $\gamma_1 = 1.3(1) \times 10^4 \text{ s}^{-1}$ ), it is still slower than the cavity decay rate of our setup ( $\Gamma_c \approx 10^9 - 10^{10} \text{ s}^{-1}$ ). This leads to a significant lower-level population and strong relaxation oscillation damping. To account for this phenomenon in our theory, we consider rate equations that comprise the lower level

$$\dot{n} = -\Gamma_c n + \beta \gamma_1 (N_1 - N_2) n + R_{sp} + f_n, \quad (4.18a)$$

$$\dot{N}_1 = S - \gamma_1 N_1 - \beta \gamma_1 (N_1 - N_2) n, \quad (4.18b)$$

$$\dot{N}_2 = -\gamma_2 N_2 + \gamma_1 N_1 + \beta \gamma_1 (N_1 - N_2) n, \quad (4.18c)$$

where the spontaneous emission rate  $R_{sp} = N_1 \beta \gamma_1$ . As before in Eq. 2.2, the Langevin noise source  $f_n(t)$  satisfies  $\langle f_n(t) f_n(t') \rangle = 2R_{sp} n \delta(t - t')$ . The inversion noise source has been neglected (see section 4.6).

In order to derive an expression for relaxation oscillation damping, we assume that the dynamics of the lower level can be adiabatically eliminated ( $\dot{N}_2 = 0$ ). This assumption is fulfilled in all our experiments, since  $\gamma_2 \gg \gamma_1, \omega_{ro}$ . We can now reduce Eq. 4.18c to

$$N_2 = N_1 \frac{\gamma_1(1 + \beta n)}{\gamma_2 + \gamma_1 \beta n}, \quad (4.19)$$

which allows us to remove  $N_2$  from Eqs. 4.18a and 4.18b. Since  $\gamma_2 \gg \gamma_1$ , we find that the lower-level population is small but its dynamics are fast. The lower-level population  $N_2$  responds almost instantaneously to any change in the photon number, which gives rise to significant damping despite the small lower-level population.

We now derive the linearised rate equations for a laser with a lower-level population. For this we substitute  $n = n_0 + \delta n$  and  $N_1 = N_{1,0} + \delta N_1$ . With the assumption that  $\gamma_1 / \gamma_2 \ll 1$  and  $\beta \ll 1$ , the rate equations become:

$$\dot{\delta n} = -(\gamma_n + \gamma_{NL}) \delta n + \beta(n_0 + 1) \delta N_1 + f_n, \quad (4.20a)$$

$$\dot{\delta N}_1 = -\gamma_1 N_{1,0} \beta \delta n - \gamma_N \delta N_1, \quad (4.20b)$$

which are essentially the same as those reported in section 4.3 (Eqs. 4.5) except for an additional damping term,  $\gamma_{NL}$ , and the replacement of the inversion  $N$  by the upper level population  $N_1$ . The additional damping term is

$$\gamma_{NL} = \frac{\gamma_1 \Gamma_c \beta n_0}{\gamma_2} = \frac{\omega_{ro}^2}{\gamma_2}. \quad (4.21)$$

This damping has its origin in the non-linear (stimulated-emission) term of Eq. 4.18a and is therefore known as the non-linear damping (see also [10]).

Non-linear damping leads to weaker intensity fluctuations. The expression for  $Q_2$  is now

$$Q_2 = \frac{\langle \delta n^2 \rangle}{n_0^2} = \left( \frac{\gamma_n}{\gamma_n + \gamma_N + \gamma_{NL}} \right) \left( 1 + \frac{\gamma_N^2}{\omega_{ro}^2 + [\gamma_n + \gamma_{NL}] \gamma_N} \right), \quad (4.22)$$

which is slightly more complex than Eq. 4.11. Despite this added complexity, we can still identify three different laser regimes as before.

In the macroscopic regime, we compare  $\gamma_{NL}$  to the photonic damping  $\gamma_n$  to find that

$$\frac{\gamma_{NL}}{\gamma_n} = \frac{\gamma_1 \beta n_0 (n_0 + 1)}{\gamma_2}, \quad (4.23)$$

which is very small close to  $M = 1$  since  $\gamma_2 \ll \gamma_1$  (this is necessary to create inversion). Thus, for macroscopic lasers, non-linear damping does not affect the threshold and Eq. 4.14 for  $Q_2$  is still valid close to threshold.

In the microscopic regime, intensity fluctuations persist for relatively large values of  $M$  and here non-linear damping does often play a role. When comparing non-linear damping to inversion damping, we find that

$$\frac{\gamma_{NL}}{\gamma_N} = \frac{\Gamma_c}{\gamma_2} \left( \frac{M-1}{M} \right), \quad (4.24)$$

indicating that non-linear damping becomes significant once  $\gamma_2 \lesssim \Gamma_c$ . In all our experiments  $\gamma_2 \ll \Gamma_c$  (and generally even  $\gamma_2 \ll \Gamma_c (M-1)/M$ ) with the result that the non-linear damping completely dominates over the inversion damping. This yields

$$Q_2 \approx \frac{\gamma_n}{\gamma_n + \gamma_{NL}} \quad (4.25)$$

for the microscopic regime with dominant non-linear damping, i.e.  $\gamma_{NL} \gg \gamma_N$ .

Based on the above results, the slow inversion condition for the microscopic regime (Eq. 4.15) can be rewritten as

$$\beta \gtrsim \frac{\gamma_1}{\gamma_2}, \quad (4.26)$$

where  $\Gamma_c$  in Eq. 4.15 has been substituted by  $\gamma_2$ . The definition for the mesoscopic and macroscopic regimes may still, however, remain unchanged, i.e. the same as in Eqs. 4.13 and 4.17. There are two reasons for this. One, as compared to inversion damping, non-linear damping plays a comparably small role at small  $M$  (see discussion above). Additionally, since  $\Gamma_c = 2c/l_{opt} \ln R_m \propto 1/l_{opt}$ , we find that somewhat larger lasers generally have  $\Gamma_c \ll \gamma_2$ , and that the ideal four-level approximation is therefore often still valid.

## 4.6 Noise sources

All noise sources can be divided into two categories: photon noise and inversion noise, depending on how they enter the rate equations.

The photon noise, represented by  $f_n(t)$  in Eq. 4.6, is due to spontaneous emission noise (as discussed in chapter 2). There is also a thermal component to the photon noise, but at room temperature this is negligible in the near-infrared of laser operation (see chapter 1). As before, the photon noise strength is given by  $\langle f_n(t)f_n(t') \rangle = 2R_{sp}n\delta(t-t')$ .

The inversion noise source is represented by the Langevin term  $f_N(t)$ . A Poissonian pump source has  $\langle f_N(t)f_N(t') \rangle = 2\gamma_1 N\delta(t-t')$  [25], which is comparable in size to the photon (quantum) noise source. The largest difference in the effect of the two noise sources lies in the prefactors in Eq. 4.6. At the “resonance” oscillation frequency  $\omega_{ro}$ , the “photon” prefactor ( $\approx \omega$ ) is much larger than the “inversion” prefactor ( $\gamma_1\beta(n_0+1) \approx \gamma_1(M-1)$ ). At frequencies around  $\gamma_1$  and below, inversion noise does play a role and if a sufficiently regular pump is used, the output of the laser might even become squeezed [10]. However, the squeezing bandwidth will naturally be limited to frequencies  $\omega \lesssim \gamma_1(M-1)$ .

In addition to the Poisson intensity noise, we consider technical pump noise. This noise enters the inversion noise term  $f_N$  through the pump  $P$ . If the bandwidth of this noise is  $\gamma_{pump}$  and it has a relative root-mean-square strength  $R$ , the contribution to the spectral density of  $\langle f_N^2 \rangle$  is approximately  $R^2 P^2 / \gamma_{pump}$  (for frequencies  $\omega < \gamma_{pump}$ ).

We now estimate the impact of this pump noise at the relaxation oscillation frequency by assuming the worst case scenario, which is when the pump noise extends up to and beyond the relaxation oscillation frequency  $\omega_{ro}$ . Comparing the pump noise contribution to  $\langle \delta n^2(\omega_{ro}) \rangle$  with that of the photon noise, yields a ratio (pump noise over photon noise)  $R^2 M^2 \gamma_1 / 2\beta \gamma_{pump}$ . In our experiment, the experimental parameters are such that this is much smaller than 1 since  $R \approx 0.001$  (as we will see in section 4.7). Pump noise is hence negligible, even in the case of this simple model, where the pump’s bandwidth has been greatly overestimated.

At low frequencies, the relative contribution to the spectral density of  $\delta n$  equals approximately  $R^2 \Gamma_c n_0 / 2\gamma_{pump}$ . In our experiments, this would dominate the noise at low frequencies. As a result, low-frequency squeezing is not possible [27].

## 4.7 Experimental setup

The microchip laser was the central component of our setup. The laser cavity was constructed using a  $\text{Nd}^{3+}:\text{YVO}_4$  crystal of small lateral size and a convex mirror. The mirror could easily be replaced for one with a different coating. On one side, all the crystals were coated with a coating that was anti-reflective at 809 nm and highly reflective at the emission wavelength of 1064 nm. On the opposite side, the crystals had anti-reflective coatings at the emission wavelength of 1064 nm. The mirror, which faced the second facet, had a radius of curvature of  $R = -25$  mm and its angle to the laser beam could be adjusted to ensure cylinder symmetry of the cavity.

For flexibility, the mirror was mounted on a translation stage that allowed us to lengthen or shorten the cavity very easily (see Fig. 4.1) with an accuracy of 1  $\mu\text{m}$ . In addition, the crystal was mounted on a cylindrical piezo that was connected to a piezo driver (*Technical Optics FPZ-1-RG*). This allowed for very fine sub-wavelength adjustment of the cavity

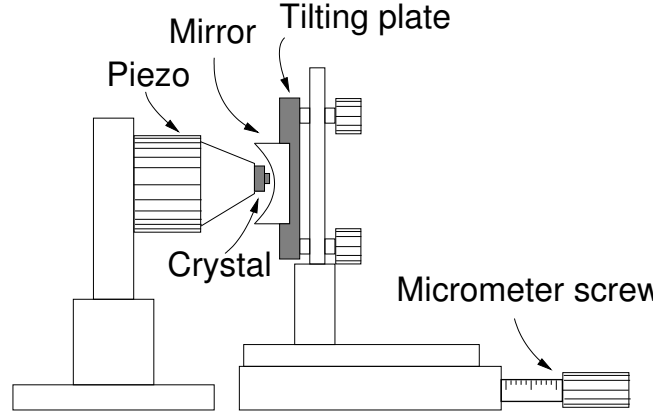


**Figure 4.1:** Crystal and mirror mounts. The mirror mount was placed on a translation stage, allowing for easy adjustment of the cavity length.

length. Hence we could tune the laser to gain maximum by observing its output.

The piezo could also be used to measure the cavity length. By detuning the laser from gain maximum, we could get it to lase in two longitudinal modes. By means of a Fabry-Perot interferometer, we measured the longitudinal mode splitting for a “typical” cavity with a 200  $\mu\text{m}$  crystal and a normal  $R = -25$  mm mirror as  $c/2l_{\text{opt}} = 250(30)$  GHz. From this an optical length  $l_{\text{opt}} \approx 600(70)$   $\mu\text{m}$  was found. This is consistent with geometrical considerations of the cavity. Note that frequency pulling can still be neglected as the cavity loss rate is still much smaller than the spectral width of the gain profile ( $\approx 225$  GHz).

In general, we always constructed a cavity that was as compact as possible to ensure a relatively large  $\beta$  factor. To shorten the distance between the mirror and the crystal for our measurements with the highest  $\beta$  value, in some experiments we used a mirror of which the mirror edges were ground away, leaving only a post in the middle as described further in chapter 6. We worked with the different crystal thicknesses 100  $\mu\text{m}$  and 200  $\mu\text{m}$ . In experiments with the 100  $\mu\text{m}$  thick crystals and the modified mirror, we reached values for  $\beta$  as high as  $10^{-5}$ . For unmodified mirrors and the 200  $\mu\text{m}$  crystal,  $\beta$  was typically of the order  $10^{-6}$  when the mirror was placed as close as possible to the crystal.

The  $\text{Nd}^{3+}:\text{YVO}_4$  crystal was pumped using a *Coherent* 899-01 Titanium:Sapphire ring laser which itself was pumped by a 5 W *Millennia*. With the use of a noise eater, the intensity fluctuations in the pump beam were brought down to below 0.1 % r.m.s.. To focus the beam onto the crystal, we used a lens with a focal length of 100 mm. The pump beam hence had a cross-section of 38  $\mu\text{m}$ , which is approximately 1.3 times larger than that of a  $\text{TEM}_{00}$  cavity mode. In our setup, this ensured negligible gain guiding and the laser was indeed clearly lasing in a single  $\text{TEM}_{00}$  mode. We employed a *Cohu* 4722 CCD-camera to monitor the intra-cavity modes and to measure mode cross-sections.

The intensity measurements were conducted using two different detectors. One detector, a *Centronic* OSD15-0 silicon detector, was used in combination with an external current converter to measure the average output intensity. The intensity dynamics were observed with another, faster DC-coupled detector with a bandwidth of 20 MHz. This detector, which is homebuilt, was equipped with a InGaAs photo diode.

The intensity time traces were recorded using a 9310L *LeCroy* oscilloscope which could record up to  $1 \times 10^6$  points at a maximum sampling rate of  $1 \times 10^8$  samples per second. The RF-spectra were recorded with a *Tektronix* 2712 spectrum analyser.

## 4.8 Experimental Results: Thresholdless oscillations

A recurring theme of this chapter, and indeed this whole thesis, is the large intensity fluctuations of lasers that fulfil the slow inversion condition, Eq. 4.15. To help the reader imagine the dynamics involved, typical intensity measurements have been plotted in Fig. 4.2. From the figures it can be seen that the oscillations change from being harmonic far above threshold ( $M = 8.5$  in Fig. 4.2a and b) to being anharmonic closer to threshold ( $M = 1.5$  in Fig. 4.2c and d). Just above threshold, at  $M = 1.065$ , a regime is reached where the oscillation damping rate  $\gamma_{ro}$  becomes as large as the oscillation rate  $\omega_{ro}$ . This leads to oscillations with an ill-defined oscillation frequency as observed in Fig. 4.2e and f. It is such time traces that are used to (directly) calculate the reduced factorial moment  $Q_2 = \langle \delta n^2 \rangle / \langle n \rangle^2$ . To make this average accurate, the total measurement time has to be large as compared to the relaxation rate of the relaxation oscillations  $\gamma_{ro} = (\gamma_n + \gamma_N + \gamma_{NL})/2$  in order to average out the slowly varying dynamics. The number of measurement points must also be sufficiently large.

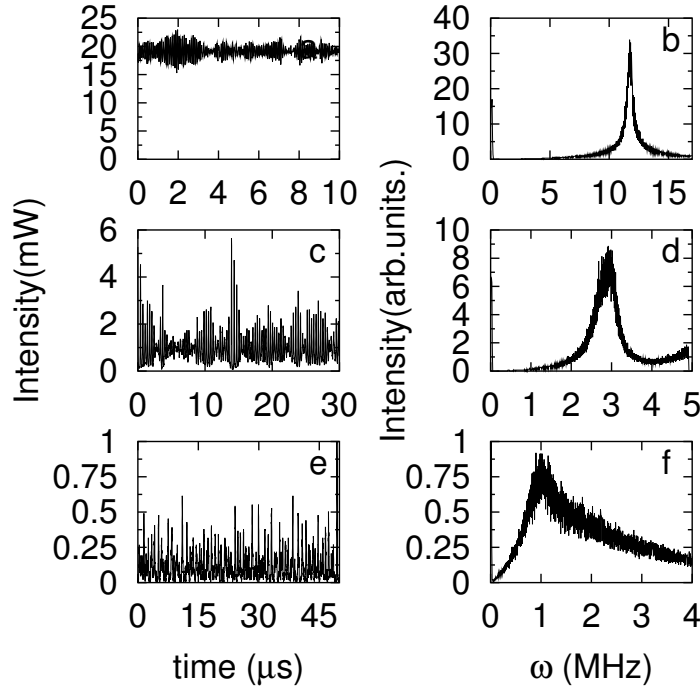


**Figure 4.2:** The effect of the pump strength on relaxation oscillations in a slow inversion laser. The three plots on the left show typical timetraces for a laser showing slow inversion. The measurement parameters are  $\Gamma_c = 5.7 \times 10^{10} \text{ s}^{-1}$  and  $\beta = 5.8 \times 10^{-6}$ ; a and b:  $M = 8.5$ ; c and d:  $M = 1.5$ ; e and f:  $M = 1.065$ .

In the theoretical analysis of the class B laser (see section 4.3), we expressed most variables in terms of the steady-state intra-cavity photon number  $n_0$ . Here, for the experimental section, it is more convenient to use the pump parameter  $M$  instead of  $n_0$ . These two are related by  $n_0 = \beta^{-1}(M - 1)$  when the laser is not too close to  $M = 1$ . Eq. 4.22 for the intensity fluctuations in a microscopic class B laser can now be reduced to

$$Q_2 \approx \frac{\frac{\Gamma_c \beta}{(M-1)}}{\left( \frac{\Gamma_c \beta}{(M-1)} + \gamma_1 M + \frac{\gamma_1 \Gamma_c (M-1)}{\gamma_2} \right)}. \quad (4.27)$$

Apart from the pump parameter  $M$ , this expression contains four constants. These are all obtained from separate measurements. The upper level decay rate  $\gamma_1$  is obtained from the fluorescence lifetime measurements discussed in chapter 3. The lower-level lifetime of  $\text{Nd}^{3+}:\text{YVO}_4$  has been measured in [10] to be 620 ns. The cavity decay rate  $\Gamma_c$  is determined directly from the relaxation oscillation rate as described in conjunction with Fig. 4.4.  $\beta$  is found from the input-output curve (see Fig. 4.3) with the relationship  $P_{\text{out}} = \Gamma_c h\nu (M - 1)/\beta$ , where  $h\nu$  is the photon energy.

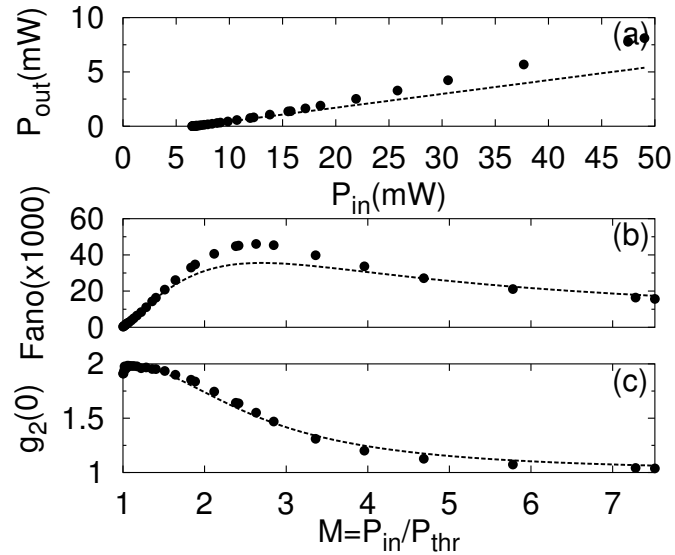


**Figure 4.3:** Results of timetrace measurements. Graph (a) shows the output intensity as a function of pump. The two lower graphs depict the resultant fluctuation measurements. (b) shows the Fano Factor. (c) shows the second order correlation function  $g_2(0)$ . The experimental parameters here are  $\beta = 2.4 \times 10^{-5}$  and  $\Gamma_c = 1.0 \times 10^{11} \text{ s}^{-1}$ . The mirror reflectivity was 80 % and the optical cavity length was estimated to be  $l_{\text{opt}} = 320(30) \text{ } \mu\text{m}^3$ .

When considering the measurements of Fig. 4.3 (which were all recorded with an oscilloscope) in terms of the two threshold definitions, we see that the intensity threshold remains well-defined with a sudden increase in output power at threshold. The fluctuation threshold, however, is diffuse and shifted. The intensity fluctuations are only weakly damped, and the Fano factor peaks at  $M \approx 2.7$  instead of  $M \approx 1$  ( $Q_2 \approx 1/2$  at the same point). Note that

Fig. 4.3 also shows the strong effect of non-linear damping, without which the fluctuation threshold ( $Q_2 = 1/2$ ) would be at  $M \approx 1/2 + (\beta\Gamma_c/\gamma_1)^{1/2} = 14.1$ . However, with non-linear damping, the fluctuation threshold is expected at  $M = 1/2 + (\beta\gamma_2/\gamma_1)^{1/2} \approx 2.2$  as derived from Eqs. 4.23 and 4.25, which is in reasonable agreement with Fig. 4.3. Deviations from theory are small; the most significant is in the intermediate  $M \approx 2.5$  region, where we measure slightly more fluctuations than suggested by theory (especially observable in the measurement of the Fano factor). This is most probably due to the anharmonic behaviour of the oscillations. Our linear model does not consider higher-order harmonics even though their contribution to the fluctuations can be large (a part of the second order harmonic is seen to the very right of Fig. 4.2d). The anharmonic effects can (at least partly) be explained using the more extensive pseudo energy theory described in chapters 5 and 6.

While the above measurements were obtained using an oscilloscope to record time traces, additional measurements were conducted with an RF-analyser. These measurements give a clear picture of the frequency behaviour of the intensity fluctuations. The oscillation rate and the damping rate of the relaxation oscillations are found directly from the spectrum by measuring the position and width of the main harmonic. Fig. 4.4 compares the measured

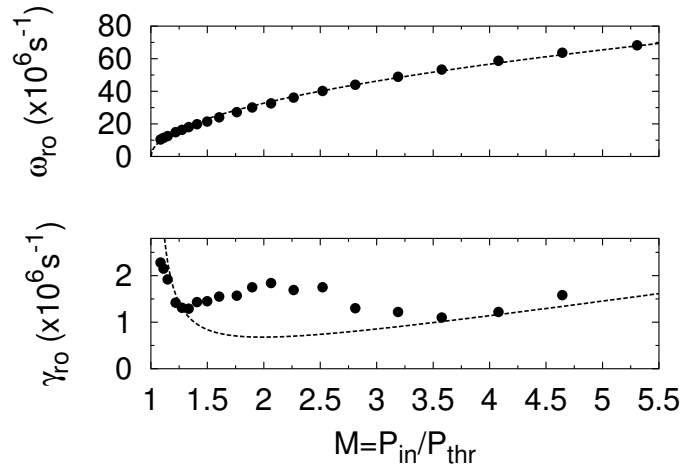


**Figure 4.4:** Relaxation oscillation rate (a) and damping rate (b) of a laser with strong relaxation oscillations. In this laser  $\beta = 8.06 \times 10^{-6}$  and  $\Gamma_c = 8.23 \times 10^{10} \text{ s}^{-1}$ .

oscillation and damping rates with the theoretical predictions. As seen from the figure, the oscillation rate is approximated quite well by theory. Since the relaxation oscillation rate is given by the simple expression  $\omega_{ro} = \sqrt{\gamma_1 \Gamma_c (M - 1)}$ , (from Eq. 4.7), we use this expression to find the value for  $\Gamma_c$ . The oscillation damping rate does not fit the theoretical prediction very well in the region  $M = 1.3$  to  $M = 3.5$ . In brief, this discrepancy is an artefact which is caused by variations in the oscillation frequency with modulation depth, which again lead to smearing of the harmonics in the intensity spectrum. This effect is the largest in the intermediate region as discussed above due to the relatively large amplitude of the oscillations in this region. Close to threshold ( $M = 1$ ) it is less pronounced because of the relatively low frequency of the oscillations. We will discuss this issue in more detail in



chapter 6.

## 4.9 Experimental results: Changing parameters

The effect of changing the two central parameters  $\beta$  and  $\Gamma_c$  will now be investigated. These parameters, whose effect was thoroughly discussed in the theoretical sections, could easily be changed by moving or replacing the cavity mirror. In conducting the experiments, we found that changing the mirror reflectivity (from 60 % to 98 %) had a negligible effect on the laser dynamics since non-linear damping dominated over inversion damping (this was expected). In comparison, changing the parameter  $\beta$  had a large effect.

We remind the reader that  $\beta$  is the fraction of spontaneous emission going into the lasing mode. This parameter is a direct function of the optical volume  $V_{cav}$  occupied by the mode. For the case where the spectral width of the spontaneous emission in free space  $\gamma_{at}$  is much larger than the cavity decay rate [2],

$$\beta = \frac{1}{p} = \frac{1}{4\pi} \times \frac{\lambda^3}{V_{cav}} \times \frac{\omega}{\gamma_{at}}, \quad (4.28)$$

where  $p$  is the number of intra-cavity modes and  $\gamma_{at}$  is the spectral width of the spontaneous emission in free space.  $V_{cav}$  changes as a function of the cavity length and width of the mode. The width,  $w_0$ , of a TEM<sub>00</sub> mode is given by  $w_0^2 = \frac{L\lambda}{\pi} \sqrt{R/L - 1}$  which reduces to  $\frac{\lambda}{\pi} \sqrt{LR}$  in short cavities. As a result,  $\beta$  is expected to scale via  $V_{cav}$  as  $\beta = L^{-3/2}$ . Since  $\beta$  represents the coupling of spontaneous emission with the lasing mode [2], it depends on the spatial overlap of the laser mode with the emission source. This spatial overlap may change as the mode widens. Eq. 4.28 assumes that *all* inverted atoms are situated in the central region of the transverse lasing profile, leading to optimal coupling. Thus, while Eq. 4.28 defines the optimum value for  $\beta$ , our values were generally somewhat lower.

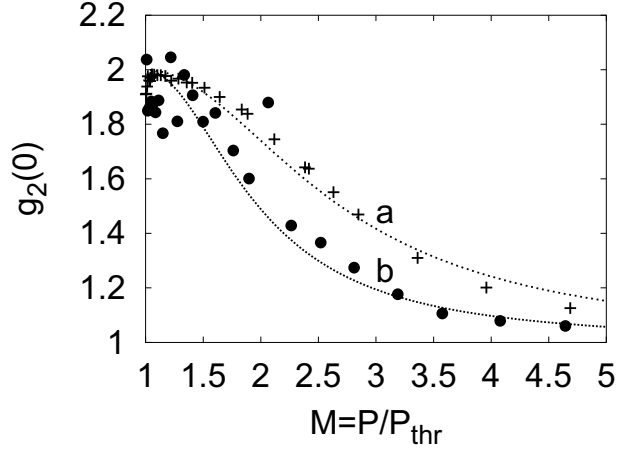


**Figure 4.5:** The effect of cavity size on fluctuation properties. For (a)  $\beta = 2.38 \times 10^{-5}$ , for (b)  $\beta = 8.06 \times 10^{-6}$ . The lines show the theoretical predictions.

In Fig. 4.5, the measured  $g_2(0)$  is plotted as a function of the pump parameter  $M$  for

different values of  $\beta$ . The value for  $\Gamma_c$  is almost the same for the two plots: for (a)  $\Gamma_c = 1.05 \times 10^{11} \text{ s}^{-1}$  and for (b)  $\Gamma_c = 0.83 \times 10^{11} \text{ s}^{-1}$ . The small difference in  $\Gamma_c$  has an almost negligible effect as is discussed below. Fig. 4.5 confirms the dependency of the threshold on  $\beta$  and hence the cavity size (see Eq. 4.28). As before, the theoretical estimates of  $g_2(0)$  lie somewhat below the experimental values since higher order harmonics have been neglected.

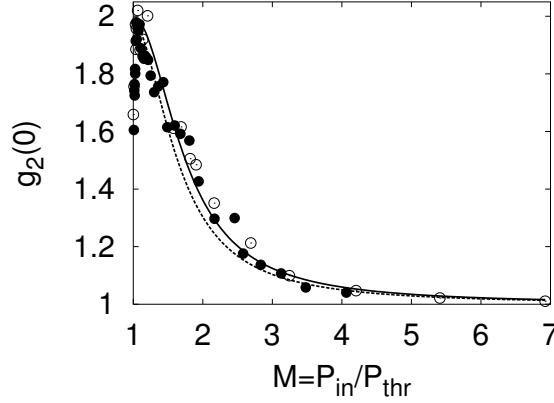


**Figure 4.6:** Changing the cavity decay rate leads only to slight changes in  $g_2(0)$ . The full curve and the filled circles were measured with  $\Gamma_c = 1.37 \times 10^{11} \text{ s}^{-1}$  (mirror reflectivity of 60 %) and  $\beta = 4.71 \times 10^{-6}$ . The dashed curved and open circles were measured with a 14-fold lower value of  $\Gamma_c = 9.82 \times 10^9 \text{ s}^{-1}$  (mirror reflectivity of 98 %) and  $\beta = 4.68 \times 10^{-6}$ .

In Fig. 4.6, the second order correlation function,  $g_2(0)$ , has again been plotted as a function of  $M$ . Both the experimental data and the theoretical treatment show that the threshold shifts only slightly when changing the cavity decay rate,  $\Gamma_c$ . This is due to the dominance of the non-linear damping, which makes the effect of inversion damping almost negligible. As we will explain in the following section this is partly related to the small longitudinal size of our “microchip” laser configuration. In lasers as small as ours,  $\Gamma_c \gg \gamma_2$  unless the mirror reflectivities are very high. In the case of a cavity where  $l_{opt} \approx 600 \mu\text{m}$ ,  $\Gamma_c$  only becomes as low as  $\gamma_2$  for a mirror reflectivity of  $\approx 99.3 \%$ .

For a  $\text{Nd}^{3+}:\text{YVO}_4$  microchip laser such as ours, therefore, the noise dynamics are independent of the cavity mirror except for in the case of very high reflectivities ( $\gtrsim 99.3$ ). Instead, the fluctuations are only affected by the spontaneous emission factor  $\beta$ .

## 4.10 Discussion and conclusion

In this chapter we have limited our description of the class B laser to a linearised model. This model relies on the approximation that the oscillations are very small as compared to the steady state values. Although simple and very powerful, the model should not be valid in the case of very deep anharmonic oscillations. In this regime, deviations from the linearised theory become sizable, especially with respect to the oscillation damping rate and the quantity of fluctuations. Instead of using the linearised model, further insight can be gained by using a Pseudo Energy approach as pioneered by Ogawa [12] and Paoli et al. [13]. This model is

discussed in chapters 5 and 6. A fully analytic *and* practical solution to the problem of class B lasers is yet to be found.

Usually,  $\text{Nd}^{3+}:\text{YVO}_4$  lasers are considered ideal four-level systems. However, when  $\Gamma_c$  and  $\gamma_2$  become comparable in size, the laser dynamics may still be affected by the fast responding lower-level population. This population causes additional damping of the relaxation oscillations, with the non-linear damping  $\gamma_{NL} = (\Gamma_c/\gamma_2) \times \gamma_1(M-1)$  that often even dominates over inversion damping due to the upper-level decay. It may interest the reader that, since  $\Gamma_c$  decreases with increasing laser cavity length (keeping the mirror unchanged,  $\Gamma_c \propto 1/l_{opt}$ ), we find that non-linear damping only becomes important when the laser is made small enough to reach the microscopic limit. Thus, although this is not the most general case, we observe that atomic damping tends to dominate in the mesoscopic limit while non-linear damping becomes dominant in the microscopic limit.

In conclusion, a relatively simple model for the study of relaxation oscillations in class B lasers was presented. Applying this theory to experimental data, it was shown that small class B lasers have ill-defined fluctuation thresholds while the power threshold is still very distinct. With the use of a very flexible cavity configuration, the impact of changing the cavity size and decay rate have both been presented and discussed in relation to the fluctuation threshold. Furthermore, the oscillation rate and damping rate of the relaxation oscillations was studied, showing that linearised theory gives a surprisingly good approximation of the fluctuation properties.

## 4.11 Appendix

In our treatment of the rate equations (see Eq. 4.18 and discussion), which are the same as the ones that appeared in Ref. [5], a few simplifications were made. In this appendix, we will go beyond these simplifications and discuss the consequences of three effects that in principle can significantly alter the laser behaviour. These are

i) *Finite branching ratio*: The population of the upper laser level does not only decay spontaneously to the lower laser level, but also to other levels with a fixed branching ratio. In fact, the diagnostics chapter 3 shows that typical branching ratios are of the order of 50 %. In Eq. 4.29b this effect enters the equation as an additional decay term  $-\gamma'_1 N_1$ . Note that the other decay terms in Eqs. 4.29 that involve  $\gamma_1$  do not change. In these terms, however, the  $\gamma_1$  has to be reinterpreted as the decay to the laser lower level only.

ii) *Frequency detuning*: The coupling of the laser mode with the excited atoms will decrease when the laser frequency is detuned from atomic resonance. In the rate equations this shows up as a reduction of the factor  $\beta$  in the stimulated emission terms present in all three equations. We describe this reduction by introducing a quantity  $\beta' = \beta/(1 + (\Delta\omega/\gamma_{at})^2)$ , where  $\Delta\omega = \omega - \omega_{at}$ , with  $\omega$  the laser frequency, and  $\omega_{at}$  and  $\gamma_{at}$  the frequency and width of the spontaneous emission, respectively.

iii) *Excess noise*: Non-orthogonality of the cavity eigenmodes can enhance the spontaneous emission rate into the lasing mode by an Petermann excess noise factor  $K$ . The associated Langevin noise amplitude is enhanced by a factor  $\sqrt{K}$ . These effects are represented in Eq. 4.29a by a modified spontaneous emission rate  $R'_{sp} = K N_1 \beta' \gamma_1$ , where the excess noise effect is represented by the multiplier  $K$  and the detuning is contained in  $\beta'$ . The modified Langevin noise source  $f'_n$  now satisfies  $\langle f'_n(t) f'_n(t') \rangle = 2R'_{sp} n \delta(t - t')$ .

With the three above corrections, the rate Eqs. 4.18 are modified into:

$$\dot{n} = -\Gamma_c n + \beta' \gamma_1 (N_1 - N_2) n + R'_{sp} + f'_n, \quad (4.29a)$$

$$\dot{N}_1 = S - \gamma_1 N_1 - \gamma'_1 N_1 - \beta' \gamma_1 (N_1 - N_2) n, \quad (4.29b)$$

$$\dot{N}_2 = -\gamma_2 N_2 + \gamma_1 N_1 + \beta' \gamma_1 (N_1 - N_2) n. \quad (4.29c)$$

As before, the inversion noise source has been neglected; the population is adiabatically removed from Eq. 4.29c to yield

$$N_2 = N_1 \frac{\gamma_1(1 + \beta' n)}{\gamma_2 + \gamma_1 \beta' n} \approx \frac{\gamma_1}{\gamma_2} (1 + \beta' n) N_1, \quad (4.30)$$

where the approximation is based on the adiabatic assumption  $\gamma_2 \gg \gamma_1 \beta' n$ . This expression is used to substitute  $N_2$  in the above Eqs. 4.29a and 4.29b.

We linearise about steady state ( $n_0$  and  $N'_{1,0}$ ) to find for the fluctuation dynamics

$$\frac{d}{dt} \begin{pmatrix} \delta n \\ \delta N_1 \end{pmatrix} = \begin{pmatrix} -(\gamma'_n + \gamma'_{NL}) & \beta' \gamma_1 n_0 \\ -\Gamma_c & -\gamma'_N \end{pmatrix} \begin{pmatrix} \delta n \\ \delta N_1 \end{pmatrix} + \begin{pmatrix} f'_n(t) \\ 0 \end{pmatrix}, \quad (4.31)$$

where we have used the substitution  $\gamma_1 N'_{1,0} \beta' \approx \Gamma_c$ . The three (modified) decay rates in the

above matrix equation

$$\gamma'_n = \Gamma_c - \beta' \gamma_1 (N_{1,0} - N_{2,0}) = \frac{R'_{sp}}{n_0} = K \frac{\Gamma_c}{n_0}, \quad (4.32a)$$

$$\gamma'_{NL} = \frac{\gamma_1 \Gamma_c \beta' n_0}{\gamma_2}, \quad (4.32b)$$

$$\gamma'_N = \gamma_1 (1 + \beta' n_0) + \gamma'_1. \quad (4.32c)$$

The modifications to the decay rates, as compared to those given in this chapter, are as follows: The photon damping  $\gamma'_n$  is enhanced by a factor  $K$ . The non-linear damping  $\gamma'_{NL}$  is decreased in the case of frequency detuning since  $\beta' \leq \beta$ . The atomic damping  $\gamma'_N$  splits into a decay rate to the lower laser level ( $\gamma_1 (1 + \beta' n_0)$ ), and additional decay to all other levels ( $\gamma'_1$ ). Also the relaxation oscillation frequency is modified to a value given by

$$\omega_{ro}^2 = \Gamma_c \beta' \gamma_1 n_0 = \Gamma_c (\gamma_1 + \gamma'_1) (M - 1), \quad (4.33)$$

where we have used the (modified) steady state condition

$$n_0 \approx \frac{M - 1}{\beta'} \frac{\gamma_1 + \gamma'_1}{\gamma_1}. \quad (4.34)$$

Since, in the present experiment, there is no frequency detuning ( $\beta' = \beta$ ) and since excess noise has little or no effect ( $K \approx 1$ ), we will now concentrate on the consequences of the finite branching ratio for the analysis presented in this chapter. We start by noting that the measured spontaneous decay rate of  $1.3(1) \times 10^4 \text{ s}^{-1}$  is actually equal to  $\gamma_1 + \gamma'_1$ . Fortunately, this does not affect our estimate for the cavity loss rate  $\Gamma_c$ , which we obtain from the slope of  $\omega_{ro}^2$  versus the pump parameter  $M$  (see Eq. 4.33). However, the presence of  $\gamma'_1$  does affect our estimate for the spontaneous emission factor  $\beta$ . Denoting the true spontaneous emission factor by  $\beta$ , and this chapter's experimental estimate by  $\beta_{exp}$ , the steady state Eq. 4.34 gives a relation

$$\beta_{exp} = \beta \left( \frac{\gamma_1}{\gamma_1 + \gamma'_1} \right) = \frac{M - 1}{n_0} = \frac{\Gamma_c h \nu (M - 1)}{P_{out}}. \quad (4.35)$$

As the literature value for the branching ratio is 0.467 (see chapter 3), the true  $\beta$  must hence be 2.14 times larger than the experimental estimate  $\beta_{exp}$ .

At the end of this appendix, we note (luckily enough) that the reanalysis presented above only affects the  $\beta$  value and not the values for the various damping rates, at least when the damping rates are expressed in terms of  $M$ ,  $\beta_{exp}$  and the total spontaneous decay rate ( $\gamma_1 + \gamma'_1$ ). The new damping rates are

$$\gamma'_n = K \beta_{exp} \frac{\Gamma_c}{M - 1}, \quad (4.36a)$$

$$\gamma'_{NL} = \left( \frac{\gamma_1 + \gamma'_1}{\gamma_2} \right) \Gamma_c (M - 1), \quad (4.36b)$$

$$\gamma'_N = (\gamma_1 + \gamma'_1) M. \quad (4.36c)$$

Thus, since the difference is so small, we will continue using this chapter's notation in the following chapters. Some of the derived rate equations presented here, however, will be used in chapter 8, where we will discuss a laser with excess noise and detuning.



## Chapter 5

### Photon statistics<sup>1</sup>

*We have measured the photon number probability distribution of a laser in which the inversion is not slaved to the field. For the experiments, we have used a  $\text{Nd}^{3+}:\text{YVO}_4$  laser which has a sufficiently slow inversion to allow measurement of the photon fluctuations at a timescale much shorter than that of the relaxation oscillations. The photon distribution function becomes highly nonstandard (i.e. non-Poissonian) in such a laser; this is consistent with available theoretical work. We point out the relevance of our results for the case of the semiconductor microlaser.*

#### 5.1 Background

The photon statistics of a single-mode laser has been studied for more than 30 years [22, 28, 29, 30, 31]. In those days the photon statistics were obtained by adiabatically eliminating the dynamic variables of the gain medium. Over the years, this approximation has given excellent agreement with experimental results. Incorporation of the variables of the gain medium has been considered in some theoretical papers [12, 13] but this work received little attention. Recently, it has been stressed that the validity of adiabatically eliminating the gain medium depends on the size of the laser; conventional laser theory is expected to break down as the laser gets smaller and smaller [5, 32, 27]. This applies when the inversion is slow enough to fulfil the condition  $\gamma_1 < \Gamma_C$ , where  $\gamma_1$  and  $\Gamma_C$  are the inversion and cavity decay rates, respectively. Dramatic deviations from “standard” photon statistics have been predicted for the case  $\Lambda\beta \gtrsim 1$  in the previous chapter, where  $\Lambda \equiv \Gamma_C/\gamma_1$  and  $\beta$  is the fraction of spontaneous emission going into the lasing mode<sup>2</sup>. Since  $\beta$  is roughly proportional to the inverse of the laser mode volume [2], the condition  $\Lambda\beta \gtrsim 1$  is easier fulfilled the smaller the laser is. In view of the present trend of laser miniaturisation, in particular for semiconductor lasers, this deviation from standard photon statistics is a highly relevant issue; it is in fact the theme of this chapter. We report experimental observation of highly nonstandard photon statistics of a  $\text{Nd}^{3+}:\text{YVO}_4$  microchip laser operating under the condition  $\Lambda\beta \approx 1$ , and we interpret these results in the context of available theories [12, 13]. The good agreement allows us to predict similar nonstandard photon statistics for semiconductor lasers operating under the condition  $\Lambda\beta \gtrsim 1$ ; such lasers are already available on a prototype basis [33, 34, 35]. Our

<sup>1</sup>Y. Lien, S. M. de Vries, N. J. van Druten, M. P van Exter, and J. P. Woerdman, “Photon statistics of a laser with slow inversion”, Phys.Rev.Lett. **86**, 2786-2789 (2001).

<sup>2</sup>The definition  $\Lambda = \Gamma_C/\gamma_1$  applies for the ideal four-level laser, i.e.,  $\gamma_2 = \infty$ , where  $\gamma_2$  is the lower level decay rate. In the non-ideal case, an extra damping term is introduced through the population of the lower level. In the case where  $\gamma_2 \ll \Gamma_C$ , the ratio of photonic and atomic damping is not  $\Gamma_C/\gamma_1$  but  $\gamma_2/\gamma_1$  [5]. This is the case for our laser, where  $\Gamma_C/\gamma_2 \approx 70$ .

experimental validation of the generalised theories on the photon statistics [12, 13] is all the more important in view of the fact that standard semiconductor lasers will soon operate in the regime  $\Lambda\beta \gtrsim 1$ .

In technical terms, if we make the usual assumption that the polarisation of the gain medium can be adiabatically eliminated, a laser with  $\Lambda < 1$  is a class A laser whereas  $\Lambda > 1$  corresponds to class B [13]. One may wonder why the photon statistics of a class B laser have not been addressed so far experimentally, in particular for semiconductor lasers for which so much noise data are available. The problem in measuring photon statistics is that one requires high quality time-domain data for faithful sampling of the relaxation oscillations. For semiconductor lasers this implies a time resolution of 100 ps, which is at the border of the present technical possibilities. For this reason we have used a  $\text{Nd}^{3+}:\text{YVO}_4$  microchip laser as an experimental model system; this laser offers a relatively low relaxation oscillation frequency ( $\omega_{ro}/2\pi \approx 10$  MHz) and an extreme class B character ( $\Lambda \approx 10^6$ ). Recently we have studied the second-order moment of the photon distribution of this laser within the context of a linearised theory [5]; this approximation fails when studying the shape of the photon number distribution since linearisation leads by necessity to a Gaussian distribution. It is the shape of the photon distribution of a class B laser that we address in this chapter: this distribution is very different from the predictions of the linearised model, and as we will see below, the distributions also show substantial deviations from a class A distribution.

## 5.2 The intensity statistics

As a reminder, the class A laser, defined by  $\Lambda \ll 1$ , has a photon probability distribution  $P(n)$  given by the generalised Poissonian distribution [20]

$$P(n) = \frac{(p + \bar{n})^{(p+n)} \exp(-p - \bar{n})}{(p + n)!}, \quad (5.1)$$

where  $n$  is the intracavity photon number and  $p$  is interpreted as the number of modes available for spontaneous emission. Equivalently,  $p = 1/\beta$ , where  $\beta$  is the fraction of spontaneous emission going into the lasing mode. For  $p \gg 1$ , we can approximate Eq. 5.1 by using Stirling's expansion for the factorial. This then yields a truncated Gaussian distribution of  $P \approx C \exp(-(n - \bar{n})^2/2(\bar{n} + 1))$ , where  $C$  is a normalisation constant[36]. Above threshold, the parameter  $\bar{n} = p(M - 1)$ , where  $M$  is the pump parameter, approximates the average photon number [20]. For high-intensity beams, where effects due to reflected vacuum fluctuations can be neglected [37] and a semi-classical description suffices,  $n$  is related to the output intensity  $I$  by  $I = n\Gamma_C \hbar\nu$ .

Because of the nonlinear nature of the full class B coupled rate equations, solutions are far from trivial. Both Ogawa [12] and Paoli et al. [13] have put forward theoretical predictions for the photon probability distribution in class B lasers. The two approaches have some common traits but differ at crucial points; however, their results can be represented by the same generic equation, which we will give first, before discussing the differences in derivation,

$$P(n) = C(a, b)n^a e^{-bn}, \quad (5.2)$$

where the normalisation constant  $C(a, b) = b^{(1+a)}/a!$ . The first and second moments of this distribution are given by the parameters  $a$  and  $b$  via  $\bar{n} = (a + 1)/b$  and  $g_2(0) - 1 \approx \delta n^2/n^2 =$



$1/(a + 1)$ . The function  $P(n)$  is thus entirely defined by the two experimentally accessible variables  $\bar{n}$  and  $g_2(0)$ .

### 5.3 The pseudo energy

Paoli et al. [13] use the concept of “pseudo energy” to solve the laser dynamics. The inversion and the intensity are re-expressed in terms of one fast and one slow variable, which are then separated. These variables are the coordinate  $q = \ln(n/n_0)$ , with  $n_0$  as the equilibrium photon number, and the pseudo energy  $W$ , defined by

$$W \equiv \frac{1}{2(M-1)\Gamma_c\gamma_1} \left( \frac{dq}{dt} \right)^2 + V(q), \quad (5.3)$$

where  $M$  is the normalised pump parameter and  $V(q) = e^q - q - 1$  is the Toda potential [13]. The pseudo energy quantifies the strength of the intensity fluctuations; for low noise levels its time average is in fact equal to  $g_2(0) - 1$ . The advantage of the pseudo energy over the true energy is that, in the limit of weak excitation and damping of the noise, the pseudo energy is conserved, whereas the true energy of the system is not. Interestingly, Paoli et al. [13] (and also Ogawa [12]) predict that the photon probability  $P(n)$  goes to zero for  $n/n_0 \rightarrow 0$ , since  $V(q)$  (and thus  $W(q)$ ) diverges in that limit. To obtain an expression for the photon probability distribution, Paoli et al. find themselves forced to expand the probability distribution in terms of the pseudo energy,  $W$ , taking only terms up to the second order. The distribution becomes non-normalisable and remains in principle only valid for small values of  $W$ , i.e., relatively weak relaxation oscillations, a condition that is *not* fulfilled in our experiments.

Also Ogawa [12] makes use of the pseudo energy concept, but he does not invoke the separation of timescales. Moreover, his model corresponds to what Siegman [1] calls an ideal three-level laser (note that lasers which are known as three and four-level systems by experimentalists like Siegman[1], are referred to as two- and three-level systems, respectively, by theoreticians [29, 12]). This model leads to approximately equal population in the two laser levels, whereas a four-level laser like our  $\text{Nd}^{3+}:\text{YVO}_4$  laser has an almost negligible population in the lower level<sup>3</sup>. This could conceivably lead to different noise properties from what is expected in a  $\text{Nd}^{3+}:\text{YVO}_4$  laser. Nevertheless, both Ogawa and Paoli et al. arrive at the same final result, namely Eq. 5.2. This suggests that Eq. 5.2 has generic validity beyond the stringent conditions used in the two derivations [12, 13]. As we will show, our experimental results confirm this hypothesis.

### 5.4 Setup

Our experimental setup is shown in Fig. 5.1. A  $\text{Nd}^{3+}:\text{YVO}_4$  chip with a thickness of 0.1 mm and a doping of 1 % atomic  $\text{Nd}^{3+}$  was put as close as possible to a concave mirror with a radius of curvature of 25 mm and a reflectivity of 80%. The mirror has a diameter of only  $\approx 1$  mm; it is basically a small platform made by the careful removal of the surrounding mirror through grinding (see mirror in Fig. 5.1). The small size was needed to keep the

<sup>3</sup>The relation  $S_P = 4S_D$ , used by Ogawa, is a consequence of the three-level model used in his paper. This is equivalent to  $N_2 = N_1$ . Note that Paoli et al. [13] assume that  $N_1 = 0$ , i.e., a four-level system.

cavity length small and  $\beta$  relatively large. The crystal was optically pumped with an intensity-stabilised titanium-sapphire laser at 809nm, with relative noise below 0.1 % r.m.s.. By using a Fabry-Perot we confirmed that the  $\text{Nd}^{3+}:\text{YVO}_4$  laser was oscillating in a single mode only. The  $\text{Nd}^{3+}$  fluorescence, at 1064 nm, had an almost Lorentzian spectrum with a width (FWHM) of  $\gamma_{\perp}/\pi = 0.22$  THz; this large value allows for adiabatic elimination of the polarisation of the gain medium. The values of  $\beta$  and  $\Gamma_C$  were found directly from the experimental data themselves. Plotting the output as a function of pump parameter and using the relation  $n = (M - 1)/\beta$  yielded  $\beta = 1.8 \times 10^{-5}$ . Furthermore, the value of  $\Gamma_C$  was deduced from the relaxation oscillation frequency  $\omega_{ro} = \sqrt{\Gamma_C \gamma_1 (M - 1)}$ , leading to  $\Gamma_C = 1.05 \times 10^{11} \text{ s}^{-1}$ . The upper level decay rate was measured to be  $\gamma_1 = 1.3(1) \times 10^4 \text{ s}^{-1}$ . Our laser is an extreme class B laser since  $\Lambda = \Gamma_C/\gamma_1 = 8 \times 10^6 \gg 1$  and  $\gamma_2/\gamma_1 = 1.2 \times 10^5 \gg 1$ .

The photon number probability distribution was determined by direct binning of the intensity values observed in an intensity-time trace. With a typical output power of 1 mW, there was no need to use a photon counter; instead we used a DC-coupled 125 MHz photodetector (*NewFocus* 1811) which has a much larger dynamic range than a photomultiplier. Nevertheless, we will refer to intensities in terms of the corresponding intra-cavity photon numbers because of the ease at which this can be related to theory. To obtain high-quality data, we took special care to minimise the background signal since this produces a smearing of the probability distribution through its noise. Therefore, to ensure that the signal was maximised without saturating the detector, the intensity was adjusted for each measurement using a half-waveplate and polariser combination (Fig. 5.1). To obtain high-quality data, we took special care to minimise the background signal since this produces a smearing of the probability distribution through its noise. Therefore, to ensure that the signal was maximised without saturating the detector, the intensity was adjusted for each measurement using a half-waveplate and polariser combination (Fig. 5.1). This made it impractical to employ this detector to measure the absolute intensity, for which another, slower Si photodiode with an adjustable current amplifier was used. The oscilloscope, a *LeCroy* 9304A, had a non-ideal flash-type AD-converter, which introduced extra noise. Some of the intensity bins of the converter had a larger probability to be filled than others and thus, for each pump value,

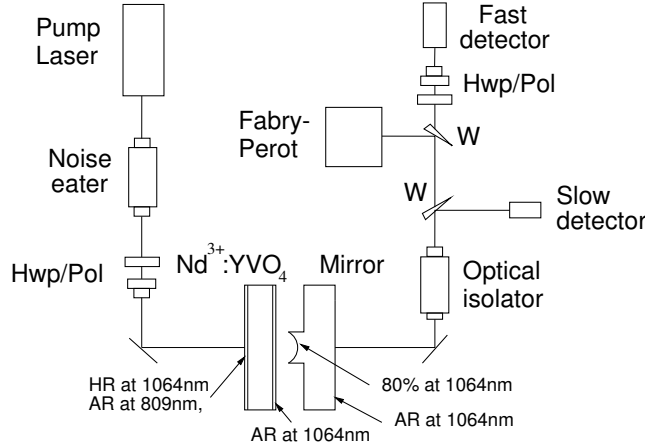


**Figure 5.1:** The setup, with the laser cavity depicted in the bottom of the figure. The cavity, which is not drawn to scale, is shown with the remodelled concave mirror. *W* indicates a Wedge, and *Hwp/Pol* is a half-waveplate and polariser combination used for the adjustment of the light intensity. *AR* and *HR* denote an anti-reflection and a high-reflection ( $\approx 100\%$ ) coating respectively.

ten measurements at various oscilloscope offsets were conducted in order to average out this effect.

## 5.5 Experimental results

The photon number probability distribution is shown in Fig. 5.2, where the experimentally obtained data are compared to the theoretical curves according to Eq. 5.2. Since the variables  $a$  and  $b$  (Eq. 5.2) are already set by the measured values of  $\bar{n}$  and  $g_2(0)$ , the comparison is a test of the shape of the curves. Fig. 3 shows that the experimental data are in excellent agreement with theory. Smearing of  $P(n)$  due to the noisy dark signal can only be seen in Fig. 5.2a, where the sharp drop in probability at very small photon numbers is somewhat diffuse in the experimental data (see inset).

It is instructive to compare the shapes of the  $P(n)$  curves in Fig. 5.2 with those for a class A laser. Fig. 5.2a may remind the reader of the thermal photon statistics of a class A laser below threshold; however, it is obtained here *above* threshold ( $M = 1.04$ ) at an average photon number  $\bar{n} = 1750$ ; its nature is due to the relaxation oscillation enhanced spontaneous emission noise [5].

Jumping now to Fig. 5.2c, we observe at  $M=7.28$  a curve that is approximately Gaussian, as applies to a class A laser sufficiently far above threshold, *but* with an anomalously large width. At this point a class A distribution would have a standard deviation  $\sigma_n \approx \bar{n}^{1/2} = 642$ , while the measured standard deviation is  $\sigma_n = 80500$ , i.e., 125 times larger! This is due to the extreme class B behaviour of our laser; for lasers that are only marginally class B, the distribution is narrower; furthermore, lasers with marginal class B properties retain their Gaussian shape (such as depicted in Fig. 5.2c) till closer towards threshold. Apart from a somewhat larger width, these marginal class B lasers have photon probability distributions that are indistinguishable from those of class A lasers.

Fig. 5.2b shows an intermediate case, which for a class A laser would correspond to a truncated Gaussian as shown by the dashed curve. As can be seen, the class B distribution deviates strongly from this truncated Gaussian; this is shown in more detail in Fig. 5.3 where two sections of Fig. 5.2b have been enlarged. Whereas there is a finite probability of having zero photons in the cavity in the class A case, class B theory predicts that there will be zero probability of having no photons in the cavity (this holds true, even very close to threshold such as in Fig. 5.2a, where the probability drop is very abrupt just above zero photons). This prediction is confirmed by our experimental results. In Fig. 5.3 the dashed curves represent the Gaussian photon probability distribution of a class A laser, chosen with  $\bar{n}$  and  $g_2(0)$  equal to those of the class B distribution, here shown by drawn curves. Note also how the upper tail extends much further for the class B distribution; this is due to the non-linearisable nature of the class B laser dynamics.

## 5.6 Discussion and conclusion

Despite the a priori weaknesses of the theories [12, 13] discussed above, they are highly successful in predicting the probability distribution. The use of a three-level system by Ogawa [12] is apparently appropriate for a four-level laser. This surprising result is consistent with the finding of Levien et al. [25] that the differences in the noise of a three-level system and a four-level system are sometimes smaller than anticipated. The approximation of Paoli et al.

[13] that  $W$  remains relatively small also seems better than expected. In the framework of pseudo energy this could be explained by a spurious drift term [38], which leads to an extra damping of the intensity fluctuations and a reduction in  $W$ , thus effectively increasing the region of validity for the low  $W$  approximation.

In conclusion, our experiment confirms the theoretical predictions [12, 13] for a class B laser, and shows that these theories apply surprisingly far beyond the parameter ranges of nominal validity. Our findings are significant for all class B lasers, in particular for semiconductor microlasers with  $\Lambda\beta \gtrsim 1$ , where we expect to see photon number statistics that are equivalent to those described here [5, 32]. In pioneering work, microdisk and microring semiconductor lasers have already crossed the limit  $\Lambda\beta \gtrsim 1$  [33, 34, 35]: reference [33] has a

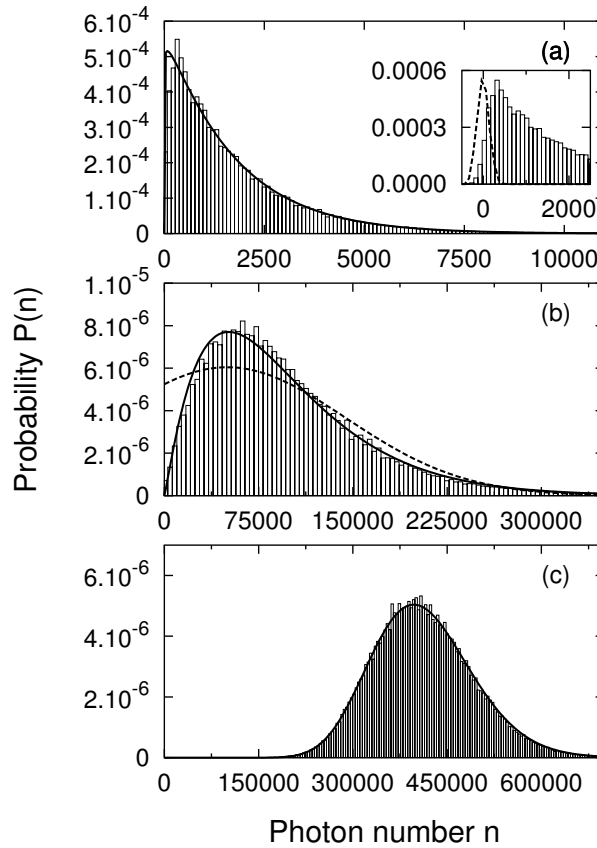


**Figure 5.2:** The photon probability distribution for three different pump values: (a)  $M=1.04$ , (b)  $M=2.85$ , (c)  $M=7.28$  with the experimental data shown as bar graphs. The full curves represent the theoretical predictions based on the measurement of  $g_2(0)$  and  $\bar{n}$ , and the dashed curve in (b) shows a class A distribution with the same value of  $g_2(0)$  and  $\bar{n}$  as the experimental data. The inset in (a) shows the distribution of the background (dark) signal as a dashed curve. The characteristic values for these graphs are (a)  $g_2(0)=1.96$ ,  $\bar{n}=1750$ ; (b)  $g_2(0)=1.47$ ,  $\bar{n}=96600$ ; (c)  $g_2(0)=1.038$ ,  $\bar{n}=413000$ .

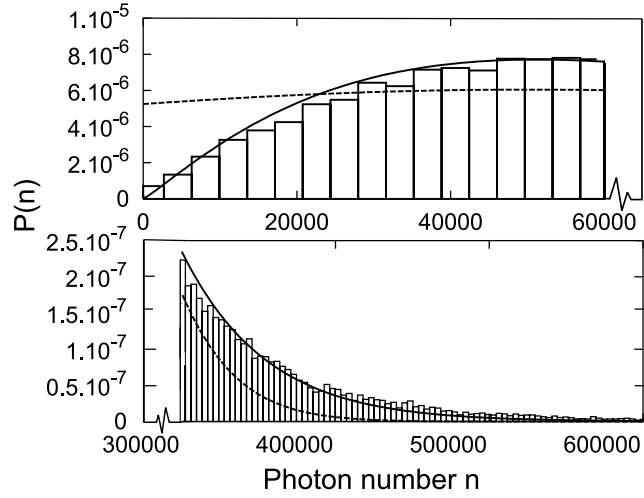


**Figure 5.3:** Enlargement of two sections of Fig. 5.2b: again a comparison of the experimental data with the theoretical curves for the class B model (solid line) and the class A model (dashed line). The two curves have the same values for  $g_2(0)$  and  $\bar{n}$  as the experimental data.

value of  $\Lambda\beta$  that equals  $\approx 2 \cdot 10^2$ . It would therefore be very interesting to study the intensity characteristics of these devices; so far, only DC properties have been reported. For more common semiconductor lasers (edge-emitting and vertically-emitting devices), the  $\Lambda\beta \gtrsim 1$  criterion has not yet been satisfied since typically  $\Gamma_C \approx 300 \text{ ns}^{-1}$ ,  $\gamma_1 \approx 3 \text{ ns}^{-1}$ ,  $\beta \approx 10^{-4}$  so that  $\Lambda\beta \approx 10^{-2}$ . However, since the dominance of class B properties is mainly a question of laser size [5, 32, 27], the non-standard photon statistics emphasised in this chapter will become obvious once these lasers are made an order of magnitude smaller. Especially close to threshold, deviations from class A photon statistics should become visible even *before*  $\Lambda\beta \gtrsim 1$  is reached as an onset towards extreme class B behaviour.

## 5.7 Acknowledgements

The author is grateful to R. Loudon for his confirmation of the statement regarding the Gaussian intensity distribution of all class A lasers.



## Chapter 6

# The laser as a Toda oscillator<sup>1</sup>

*The Toda oscillator model gives a true description of the intensity fluctuations of a laser. Here, we use this model to study lasers with strongly developed relaxation oscillations. Via a separation of timescales, we focus on the theoretical and experimental investigation of the instantaneous relaxation oscillation frequency and damping rate. As an experimental system, the Nd<sup>3+</sup>:YVO<sub>4</sub> laser is used.*

### 6.1 Introduction

An essential ingredient of standard laser theory is that the intensity fluctuations are strongly damped above threshold. However, very many lasers, such as rare-earth doped solid-state lasers and most semiconductor lasers, do not have stable intensities but exhibit relaxation oscillations that are driven by fluctuating spontaneous emission. To first order, these oscillations are well-described by linearisation about the point of intensity stabilisation, but once the oscillations get stronger, this approximation is stretched beyond its validity range. In this chapter we will analyse the relaxation oscillations by using the Toda model. This model is a generalisation of standard laser theory, and is particularly well-suited for our purpose. Although the theory of the Toda oscillator has already been known for some time in the context of laser physics [12, 13], we present here what is to our knowledge the first experimental work carried out with this model specifically in mind.

Generally speaking, lasers with relaxation oscillations have relatively slow inversion decay rates. These lasers are commonly known as class B lasers, which distinguish themselves from class A lasers by fulfilling the condition  $\Lambda = \Gamma_c/\gamma_1 > 1$ , where  $\Gamma_c$  and  $\gamma_1$  are the cavity and inversion decay rates respectively [3] (see section 3.2 for discussion of the nomenclature). Since the relaxation oscillations are driven by spontaneous emission noise, they are relatively strong if the fraction  $\beta$  of spontaneous emission going into the lasing mode is large. Especially in the regime  $\Lambda\beta \gtrsim 1$ , recent study (see chapter 4 as well as [5, 32, 27]) shows that the intensity fluctuations can become as large as the mean intensity. Since  $\beta$  is inversely proportional to the cavity size [2], this regime is reached by reducing the size of the laser.

To gain an understanding of the intensity fluctuations described above, we employ the Toda oscillator model. By rewriting the laser rate equations, we map the problem onto that of a mechanical oscillator consisting of a single particle, trapped in a so-called Toda potential [39]; the particle is set into oscillation by noise. One of the key concepts of this model is the pseudo energy, which is a measure for the depth of the relaxation oscillations and which is

<sup>1</sup>Y. Lien, S. M. de Vries, M. .P. van Exter and J. P. Woerdman, “Lasers as Toda oscillators”, J. Opt. Soc. Am. B **19**, 1461-1466 (2002).

almost conserved in a weakly-damped system. The introduction of this quantity allows for a separation of the photon and inversion dynamics into fast relaxation oscillations with an amplitude that evolves slowly in time.

## 6.2 The “anharmonic” oscillator

Most laser theories apply to class A lasers, which fulfil the condition  $\Lambda = \Gamma_c/\gamma_1 < 1$ . The difference between class A and class B lasers becomes apparent when studying the time evolution of the lasers. In class A lasers, the inversion is sufficiently fast to be adiabatically eliminated and it is thus slaved to the photon number. In class B lasers on the other hand, the inversion and photon numbers oscillate approximately out of phase in potentially strong relaxation oscillations.

This noise behaviour is usually the strongest in small lasers; but in spite of the very smallest lasers being semiconductor lasers, these are not yet small enough to fulfil the noise criterion  $\Lambda\beta \gtrsim 1$  (although it is believed that they will reach this regime in the near future [32, 33, 40]). The  $\text{Nd}^{3+}:\text{YVO}_4$  laser, however, *does* satisfy the above condition when made sufficiently small and lossy; this is due to its extremely slow upper level decay rate  $\gamma_1$ . Such a  $\text{Nd}^{3+}:\text{YVO}_4$  laser, which has a four-level scheme as depicted in Fig. 6.1, will be the experimental basis of this chapter.

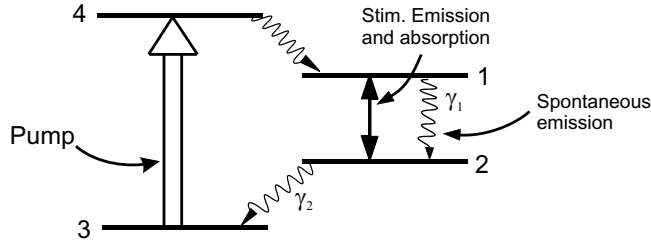


**Figure 6.1:** The  $\text{Nd}^{3+}:\text{YVO}_4$  laser is a four-level laser, with a pump wavelength of 809 nm and an emission wavelength of 1064 nm.

The Toda model is based on a second-order differential equation that can be deduced easily from the rate equations if either the optical field or the polarisation is adiabatically eliminated (the so-called “bad-cavity” or “good-cavity” approximations). In our case, we eliminate the polarisation (see section 6.5 for justification) to obtain the following four-level rate equations [5]

$$\frac{dn}{dt} = \gamma_1\beta n\Delta N - \frac{\Gamma_c}{n_0}n - \frac{\Gamma_c}{\gamma_2}\gamma_1\beta n(n - n_0) + \Gamma_c + \sqrt{2\Gamma_c n}\xi(t), \quad (6.1a)$$

$$\frac{d\Delta N}{dt} = \gamma_1(1 + \beta n)\Delta N - \Gamma_c(n - n_0) + \Gamma_c\frac{\gamma_1}{\gamma_2}[n - n_0 + \beta(n - n_0)^2], \quad (6.1b)$$

where  $n$  and  $N$  are the photon and inversion numbers, respectively;  $n_0$  and  $N_0$  are the corresponding steady-state values and  $\Delta N = N - N_0$ . These steady state values satisfy  $\Gamma_c/n_0 \approx \Gamma_c/(n_0 + 1) = \Gamma_c - \gamma_1\beta N_0$ , where  $\Gamma_c/n$  denotes the inherent photon damping of



the relaxation oscillations. This damping arises because the decay rate  $\Gamma_c$  of the optical field is not fully compensated by the stimulated emission rate  $\gamma_1\beta N_0$  (there is also spontaneous emission present). A finite lower-level decay rate  $\gamma_2$  gives rise to two terms that can be recognised through the  $\gamma_2$ . The  $\gamma_2$  terms in Eq. 6.1b are, however, negligible as compared to the other coupling term  $\Gamma_c(n - n_0)$  since  $\gamma_2 \gg \gamma_1$ . The Langevin noise source is denoted by  $\xi(t)$  with  $\langle \xi(t)\xi(t+\tau) \rangle = \delta(\tau)$ .

The two first-order equations (Eq. 6.1a and Eq. 6.1b) can be combined into a single second-order differential equation. This rewrite yields

$$\frac{d^2n}{dt^2} - \frac{1}{n} \left( \frac{dn}{dt} \right)^2 + 2\gamma_{ro}(n) \frac{dn}{dt} + \omega_{ro}^2(n) (n - n_0) = f(t), \quad (6.2a)$$

$$\gamma_{ro}(n) = \frac{1}{2} \left[ \frac{\Gamma_c}{n} + \gamma_1(1 + \beta n) + \frac{\Gamma_c}{\gamma_2} \gamma_1 \beta n \right], \quad (6.2b)$$

$$\omega_{ro}^2(n) = \Gamma_c \gamma_1 \beta n, \quad (6.2c)$$

where  $\gamma_{ro}(n)$  and  $\omega_{ro}(n)$  are the “instantaneous” relaxation oscillation damping and frequency. The Langevin noise source  $f(t) = \sqrt{2R_{sp}n} \xi(t)$  represents the fluctuations in the spontaneous emission rate, acting only on  $n(t)$ . Eq. 6.2a is similar to the equation for a noise-driven, damped harmonic oscillator except for three important differences. For one, the damping rate  $\gamma_{ro}(n)$  is a function of the *instantaneous* photon number  $n$ . Similarly, the anharmonic restoring force  $\omega_{ro}^2(n)$  is also a function of  $n$ . Finally, there is an additional term proportional to  $(dn/dt)^2$ ; this term generates higher-order harmonics.

A first-order solution can be found by assuming that  $(n - n_0) \ll n_0$  so that the relaxation oscillation damping and frequency remain approximately constant. This gives the linearised forms for the two rates:

$$\tilde{\gamma}_{ro} = \frac{1}{2} \left[ \frac{\Gamma_c \beta}{(M - 1)} + \gamma_1 M + \Gamma_c \frac{\gamma_1}{\gamma_2} (M - 1) \right], \quad (6.3a)$$

$$\tilde{\omega}_{ro} = \sqrt{(M - 1) \Gamma_c \gamma_1}, \quad (6.3b)$$

where  $M = 1 + \beta n_0$  is equivalent to a pump parameter when the laser is sufficiently far above threshold. Far above threshold, the first term of Eq. 6.3a can be neglected, and the relaxation oscillation damping rate is set by the lower level decay rate  $\gamma_2$  if  $\gamma_2 \ll \Gamma_c$ ; in this case the definition of a class B laser changes from  $\Lambda = \Gamma_c/\gamma_1 \gg 1$  to  $\tilde{\Lambda} = \gamma_2/\gamma_1 \gg 1$  [5, 40]. From here on, the standard route is to reduce the problem to that of a simple harmonic oscillator by using the linearising assumption underlying Eq. 6.3, which also implies that  $(dn/dt)^2$  is negligible as compared to the  $(d^2n/dt^2)$  term in Eq. 6.2a. In this chapter, we will show how one can go beyond this standard route.

### 6.3 Pseudo energy

In order to find (semi-)analytical solutions of Eq. 6.2, it is advantageous to introduce the anharmonic “Toda potential”. This potential is found by rewriting Eq. 6.2a in terms of a

coordinate  $q = \ln(n/n_0)$ , and by neglecting, for the time being, the noise and damping contributions in this equation. This yields

$$\frac{1}{(M-1)\Gamma_c\gamma_{\parallel}} \frac{d^2q}{dt^2} = -(e^q - 1) = -dV(q)/dq. \quad (6.4)$$

where the Toda potential  $V(q)$  is defined as

$$V(q) = e^q - q - 1, \quad (6.5)$$

where  $V(q=0) = 0$  is the minimum. Note that of the three nonlinearities mentioned before, the first one ( $\gamma_{ro}(n)$ ) has been neglected, the second has been removed through the coordinate transformation, and the third one is incorporated in the non-linearity of the Toda potential. The Toda potential has been plotted in Fig. 6.2; as one can see, it is asymmetric as well as

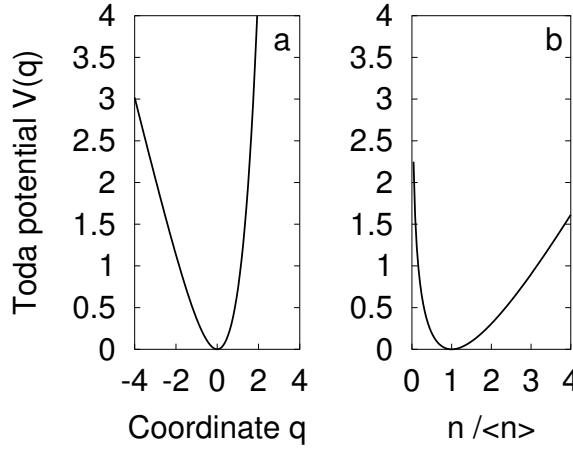


**Figure 6.2:** The Toda potential in terms of the coordinate  $q$  on the left and re-expressed in terms of the photon number on the right.

anharmonic. In Fig. 6.2a it has been plotted in terms of the coordinate  $q$ , whereas Fig. 6.2b shows the potential in terms of the photon number to indicate how the photon dynamics will be affected. After having defined the Toda potential, a quantity called the pseudo energy  $W$  is introduced as [13]

$$W(t) \equiv \frac{1}{2(M-1)\Gamma_c\gamma_1} \left( \frac{dq}{dt} \right)^2 + V(q), \quad (6.6)$$

where the first and second terms are the kinetic and potential pseudo energies, respectively. The expression  $1/[(M-1)\Gamma_c\gamma_1] \equiv (\tilde{\omega}_{ro}^2)^{-1}$  plays a role equivalent to mechanical mass, where  $\tilde{\omega}_{ro}$  is the linearised relaxation-oscillation frequency introduced in Eq. 6.3b. The pseudo energy is a measure for the fluctuations in relative intensity or  $q$ ; each value of the pseudo energy  $W$  corresponds to a specific relaxation oscillation depth, frequency and waveform. As long as the relaxation oscillations are neither damped nor driven, this pseudo energy will remain constant. This means that the time development of the pseudo energy  $W$ , which

is on the timescale of the relaxation oscillation damping rate  $\gamma_{ro}$ , can be seen entirely separate from the individual oscillations that evolve on the much faster timescale of the relaxation oscillation frequency  $\omega_{ro}$ . It is this separation of  $W$  from  $q$  that simplifies the problem sufficiently to yield (semi-)analytical solutions beyond the linearised regime. An example of the separation of timescales can be seen in section 6.6 below, where typical time traces for both intensity and pseudo energy have been plotted.

## 6.4 Damping and oscillation rate

The relaxation oscillation damping rate can be found relatively straightforwardly in the limit of small fluctuations. In this case, the Toda potential can be rewritten as a harmonic potential  $V(q) = e^q - q - 1 \approx \frac{1}{2}q^2$  and the coordinate  $q$  can be reformulated as the photon number deviation from the steady state value ( $q = \ln(n/n_0) \approx (n - n_0)/n_0$ ). With this approximation, it is no surprise that the autocorrelation function of the pseudo energy can be written as

$$\langle W(t)W(t + \tau) \rangle = \langle W \rangle^2 (1 + e^{-2\tilde{\gamma}_{ro}\tau}), \quad (6.7)$$

where  $\tilde{\gamma}_{ro}$  is the linearised relaxation oscillation damping rate as defined in Eq. 6.3. Although Eq. 6.7 was found in the limit of small, linearised fluctuations, below we use the agreement with experimental results to show that this equation also applies in the case of large fluctuations.

One of the key points in this chapter is that it is in general impossible to deduce the relaxation oscillation damping rate from a measurement of the intensity noise spectrum alone. The reason for this is the anharmonic nature of the (Toda) potential, or equivalently the dependency of  $\omega_{ro}$  on photon number. The increase of the relaxation oscillation period  $t_c$  with modulation depth can be expressed as (see Eq.2.20 in Ref. [13]):

$$\tilde{\omega}_{ro}t_c = 2\pi(1 + \frac{1}{12}W + ..). \quad (6.8)$$

In the spectral domain the non-constant oscillation period leads to a broadening  $\delta\omega_{ro}$  of the principal harmonic. Restricting ourselves to the first order we obtain a rough estimate for this broadening:

$$\delta\omega_{ro} \approx \tilde{\omega}_{ro}\bar{W}/12, \quad (6.9)$$

where the time-averaged pseudo energy is given by

$$\bar{W} = \frac{\Gamma_c\beta}{2\tilde{\gamma}_{ro}(M-1)}. \quad (6.10)$$

The broadening  $\delta\omega_{ro}$  comes in addition to the intrinsic spectral width caused by the damping of the relaxation oscillations.

## 6.5 The setup and experimental parameters

For the experiments, we have used a  $\text{Nd}^{3+}:\text{YVO}_4$  chip with a thickness of  $\approx 100 \mu\text{m}$  and a doping of 1 % atomic  $\text{Nd}^{3+}$  together with various outcoupling mirrors (see Fig. 6.3). On one side the crystal was coated to be highly reflective at 1064 nm and anti-reflective at

809 nm, while on the opposite facet it had a 1064 nm anti-reflection coating. All experiments described here were conducted with the  $\text{Nd}^{3+}:\text{YVO}_4$  laser operating in a single transverse and longitudinal mode. Single mode operation was easily achieved owing to the short length of the cavity and the strong curvature of the mirror. This ensured large longitudinal and transverse mode splitting. In addition, the spatial confinement of the pump strongly favoured the  $\text{TEM}_{00}$  mode. Since we are interested in the effect of the magnitude of the spontaneous emission factor  $\beta$  on the laser noise, we varied the optical cavity length from  $\approx 300 \mu\text{m}$  to  $\approx 1200 \mu\text{m}$  (here we have accounted for a crystal refractive index of  $n_e = 2.17$  at 1064 nm). The mirror depicted in Fig. 6.3 had the edges ground away to leave a small platform only; this enabled us to make the air section of the cavity very short (about  $\approx 75 \mu\text{m}$  at the shortest). The mirror was concave with a radius of curvature of 25 mm and had a reflectivity of 80 % at the lasing wavelength. We pumped the laser with an intensity-stabilised titanium-sapphire laser at 809 nm. The relative noise of this pump was below 0.1 % r.m.s., which is effectively negligible (in particular since the fluctuation bandwidth of the pump laser was 5 kHz, i.e. much smaller than  $\omega_{ro}/2\pi \approx 10$  MHz). Owing to the relatively large splitting of the levels, the effect of thermal photons was also negligible. The data were collected with a LeCroy 9450 digital oscilloscope and a Tektronix 2712 spectrum analyser. The oscilloscope could record as many as 50000 intensity-time points; its time window was chosen to measure a minimum of 20 points per oscillation cycle. Up to twenty separate time traces were taken for each pump value and the data presented below are averages of these results. We established the

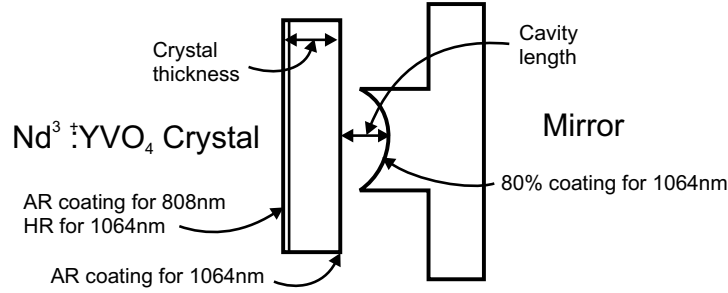


**Figure 6.3:** The  $\text{Nd}^{3+}:\text{YVO}_4$  laser consists of a crystal with reflective and anti-reflective coatings and a spherical mirror. The edges of the spherical mirror were ground away to produce a small platform with a diameter of 1 mm, which allows the mirror to be moved closer to the crystal.

following laser parameters for use in the rate equations: the  $\text{Nd}^{3+}$  fluorescence at 1064 nm had an almost Lorentzian spectrum with a width (FWHM) of  $\gamma_{\perp}/\pi = 0.22(2)$  THz. This is much larger than the cavity decay rate  $\Gamma_c$ , thus validating the adiabatic elimination of the polarisation that we described in section 2. The value of  $\beta$  was found directly from the output versus input power curve [5], while the product  $\Gamma_c\gamma_1$  was determined from the linearised relaxation oscillation frequency  $\tilde{\omega}_{ro}$  (see Eq. 6.3b). The upper-level decay rate was measured directly from the fluorescence decay and was found to be  $\gamma_1 = 1.3(1) \times 10^4 \text{ s}^{-1}$ . Another important variable is the lower-level decay rate  $\gamma_2$ , for which References [10] and [9] quote values in the range of  $1 - 2 \times 10^9 \text{ s}^{-1}$ . The lower level decay rate  $\gamma_2$ , which was obtained by fitting Eq. 6.7 to the experimental data reported in section 6, was found to be in reasonable

agreement with literature<sup>2</sup>.

## 6.6 Experimental results

Our experimental results are based on high-quality time traces, from which the pseudo energy can be calculated by the use of Eq. 6.6. Since the pseudo energy  $W$  changes at a very slow timescale as compared to the photon number, it is not necessary to calculate it for all intensity points. Instead, we have chosen to extract  $W$  only at the relaxation oscillation extrema (peaks and troughs); at these points all the pseudo energy is stored in the oscillator as “potential energy” and it can thus be easily found. A section of a typical timetrace for the oscillating laser intensity and the calculated pseudo energy is displayed in Fig. 6.4. As a consequence

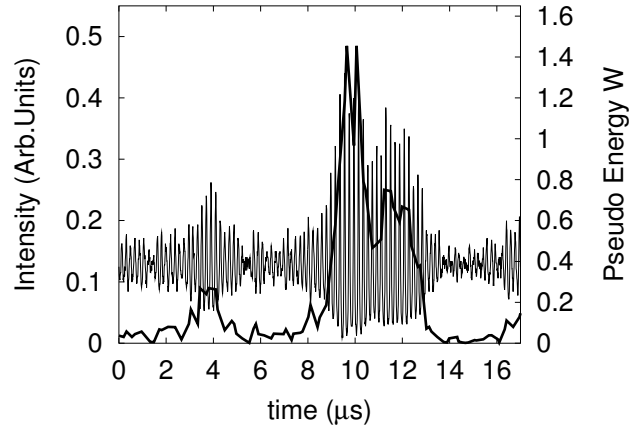


**Figure 6.4:** A typical timetrace of the laser intensity (thin curve). The pseudo energy (thick curve) is related to the relaxation oscillation amplitude; it changes on the timescale of the relaxation oscillation damping, which is slow compared to the oscillation frequency.

of being a measure for the relaxation-oscillation depth, the pseudo energy also dictates the frequency and the shape of the oscillations, which become anharmonic when the pseudo energy becomes large. This relationship is illustrated in Fig. 6.5, where we have plotted two enlarged sections of Fig. 6.4 with different pseudo energies (see caption for details). For comparison, the dotted curves depict the theoretical curves given by Eq. 6.4 and solved with an iterative solution method. The relaxation oscillations are clearly well-described by the theoretical framework. Fig. 6.5a demonstrates the almost harmonic nature of the oscillations in the limit of weak modulations; Fig. 6.5b shows how the oscillations become slower and more anharmonic when the pseudo energy increases. The frequency reduction at increased modulation depth was found to be consistent with the theoretical predictions (Eq. 6.9 predicts that oscillations with  $W = 1$  should be about 8 % slower than for  $W \approx 0$ ).

<sup>2</sup>We found values of the lower level decay rate  $\gamma_2$  in the range  $1.7 - 2.4 \times 10^9 \text{ s}^{-1}$  when varying the cavity length from  $300 \text{ μm}$  to  $1200 \text{ μm}$ . These variations in the estimate of  $\gamma_2$  suggest that a gain grating caused by back-reflected standing waves caused extra damping; see Ref. [41].

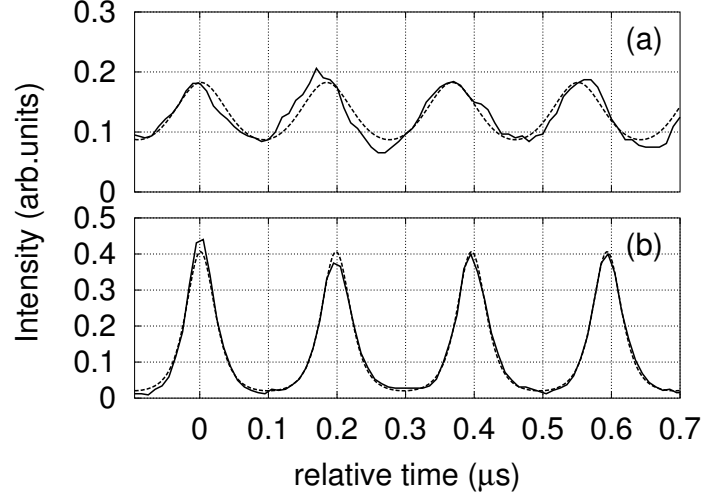


**Figure 6.5:** Two sections of Fig. 6.4, magnified to show how the oscillation magnitude affects the shape and frequency of the oscillations. The solid curves represent the experimental data, whereas the broken curves depict the theoretical predictions obtained from Eq. 6.4. Fig. 6.5a is centred on  $\approx 6.8 \mu\text{s}$  and Fig. 6.5b is on  $\approx 10.3 \mu\text{s}$  of Fig. 6.4. The theoretical curves have pseudo energies  $W = 0.068$  and  $W = 1.00$ , respectively. As expected the oscillations become slower and more anharmonic with increasing pseudo energy.

The magnitude of the intensity fluctuations depends on the laser size and pump strength. This dependence is shown in Fig. 6.6, where the average pseudo energy  $\bar{W}$  has been plotted for two different cavity lengths: a “short” cavity with a length  $l \approx 300 \mu\text{m}$  and a measured  $\beta = 9.9 \times 10^{-6}$ , and a “long” cavity with  $l \approx 1200 \mu\text{m}$  and a measured  $\beta$  of  $2.3 \times 10^{-6}$ . Note how the average pseudo energy  $\bar{W}$  starts at  $\approx 1$  at the lasing threshold and gradually drops for increasing pump strength. As might be expected from section 6.1, the laser with the short cavity is noisier than the long-cavity laser (see Fig. 6.6). This is due to a relatively large factor  $\tilde{\Lambda}\beta = 1.05$ , thus putting this laser further into the class B regime than the long-cavity laser ( $\tilde{\Lambda}\beta = 0.28$ ). As discussed in relation with Eq. 6.3, we have used  $\tilde{\Lambda} = \gamma_2/\gamma_1$  instead of  $\Lambda = \Gamma_c/\gamma_1$  in our description of the class B behaviour.

We mentioned above (section 6.4 and discussion of Fig. 6.5) that the relaxation-oscillation damping rate can *not* be found directly from the intensity spectrum. Instead we deduce this damping rate using the Toda oscillator model. We start with analysing the dynamics of the pseudo energy by calculating its time-autocorrelation from timetraces like the one shown in Fig. 6.4. A typical result is plotted in Fig. 6.7 together with a fit using Eq. 6.7. From autocorrelation timetraces such as the one plotted in Fig. 6.7, estimates for the relaxation-oscillation damping rate  $\tilde{\gamma}_{ro}$  were obtained.

For each pump value, we averaged over the estimates for  $\tilde{\gamma}_{ro}$  to plot the relaxation-oscillation damping rate as a function of pump strength (see Fig. 6.8). Although Eq. 6.7 and Eq. 6.3a have been proven only in the weak-oscillation regime, we nevertheless find that theory compares favourably with the experimental results in all regimes. Since we have used only the envelope of the oscillations to find the damping rate, the result is not affected by

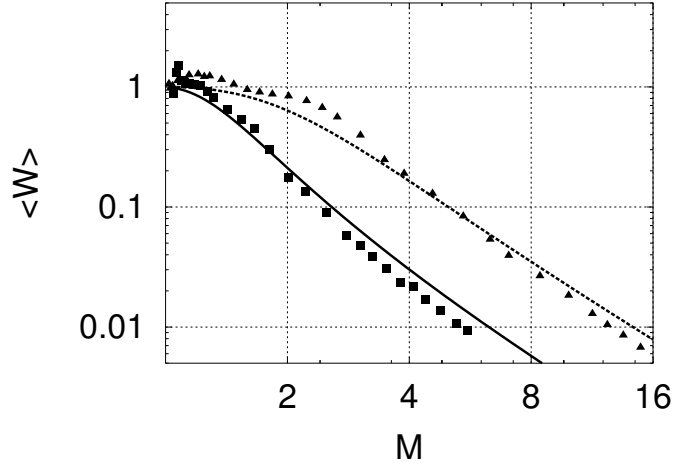


**Figure 6.6:** The average pseudo energy  $\bar{W}$  as a function of the pump parameter  $M$ . The points represent the experimental data, the curves are the theoretical predictions for  $\bar{W}$  (Eq. 6.10). The parameters used for the theoretical curves were obtained from independent experiments. The triangles and the broken curve correspond to a cavity with a length of  $l \approx 300 \mu\text{m}$ ; the squares and the solid line represent a cavity with a length of  $l \approx 1200 \mu\text{m}$ .

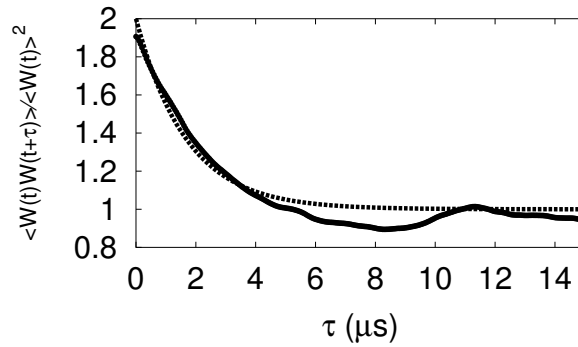


**Figure 6.7:** The pseudo energy autocorrelation function typically decays within a few microseconds. The solid curve shows the time development of the autocorrelation function, while the broken curve is the theoretical fit.

other factors such as anharmonicity.

Fig. 6.8 deserves some further discussion; it shows the measured relaxation-oscillation damping rate as a function of the pump parameter  $M$  for the two cavity configurations described in conjunction with Fig. 6.6. Naïvely, the damping rate could be obtained by measuring the width of the principal harmonic of the intensity spectrum. However, this measurement is misleading since the harmonic is broadened through the varying oscillation frequency. While the open circles represent the spectral measurement, the solid circles show the damp-

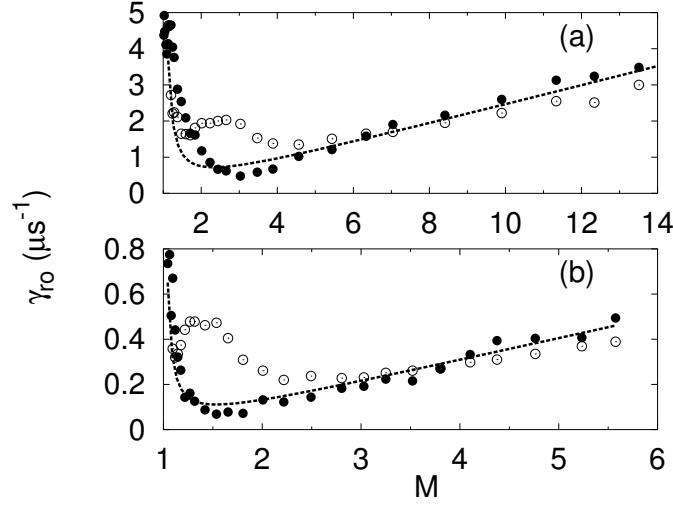


**Figure 6.8:** Relaxation-oscillation damping rate  $\gamma_{ro}$  as a function of  $M$ ; in (a)  $l = 300 \mu\text{m}$ , in (b)  $l = 1200 \mu\text{m}$ . The open circles represent the width of the principal harmonic in the intensity noise spectrum, which thus also includes an extra broadening due to the changing oscillation frequency. The solid circles show the damping rate as obtained by analysing the time dynamics of the pseudo-energy theory. The theoretical curves are based on the linearised theory result of Eq. 6.3a.

ing obtained when using the Toda oscillator approach. It is the separation of timescales that has allowed us to find the true damping rate, since we are now insensitive to the amplitude dependence of the relaxation oscillation frequency. We note that this separation is very robust (provided that  $\omega_{ro} \gg \gamma_{ro}$ ) and works far into the nonlinear regime, i.e. also for  $W \approx 1$ . However, theoretical complexities makes it difficult to go formally beyond the expansion in Eq. 6.8. Also,  $\gamma_{ro}$  quickly increases when approaching threshold (from above), leading quickly to violation of the condition  $\omega_{ro} \gg \gamma_{ro}$ .

By calculating the difference between the two damping rates depicted in 6.8, we obtain a quantitative estimate for the broadening in the intensity noise spectrum caused by the amplitude dependency of the oscillation frequency. This experimental result can then be compared to Eq. 6.9 which gives a rough estimate for the additional width of the principal harmonic. The theoretical estimate is based on the first-order expansion of Eq. 6.8, and is in qualitative agreement with the broadening (see Fig. 6.9), without using any free parameters. As can be seen from the graph, both the overall magnitude and the peak shift have been qualitatively accounted for. The extra broadening  $\delta\omega_{ro}$  is the largest for intermediate pump strengths (see also Eq. 6.9), where *both*  $\bar{W}$  and  $\omega_{ro}$  are sizeable. Comparing the results for the different cavity lengths, we find that if the laser is relatively small, the broadening  $\delta\omega_{ro}$  remains large until further above threshold. This is an example of how the class B properties manifest themselves more strongly in small lasers [5, 27].



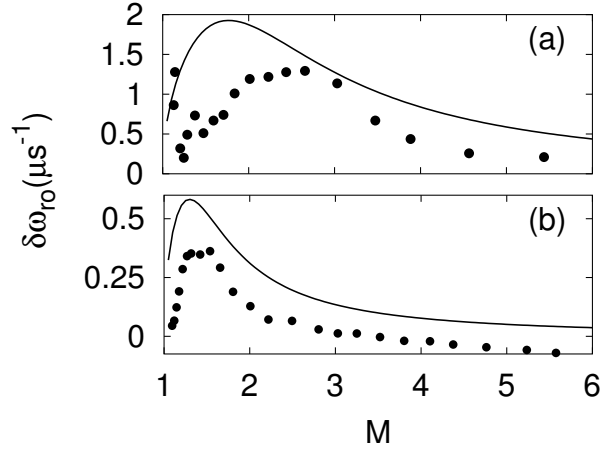


**Figure 6.9:** The broadening of the main harmonic due to the pseudo-energy dependency of the oscillation frequency, here for two different cavity lengths of the laser. The data points were obtained by subtracting the width as given by linearised theory from the measured width of the principal harmonic. As in Fig. 6.6, the curves represent theoretical estimates for which the parameters have been separately obtained. The upper figure (a) depicts the short cavity results ( $l \approx 300\mu\text{m}$ ), the bottom figure (b) corresponds to the long cavity ( $l \approx 1200\mu\text{m}$ ).

## 6.7 Concluding discussion

We have made a first theoretical and experimental study of a laser operating in the Toda oscillator regime. The Toda oscillator model describes the dynamics of the system through the separation of timescales. These timescales correspond to the relaxation oscillation frequency and damping rate, and their separation allows for a study of the damping rate without contributions due to frequency variations. In addition, the model has been applied successfully to estimate the noise strength in the laser, and to describe the anharmonic shape of the deep oscillations. We have emphasised the importance of laser size for the intensity fluctuations; extreme class B properties such as deep intensity modulations are stronger in small laser systems and are observed until further above threshold.



## Chapter 7

---

### Ring modes -Combining gain and index guiding<sup>1</sup>

*The effect of quadratic index guiding and Gaussian gain guiding on the transverse mode profiles in Nd<sup>3+</sup>:YVO<sub>4</sub> microchip lasers is investigated. We concentrate on the regime where the two guiding mechanisms are comparable in size, observing the transition from the index-guided regime to the gain-guided regime. Excellent agreement is found between experiment and theory, both in the far and near fields.*

#### 7.1 Introduction

End-pumped microchip lasers are in common use due to their simplicity of fabrication and the ease at which they can be frequency doubled. In most practical applications, these lasers are made from monolithic crystals with highly reflective coatings at the lasing wavelength. Such laser cavities have planar mirrors and the transverse eigenmodes are not determined by the mirror curvature but by the weak guiding effects introduced by the pump. In these lasers, the optical end pump leads to both a gain guide and a thermally induced index guide. As an alternative to the monolithic cavity, planar crystals are often combined with concave mirrors.

A thermal index guide can be due to a temperature-induced change in refractive index, or a heating-related curvature of the crystal surface. Except for in planar monolithic cavities, thermal guides are weak, and they can therefore often be neglected, at least when compared to other guiding mechanisms such as index guiding due to curved mirrors. However, when they are considered, the resulting weak index guide can reasonably be approximated to the lowest non-vanishing order, which is the quadratic index guide [42, 43].

The gain guide tends to dominate over the index guide in three-level lasers [44]. However, in four-level lasers such as in Nd<sup>3+</sup> doped systems, gain guiding is usually relatively weak. This is due to the fact that intra-cavity photons outside the pumped area are not absorbed as they are in three-level lasers. Depending on the curvature of the cavity mirrors, if any, it follows that gain- and index guiding can be of comparable size in four-level lasers as is the case in the transitional regime studied in this chapter.

The regime of similar gain- and index-guiding regime is also very interesting from a noise point of view. Recently, Druten et al. [45] showed that the noise strength can display resonant behaviour at specific combinations of gain- and index guiding. In chapter 8 we will discuss how this so-called *excess* quantum noise [46, 47, 48, 49] arises in a configuration that is very similar to the one used in this chapter.

---

<sup>1</sup>N. J. van druten, S. S. R. Oemrawsingh, Y. Lien, C. Serrat and M. P. van Exter, "Observation of transverse modes in a microchip laser with combined gain and index guiding", J. Opt. Soc. Am. B **18**, 1793-1804(2001).

In our experiment, we used a Titanium Sapphire pump laser with Gaussian intensity profile and a planar crystal combined with a weakly-curved convex mirror to study the combination of Gaussian gain-guiding and quadratic index-guiding. A large set of transverse modes, whose intensity profiles vary with mirror reflectivity, are observed both in the near and the far fields. We find that these modes differ significantly from the usual Laguerre-Gaussian modes, especially for low mirror reflectivities where conical emission is observed with several rings in the far field and no rings in the near field. Also the effect of tuning the cavity length is investigated and compared to our numerical results. The theoretical model is kept simple: we neglect for example non-linearities such as spatial hole burning and temporal effects due to the slow inversion behaviour of our class B laser (see chapter 4). Despite these approximations we find excellent agreement with theory.

## 7.2 Theoretical model

Although the experiments of this chapter were conducted with a planar crystal and a concave mirror, this is only one of several equivalent configurations to which theory [50] for combined gain- and index-guiding applies. In Fig. 7.1 we present three equivalent cavities. Our theoretical model is based on the planar monolithic cavity (Fig. 7.1a) to which the two other cavities are reduced using the relations given in Ref. [50]. Assuming a cavity of length  $L$  and a cavity base refractive index  $n_0$ , we consider the changes to the refractive index  $\Delta n = \Delta n_R + \Delta n_g$ , which constitute a quadratic index guide  $\Delta n_R$  and a (complex-valued) Gaussian gain guide  $\Delta n_g$ , where  $\Delta n_g$  is assumed to be proportional to the pump intensity. Since we account for neither spatial nor temporal hole burning, the model, strictly speaking, only applies just above threshold.

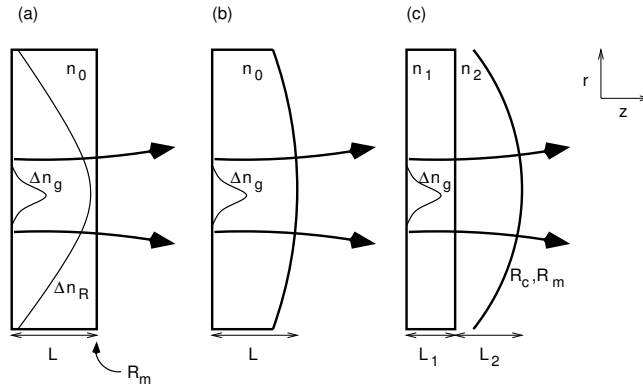


**Figure 7.1:** (a) Cavity configuration considered in the theoretical model: a longitudinally homogeneous system with length  $L$ , with a transverse quadratic index guide  $\Delta n_R$  and a Gaussian gain guide  $\Delta n_g$ . The arrows in this figure indicate the output of the microchip laser through the end mirror with reflectivity  $R_m$ . Configurations (b) and (c) are equivalent as long as the longitudinal variation of the mode profile may be neglected. (b) a monolithic cavity with a gain guide  $\Delta n_g$ , and a curved surface. (c) The cavity configuration used in the experiments: a crystal gain medium, with a transverse Gaussian gain profile, and a separate concave mirror, with radius of curvature  $R_c$  and reflectivity  $R_m$ .

For our model, we unfold the standing-wave cavity and treat it as a waveguide of length  $2L$  with the optical wave travelling in a single direction only. Expressing the paraxial wave equation in terms of cylindrical coordinates  $\mathbf{r}(r, \phi, z)$ , we obtain

$$\left[ \nabla_r^2 + 2k_z^2 \left( \frac{\Delta\omega}{\omega_{at}} + \frac{\Delta n}{n_0} \right) \right] u = -2ik_z \frac{\partial u}{\partial z}, \quad (7.1)$$

where

$$\nabla_r^2 = \frac{\partial^2}{\partial r^2} + \frac{1}{r} \frac{\partial}{\partial r} + \frac{1}{r^2} \frac{\partial^2}{\partial \phi^2} \quad (7.2)$$

is the usual transverse Laplacian. Also,  $u(\mathbf{r})$  is the slowly varying envelope of the (monochromatic) electric field component of the electromagnetic field  $E(\mathbf{r})$ , which has a wave vector  $k_z = n_0\omega_{at}/c$  in the  $+z$  (longitudinal) direction and is related given by

$$E(\mathbf{r}) = u(\mathbf{r})e^{-i(\omega t - k_z z)}. \quad (7.3)$$

Cavity detuning is given by  $\Delta\omega = \omega - \omega_{at}$ , where  $\omega_{at}$  is the spontaneous emission frequency (in radians). As is natural in the paraxial approximation, we assume that the guiding  $\Delta n(\mathbf{r}) = n(\mathbf{r}) - n_0 \ll n_0$  and that  $\Delta\omega \ll \omega$ .

Explicitly, the guiding  $\Delta n = \Delta n_R + \Delta n_g$  can be written as

$$\Delta n_R(\mathbf{r}) = -\frac{2n_0 r^2}{k_z^2 w_0^4}, \quad (7.4)$$

and

$$\Delta n_g(r, \Delta\omega) = -\frac{cg(\mathbf{r}, \Delta\omega)}{2\omega_{at}}, \quad (7.5)$$

with

$$g(r, \Delta\omega) = g_0 \exp(-2r^2/w_g^2) \frac{i - \Delta\omega/\gamma_{at}}{1 + (\Delta\omega/\gamma_{at})^2}, \quad (7.6)$$

where  $w_0$  is the modal waist width due to the quadratic index-guide,  $w_g$  is the width of the Gaussian gain-guide, and  $g_0$  denotes the gain per unit length at the peak of the Gaussian pump.

At this point it is interesting to investigate the effect of detuning on the gain-guide  $\Delta n_g$ . The imaginary part of Eq. 7.6 denotes the gain itself and is (by definition) the strongest for zero detuning. The gain-related index-guide, which is the real part of Eq. 7.6, is important to the transverse mode structure. We know that extending the cavity by a length  $\Delta L$  gives a negative frequency detuning  $\Delta\omega = -\omega_{at}(\Delta L/L)$ . In a longer cavity, a gain-related index change is therefore negative in the centre of the pump spot, which again leads to less focussing of the mode and presumably a bigger mode profile. It is the differing behaviour of the gain guide and the index-related gain guide that leads, as we will see, to the the complex ring modes for positive (in  $\Delta L$ ) detuning. The effect of detuning on the gain and the gain-related index guide has been plotted in Fig. 7.2 as a function of detuning  $\Delta\omega/\gamma_{at}$ .  $\text{Nd}^{3+}:\text{YVO}_4$  is homogeneously broadened with a FWHM of  $\gamma_{at}/\pi = 215$  GHz (see page 17).

It is convenient to rescale the transverse coordinate  $r$  to  $\rho = r/w_0$ . The paraxial wave equation (Eq. 7.1) now becomes

$$\left[ -\frac{1}{2} \nabla_\rho^2 + 2\rho^2 + z_0 g \right] u = 2iz_0 \left[ \frac{\partial u}{\partial z} - \frac{in_0 \Delta\omega}{c} u \right], \quad (7.7)$$

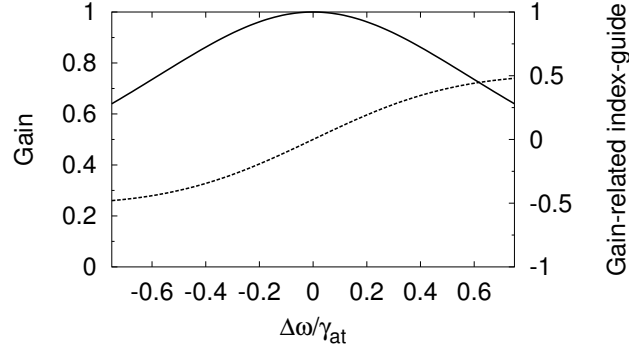


**Figure 7.2:** The effect of detuning on the gain (full curve, scaled on the left) and the gain-related index guide (broken curve, scaled on the right). The two y-axes are not to scale.

with

$$\nabla_{\rho}^2 = \frac{\partial^2}{\partial \rho^2} + \frac{1}{\rho} \frac{\partial}{\partial \rho} + \frac{1}{\rho^2} \frac{\partial^2}{\partial \phi^2}, \quad (7.8)$$

the rescaled transverse Laplacian, and  $z_0 = k_z w_0^2/2$ , the Rayleigh range corresponding to the waist size  $w_0$ . The mode amplitude  $u$  is now considered as a function of  $\rho$  instead of  $r$ . Because the guiding of Eqs. (7.4)-(7.6) has cylinder symmetry, Eq. (7.1) is separable in cylindrical coordinates. In addition, since the gain is maximum on axis, higher-order angular-momentum modes, which have zero intensity on axis, will not be significant, and we can thus limit the analysis to the lowest-order (angular-momentum) modes, eliminating the  $\phi$  dependence [50].

The transverse mode structure depends on the terms on the left hand side of Eq. (7.7) as there are no radially-dependent terms on the equation's right side. The key to the transverse behaviour,  $z_0 g$ , contains three (dimensionless) parameters: these are the zero-detuning on-axis gain per Rayleigh range  $z_0 g_0$ , the ratio between the waists  $w_g/w_0$  and the scaled detuning  $\Delta\omega/\gamma_{at}$ . By setting the right side of Eq. (7.7) equal to  $\mu u$ , we can express the  $z$ -dependency of the eigenfunction as

$$u_{\mu}(\rho, z) = u_{\mu}(\rho, 0) \exp[i(n_0 \Delta\omega/c - \mu/2z_0)z]. \quad (7.9)$$

We now impose the boundary condition that the lowest-loss eigenmode reproduces after one round trip. Considering the round trip mirror reflectivity  $R_m$  we now need

$$\sqrt{R_m} E_0(z + 2L) = E_0(z). \quad (7.10)$$

Inserting Eq. (7.3) and then Eq. (7.9) yields

$$\mu = 2z_0 \left( k_z + \frac{n_0 \Delta\omega}{c} - \frac{\pi m}{L} - \frac{i}{4L} \ln R_m \right), \quad (7.11)$$

where the integer  $m \gg 1$  is the longitudinal mode index. Thus, if the laser is at threshold, the imaginary part of the eigenvalue  $\text{Im } \mu$  is set by the mirror reflectivity only. The real part  $\text{Re } \mu$  is dictated by the requirement that the phase shift during a round trip is a multiple of  $2\pi$ .

The phase shift can be tuned by adjusting the length of the cavity. Expanding the cavity length  $L$  around  $L_0$  and the mode index  $m$  around  $m_0$ , which have been chosen so that  $k_z = \pi m_0/L_0$ , we obtain

$$\frac{2\Delta L}{\lambda_{\text{at}}} = \left[ -\frac{\Delta\omega}{\omega_{\text{FSR}}} + \tilde{m} + \frac{L_0 \text{Re } \mu}{2\pi z_0} \right], \quad (7.12)$$

where  $\Delta L = L - L_0$  and  $\tilde{m} = m - m_0$ .  $\omega_{\text{FSR}} = \pi c/n_0 L_0$  is the free spectral range of the cavity.

The transverse eigenvalue problem (left hand side of Eq. 7.7) is theoretically approached most naturally by fixing the parameters  $z_0 g_0$ ,  $w_g/w_0$  and  $\Delta\omega/\gamma_{\text{at}}$ . The eigenvalues  $\mu$  and the eigenfunctions  $u(\rho)$  can then be found numerically. Experimentally, however, it is the values  $\text{Im } \mu$  and  $\Delta L$  that are fixed. Fixing  $\Delta L$  also defines the relationship between  $\text{Re } \mu$  and  $\Delta\omega$  (see Eq. (7.12)). The boundary conditions set by Eq. (7.11) have to be considered when solving the eigenvalue equation.

Hence, we specify the values  $w_g/w_0$  and  $z_0 \ln(R_m)/L_0$  in the experimental setup, with the former corresponding to the relative narrowness of the pump and the latter being set by the mirror reflectivity. The modal gain  $\text{Im } \mu$  is now found directly from Eq. (7.11). The transverse mode structure at threshold is calculated numerically by allowing  $g_0$  (instead of  $\text{Im } \mu$ ) and  $\text{Re } \mu$  to vary and by using the boundary condition that  $u(\rho)$  vanishes for  $\rho \rightarrow \infty$ . This allows us to find the threshold pump powers and the mode profiles of the individual modes. For each solution the near-field intensity profile  $I(r)$  is given simply by  $I(r) \propto |u(\rho)|^2$ , while the far field profile is obtained by performing the conversion integral

$$I(\theta) \propto \left| \int_0^\infty u(\rho) J_0(k_z w_0 \rho \theta) d\rho \right|^2, \quad (7.13)$$

where  $J_0$  is the zeroth-order Bessel function of the first kind.

Most importantly, the theoretical treatment presented here extends the theory of Serrat et al. [50] by including the effect of tuning the cavity length. This is a theme that is highly significant for the following chapter. The main difference between the model presented here and other models on rare-earth microchip lasers [51, 52, 53] is our inclusion of the parabolic index guide (in addition to the gain-related index guide). The other models, on the other hand, often include the effects of gain medium saturation (and in some cases other radial gain distributions).

### 7.3 Mirror reflectivity and guiding

One of the key points of this chapter (and Ref. [50]) is the fact that the relative importance of the parabolic index guide as compared to the gain-related guiding is determined by the mirror reflectivity. This can be understood as follows: since the laser reflectivity determines the gain needed to reach threshold (imaginary part of Eq. (7.11)), it follows directly that cavities with large mirror reflectivities need less gain to reach threshold. Conversely, if the mirror reflectivity is low, gain guiding will be comparable or stronger than the parabolic index-guide. The effect of the mirror enters Eqs. 7.9 and 7.11 through  $\text{Im } \mu = -z_0 \ln R_m/2L$ , which denotes the modal gain per Rayleigh length: it is found that the parabolic index guide dominates when  $\text{Im } \mu \ll 1$  and that the gain guide dominates in the case where  $\text{Im } \mu \gg 1$ .

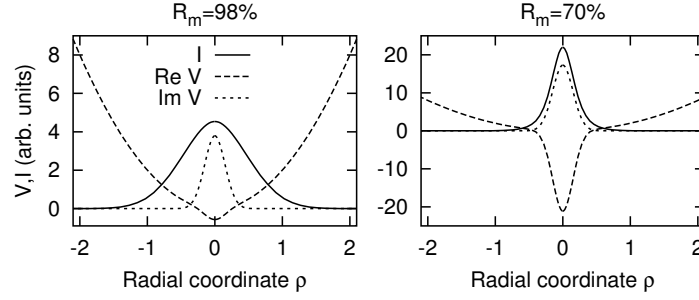


**Figure 7.3:** Transverse profile of the real (dashed line) and imaginary (dotted) part of the guiding “potential” for  $w_g/w_0 = 0.30$ . We have plotted the transverse mode profile of the lowest-loss eigenmode (solid line, with the vertical scale adjusted for each plot) for comparison. Detuning was set to the point at which the threshold is the lowest. (a)  $\text{Im } \mu = 0.36$  (corresponding to  $R_m = 98\%$  in the experiment), the parabolic part (the mirror curvature) of the real-valued index guide dominates. (b) For  $\text{Im } \mu = 6.3$  ( $R_m = 70\%$ ), the Gaussian guide dominates, as it confines the mode to a region where the parabolic index guide is relatively small. Note the difference in vertical scale (for  $V$ ) between (a) and (b).

The two regimes have been illustrated in Fig. 7.3 for  $w_g/w_0 = 0.30$ , which is the case studied in sections 7.4 and 7.5 of this chapter. Both the real (long-dashed curve) and the imaginary part (short-dashed curve) of the potential  $V(\rho) = 2\rho^2 + z_0 g$  were plotted. Both on the right and on the left, detuning was set to be the point at which the system would reach threshold first. Next to the various forms of guiding, the near-field intensity (solid curve) of the lowest-loss (fundamental) eigenmode has been shown. While the curves on the left correspond to  $\text{Im } \mu = 0.36$  and a mirror reflectivity  $R_m = 98\%$  in our system, the curves on the right represent a reflectivity of  $70\%$  and  $\text{Im } \mu = 6.3$ .

It is interesting to note the differences between the two plots in Fig. 7.3. On the left hand side, the refractive index is dominated by the quadratic index guide and the contribution of the gain-related index guide adds only a small dimple at  $\rho = 0$ . The lowest-loss eigenmode was hence only confined by the quadratic index guide. The detuning at which these curves were plotted, was slightly negative in length (positive in frequency).

On the right hand side of Fig. 7.3, it is the gain-related guiding effects that dominate. Here the imaginary part of the potential is much larger as compared to the plot on the left, but it is the real part that is enhanced the most. The reason for this is the fact that this cavity is detuned even more from gain maximum (towards larger positive  $\Delta\omega$ ). Such a large detuning is advantageous in cavities with strong gain guiding as additional focussing of the laser eigenmodes improves the overlap with the gain profile, thereby lowering the lasing threshold.

As already noted in the introduction, in this chapter we will be particularly interested in the intermediate regime ( $\text{Im } \mu \approx 1$ ) where the parabolic index guide and the gain-related guiding are of similar strength. The experimental setup was specifically designed to address this regime.



## 7.4 Experimental setup

As was discussed by Serrat et al. in Ref. [50], the configuration shown in Fig. 7.1(a) can be mapped onto the configurations of Fig. 7.1(b) and (c), as long as the cavity length is shorter than the Rayleigh range of the cavity modes involved. Experimentally, the configuration of Fig. 7.1(c), consisting of a separate laser crystal and a concave mirror was preferred since it allows both flexibility and good control over the guiding parameters. For instance, the strength of the effective quadratic index guide is determined by the curvature of the concave mirror and its distance to the crystal [cf. Eqs. (7.14a)-(7.14c) below, and also the discussion in section 7.6].

The cavity used in the experiments is shown in some more detail in Fig. 7.4. The laser crystal is a 1% doped Nd:YVO<sub>4</sub> chip of  $3 \times 3 \times 0.21(3)$  mm. The left facet in the figure has an anti-reflective coating at the pump wavelength, 808 nm, and it is highly reflective at the lasing wavelength, 1064 nm. The other facet is coated anti-reflective at 1064 nm. An out-coupling mirror with a radius of curvature of  $R_c = 200$  mm and a diameter of 10 mm is placed as close as possible to the latter end, leaving only a small air gap between the crystal and the mirror.

The distance between laser crystal and output coupler could be varied with a micrometer-based translation stage. In practice, the air gap was first minimised until the mirror touched at the edge of the crystal holder (diameter: 5 mm), and then moved back a sufficient distance to allow for fine alignment of the relative tilt. The resulting size of the air gap is estimated from the translation stage read-out to be  $0.10(3)$  mm, where the uncertainty is mainly due to variations in the alignment procedure.

The use of a separate output coupler allows for its easy replacement for another. Hence we can study the same cavity configuration with different out-coupling intensity reflectivities, i.e. different intra-cavity losses. Five different reflectivities  $R_m$  were used: 98 %, 94 %, 90 %, 80 %, and 70 %. The laser crystal was mounted on a piezo-electric transducer (a piezo), so that the cavity length could be fine-tuned on the subwavelength scale.

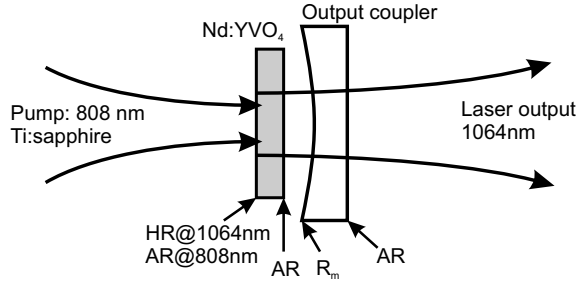


**Figure 7.4:** The experimental setup of the microchip laser. The plano-concave configuration is end pumped using a Titanium Sapphire at 808 nm. The crystal is about 200  $\mu$ m thick with a refractive index of 2.2 and the air gap has a length of 0.1 mm. The radius of curvature of the output coupler is 200 mm. We can vary the reflectivity by replacing the output coupler for another with the same radius of curvature.

The microchip laser is pumped by a *Coherent* 899 Titanium Sapphire laser operating at 808 nm. The Titanium Sapphire laser itself is being pumped by a *Spectra Physics* Millennia laser operating at 532 nm. The transverse profile of the pump is Gaussian and has a waist

size  $w_g = 14 \mu\text{m}$  in the focus, which was on the crystal. The pump power incident on the  $\text{Nd}^{3+}:\text{YVO}_4$  crystal was varied using a combination of a rotatable half-wave plate and a polariser in the collimated part of the pump beam. Typical pump powers were in the 1 – 50 mW range.

The transverse profile of the output beam of the microchip laser was studied by imaging the near field or the far field onto a HiSIS22 CCD camera, using calibrated two-lens imaging systems. The estimated resolution of the imaging system was  $3 \mu\text{m}$  for the near field and  $0.2 \text{ mrad}$  for the far field. Optical-quality beamsplitters were used to reduce the intensity of the light incident on the camera to within its dynamic range. The camera was custom-modified by replacing the original CCD device with a Kodak KAF-0440L CCD which had an anti-blooming system and (more importantly) which did not have a glass window in front of the chip. Avoiding this glass window eliminates optical interference effects originating from the reflection of the glass surfaces; this was found to significantly improve the quality of the images obtained. The size of the chip is  $768 \times 512$  pixels, where the physical size of one pixel is  $9 \times 9 \mu\text{m}^2$ ; the camera is capable of producing 16 bit grayscale images. The resulting mode profiles were generally found to have excellent circular symmetry. For comparison with the theoretical mode, a cross-section was taken along the long (768 pixel) axis of the CCD chip through the centre of the mode profile.

To map the experimental parameters for the configuration of Fig. 7.1(c) onto those of the theoretical model based on Fig. 7.1(a), we use Eqs. 7.14a, 7.14b and 7.14c from the paper of Serrat et al. [50]. For convenience, these are reproduced here in the present notation, namely

$$n_0 = \sqrt{n_1 n_2 \left( \frac{n_1 L_1 + n_2 L_2}{n_2 L_1 + n_1 L_2} \right)} \quad (7.14a)$$

$$L = \sqrt{\left( \frac{L_1}{n_1} + \frac{L_2}{n_2} \right) (n_1 L_1 + n_2 L_2)} \quad (7.14b)$$

$$w_0^2 = \frac{2}{k_z} \sqrt{L R_c n_0}. \quad (7.14c)$$

Variable	Description	Value
$L_1$	Crystal thickness	0.21(3) mm
$n_1$	Crystal refractive index	2.1652
$L_2$	Size of the air gap	0.10(3) mm
$n_2$	Refractive index of air gap	1
$R_c$	Mirror radius of curvature	200 mm
$w_g$	Gain(=pump) waist size	14(1) $\mu\text{m}$
$\lambda_{\text{at}}$	Laser output wavelength	1064 nm
$\gamma_{\text{at}}/\pi$	FWHM of the gain	207 GHz
$L$	Effective length	0.3 mm
$n_0$	Effective refractive index	1.7
$w_0$	Waist size of parabolic index guide	46 $\mu\text{m}$

**Table 7.1:** Overview of the experimental parameters and the corresponding values of the derived theoretical parameters.

An overview of all the relevant parameters of the laser used in the experiment is given in

Table 7.1, including the model parameters derived using Eq. (7.14a)–Eq. (7.14c). Note that the gain waist size  $w_g$  is indeed smaller than the waist size  $w_0$  for the parabolic index guide,  $w_g/w_0 = 0.30$ .

The output of the laser was investigated spectrally by passing it through a planar Fabry-Perot interferometer. The laser was found to operate in a single transverse and longitudinal mode for all the data presented in section 7.5. By operating the laser further above threshold, and carefully tuning the cavity length close to the point of a longitudinal mode switch, it was possible for two longitudinal modes to oscillate simultaneously. This allowed us to determine the longitudinal mode spacing as  $0.27(3)$  THz, where the estimated variation is mainly due to the fact that the cavity needed to be rebuilt for the different mirror reflectivities. This value is consistent with the theoretical value based on the numbers in Table 7.1,  $\omega_{\text{FSR}}/2\pi = c/2n_0L = 0.29$  THz. Note that the longitudinal mode spacing is somewhat larger than the gain bandwidth  $\gamma_{\text{at}}/\pi$ . This situation is typical for practical rare-earth microchip lasers, and is favourable for single-mode operation.

In the case of the mirror with 90 % reflectivity, it was also possible, under a very limited set of cavity and pumping conditions, to have two transverse modes oscillating simultaneously. The estimated transverse-mode frequency splitting was  $3(2)$  GHz, where the uncertainty is mainly determined by the difficulty of obtaining stable simultaneous oscillation in two transverse modes. This value is in rough agreement with the calculated value of 1.3 GHz.

## 7.5 Results

### 7.5.1 Modal thresholds

In order to compare the theoretical mode profiles to the experimental ones, it is necessary to know which of the modes will be lasing. Thus, in this section we first discuss the modal thresholds, i.e. the pump power needed to bring each mode to threshold. We will discuss the modal thresholds as a function of cavity detuning and reflectivity. This also serves as a qualitative overview of the various regimes involved. Later, in section 7.5.2 we will compare and discuss the theoretical and experimental transverse-mode profiles.

An overview of the threshold behaviour as a function of cavity detuning is shown in Fig. 7.5. The left-hand side shows theoretical results, obtained through the methods described in 7.2 for the five different reflectivities used in the experiments. Each curve in the graphs represents the pump power needed to bring a particular mode to the lasing threshold. Note that this has been plotted such that the highest curve corresponds to the mode with the lowest lasing threshold. Each curve is smooth and when two curves cross, a different mode has the lowest threshold and will become the lasing mode. The lowest-loss transverse modes from adjacent longitudinal-mode manifolds [cf. Eq. (7.12)] have also been plotted, to indicate the free spectral range. The right-hand side of Fig. 7.5 shows experimental results of the laser output power (i.e., *not* the threshold power) as a function of the cavity length. These were taken with the pump power fixed at a value close to the point where lasing over the entire free spectral range was just observed.

Although strictly speaking the left-hand and right-hand side of Fig. 7.5 should not be directly compared, we do expect to see very similar behaviour. When the laser is operated not too far above threshold, as in the experimental data of Fig. 7.5, the output power will usually be proportional to how far above threshold the laser is operated [1]. As long as the

laser remains single-mode (i.e., as long as the saturation is sufficiently homogeneous, both spatially and spectrally), we thus expect the experimental output power curve to follow the topmost curve of the calculated modal thresholds. A crossing of the theoretical curves should result in a discontinuous derivative of the experimental curve as the laser performs a “mode switch” (accompanied by a sudden change in transverse mode profile, as will be discussed extensively below).

Comparing the theoretical and experimental data in this way, we indeed see very similar behaviour for each of the reflectivities. In addition, the modal behaviour shows the signature of a transition from index-guiding-dominated at high reflectivities to gain-guiding dominated at low reflectivities. At high reflectivity there are many modes with similar modal gains, but only the lowest-order modes (e.g. in the case of  $R_m = 98\%$  the two modes shown in Fig. 7.5) have sufficient overlap with the localised gain to become the lowest-loss mode for a particular detuning.

For the lower reflectivities, Fig. 7.5 shows just a single smooth curve. In this case higher-order modes actually have much higher threshold, and this reflects the strong mode-discrimination that is typical for gain-guiding [50].

At intermediate reflectivities higher-order modes appear towards positive cavity-length detuning, each in a rather narrow range of cavity detunings. This effect is caused by the gain-related index guide and will be discussed in some more detail in section 7.5.2. Figure 7.5 illustrates that the intermediate regime is of special interest: it exhibits features that are present neither in the index-guiding-dominated regime nor in the gain-guiding dominated regime. Note also that in all cases the lowest threshold is achieved for a cavity detuning away from gain maximum towards shorter cavity length, corresponding to  $\Delta\omega > 0$ , as already discussed for Fig. 7.3.

Apart from the general qualitative agreement between theory and experiment in Fig. 7.5, there are also quantitative differences. At 98 % reflectivity, the theory predicts two possible modes, but the experiment shows no discontinuities, just one mode. At 94 % and 90 %, the theory also predicts more modes than the experiment shows (5 versus 3 and 6 versus 4, respectively). The modes that do not appear in the experiment are the last few higher order modes in the calculations. This deviation and possible causes for it will be discussed more extensively in section 7.6. We have verified that varying the theoretical parameters within the range allowed by experimental uncertainties is insufficient to resolve the discrepancy. The above comparison is only possible at positive cavity detunings where the higher-order modes appear. In contrast, it is almost impossible to determine from Fig. 7.5 whether theory and experiment differ significantly for negative cavity detunings.

### 7.5.2 Modal profiles

We now come to the main topic of this chapter: to compare the calculated and experimental transverse modal profiles for each reflectivity. As a pragmatic solution to the systematic deviation between theory and experiment noted in section 7.5.1, we have taken the following approach: for the reflectivities of 98 %, 94 % and 90 %, it was found that the profiles did not depend sensitively on cavity detuning (provided, of course that the detuning did not induce a mode hop). For these reflectivities we compare the experimentally observed modes with their theoretical counterparts at the cavity detuning that corresponds to the highest laser output and the lowest threshold.

At lower reflectivities (80 % and 70 %), the modal profiles change continuously as a

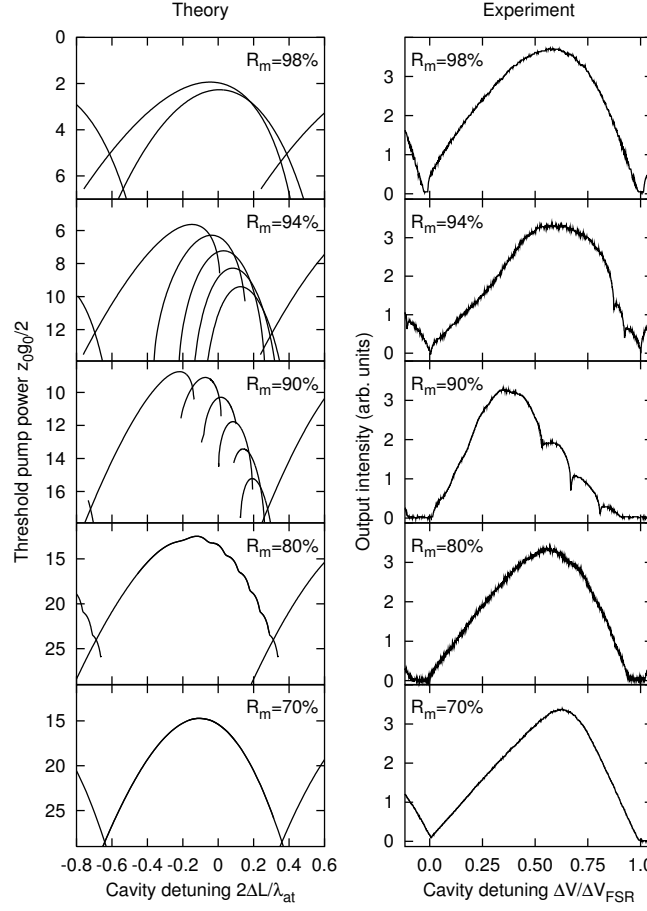


**Figure 7.5:** On the left is a theoretical calculation of the threshold of the modes against the cavity detuning for various reflectivities of the outcoupling mirror. On the right are experimental results which show the laser intensity output against the cavity detuning. The cavity detuning is measured in terms of the voltage  $\Delta V$  on the piezo, normalised to the voltage required to scan a full free spectral range  $\Delta V_{\text{FSR}}$ . When in the calculation the laser jumps from one mode to the next, the experiment should show a small discontinuity as well.

function of detuning. Large negative cavity-length detunings lead only to modes changes to the modal profiles, while changes are much more profound for small and positive detuning. Here, we resort to a slightly different procedure for comparing theory and experiment, guided by the above observations. We assume that the most negative cavity detuning within the free spectral range in the theory and experiment match. Then we match the most positive cavity detuning within the free spectral range in the experiment to the largest detuning in the calculations where the same high-order mode profile occurs as in the experiment (using the 94 % and 90 % reflectivity data). This leaves us with approximately 85(5) % of the original free spectral range in the theory to match with the entire free spectral range in the

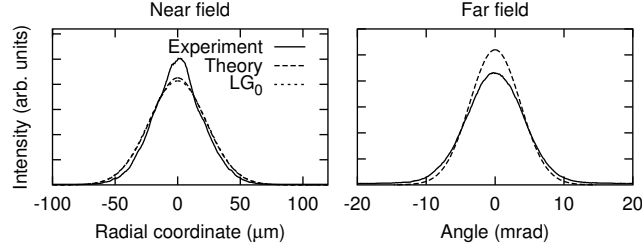


**Figure 7.6:** Near-field (left) and far-field (right) mode profile at reflectivity  $R_m = 98\%$ , for the cavity detuning corresponding to the lowest threshold. The solid curves are the experimental data, the dashed curves the result of the theoretical model. The index guide dominates (cf. Fig. 7.3), and the profile deviates very little from the profile of the lowest-order Laguerre-Gaussian mode  $LG_0$  of the purely parabolic index guide (both in the near field and in the far field). The  $LG_0$  mode is shown as the dotted curve in the near field; in the far field the  $LG_0$  profile is not shown, it would overlap with the curve of the theoretical model.

experiment. We note that this scaling is the only arbitrary scaling factor we have applied to our data. All other theoretical parameters are directly taken from the experiment, and have not been adjusted to further improve agreement between theory and experiment. Note also that a single set of values for the theoretical parameters was used to produce the full set of mode profiles discussed below.

For mirror reflectivity  $R_m = 98\%$ , we observe only one mode in the experiment. The modal profile changes very little as a function of detuning, both in the near field and in the far field. The theoretical and experimental profiles at the point of lowest threshold (highest output power) are compared in Fig. 7.6. The theory matches the experimental curve reasonably well, both in the near and far fields. For comparison the theoretical profile of the lowest-order Laguerre-Gaussian mode  $LG_0$  of the purely quadratic index guide ( $\Delta n_R$ ) is also shown. Clearly, the deviations from pure index guiding are rather small.

In Fig. 7.7, the three experimental mode profiles observed at  $R_m = 94\%$  are compared to theory. The three lowest order Laguerre-Gaussian mode ( $LG_N$ ,  $N = 0, 1, 2$ ) of the pure parabolic index guide are also shown. Especially for the higher order modes, there is a clear difference between  $LG_N$  on one hand, where the minima go to zero, and our theory and experiment on the other, where the minima are nonzero. Note also that in the near field the additional rings are generally weaker than their  $LG$  counterparts, while in the far field the rings are generally stronger. These profiles can be interpreted as standard Laguerre-Gaussian profile deformed under the influence of the gain guide.

For 90 % reflectivity, we have four modes with four different profiles, all shown in Fig. 7.8. Here, the deviations from the conventional  $LG$  modes are obvious, as the direct comparison in Fig. 7.8 shows. The near-field patterns show only very weak rings, while in the far field the outer ring becomes quite strong, even stronger than the inner rings. In addition the outer ring starts to merge with the inner rings. The theoretical mode profiles reproduce these features, and match the experimental profiles quite well. The only significant difference is that the theoretical profiles seem to be more deeply modulated.

Based on the near-field profiles in Fig. 7.7 and Fig. 7.8, a qualitatively explanation can

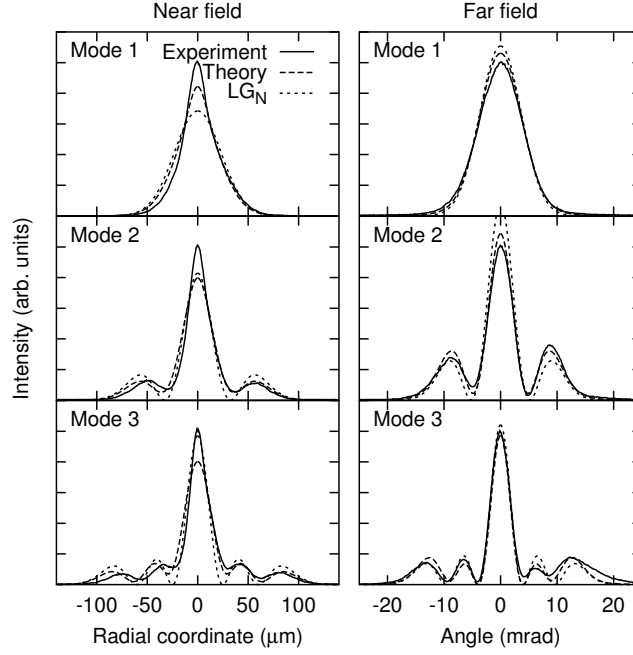


**Figure 7.7:** Near-field (left) and far-field (right) mode profiles at reflectivity  $R_m = 94\%$ . Three modes are found in the experiment (solid curves). These profiles match the results from the theoretical model (dashed curves) relatively well. In contrast, both deviate from the three lowest-order Laguerre-Gaussian TEM modes of the parabolic index guide ( $LG_N$ , dotted curves); the near-field rings are weaker and the far-field rings are stronger than those of the  $LG_N$  modes, and the intensity between rings does not go to zero.

now be given why each of these modes appears at a narrow range of detunings, a fact that was already noted in section 7.5.1, see Fig. 7.5. The near-field modal profiles are essentially strongly deformed Laguerre-Gaussians. Each mode has the lowest threshold when the overlap with the pump beam is maximised, i.e. when the rings are suppressed and when the central peak has a width similar to that of the gain profile, about one third of the  $LG_0$  mode in Fig. 7.8. To deform the central peak in this way, the lowest-order mode, a deformed  $LG_0$  mode, needs significant additional guiding. This additional guiding is provided by the gain-related index guide for positive detuning in frequency, i.e. for negative cavity-length detuning.

The next mode, a deformed  $LG_1$  mode, require less additional guiding, since the central peak of the  $LG_1$  mode has a reduced width to begin with. The width of the central peak of the third mode, a deformed  $LG_2$  mode, is similar to that of the gain profile, hence it does not need additional focussing, and it appears near zero detuning [50]. The central peak of the  $LG_3$  and higher-order modes actually need additional *anti-guiding* for maximum overlap with the gain profile. Thus, the related deformed modes will have the lowest threshold at negative frequency detuning (positive cavity-length detuning) where the gain-related index guide provides anti-guiding. In summary, each deformed mode has a specific detuning where the gain-related index guide yields maximum overlap with the gain profile. This effect is

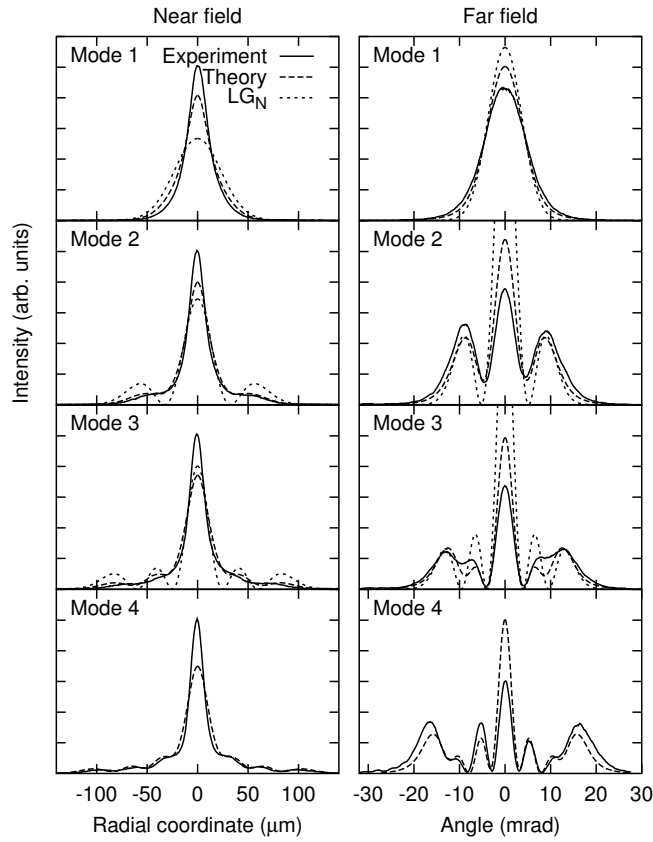


**Figure 7.8:** Near-field (left) and far-field (right) mode profiles at reflectivity  $R_m = 90\%$ . Four modes are found in the experiment (solid curves), and the profiles agree well with the results from the theoretical model (dashed curves), both in the near field and in the far field. For the higher-order modes the deviations from Laguerre-Gaussian modes are large: the near-field rings are strongly suppressed while the far-field rings become quite strong compared to the central peak. A direct comparison with the  $LG_N$  modes (dotted curves) is shown for the first three modes.

somewhat similar to “mode pulling” in a lossy cavity, the shift of the *longitudinal* modes towards line centre by the dispersion of the gain-related refractive index [1]. Hence it could be called “transverse mode pulling”.

At 80 % reflectivity, we enter the gain-dominated regime, and only a single mode is observed (Fig. 7.9). In contrast to the above, however, the modal profile now does change shape, and it does so in a continuous fashion while detuning the cavity. The evolution of the near field is not very interesting as it always shows a ringless profile, changing only in width when detuning the cavity length. Note however, that since the profile is not Gaussian, the word ‘width’ is actually ill-defined. Taking the standard deviation of such a profile as the width, we find that it decreases by about a factor of two when detuning from short to long cavity lengths over the available free spectral range. Although a longer cavity length causes



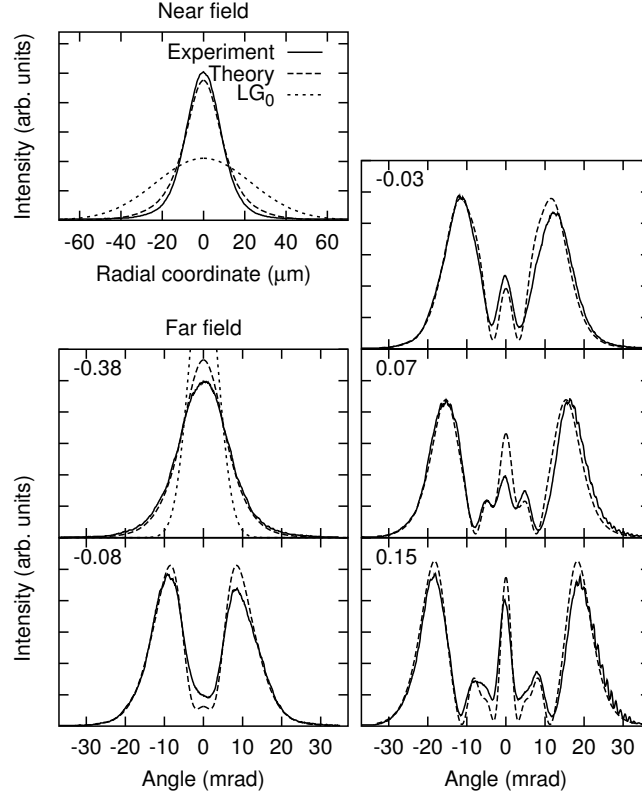


**Figure 7.9:** Near-field and far-field profiles for  $R_m = 80\%$  mirror reflectivity. The experimental data (solid curves) are again reproduced well by the theoretical model (dashed curves). The near-field profile changes only in width and we show only one profile. The far-field profile changes much more drastically; a number of representative examples are shown. The value of the cavity detuning  $2\Delta L/\lambda_{at}$  (cf. Fig. 7.5) of the theoretical curves is indicated in the graphs of the far-field profiles. The lowest-order Laguerre-Gaussian mode  $LG_0$  of the purely parabolic index guide is also shown for comparison (dotted curves).

less focussing or even defocussing for the gain-related index guide, the mode also requires more on-axis gain to remain at threshold, causing the field to be pulled towards the centre. Apparently, at longer cavity lengths the imaginary part of the gain guide has more influence on the mode formation than the gain-related index guide, causing a more narrow near field profile at longer cavity lengths.

The far field profile changes much more dramatically than the near field. The continuously changing profile is illustrated by a number of representative examples in Fig. 7.9. The theoretical value for the cavity detuning  $2\Delta L/\lambda_{at}$  is shown in the upper left corner of each graph (i.e. these numbers correspond to the horizontal axis in the left part of Fig. 7.5). For negative cavity-length detunings the mode profile changes only slowly, while for positive cavity-length detunings the change is much more rapid.

Finally, at a mirror reflectivity of 70 %, the gain guide is even more dominant (see also

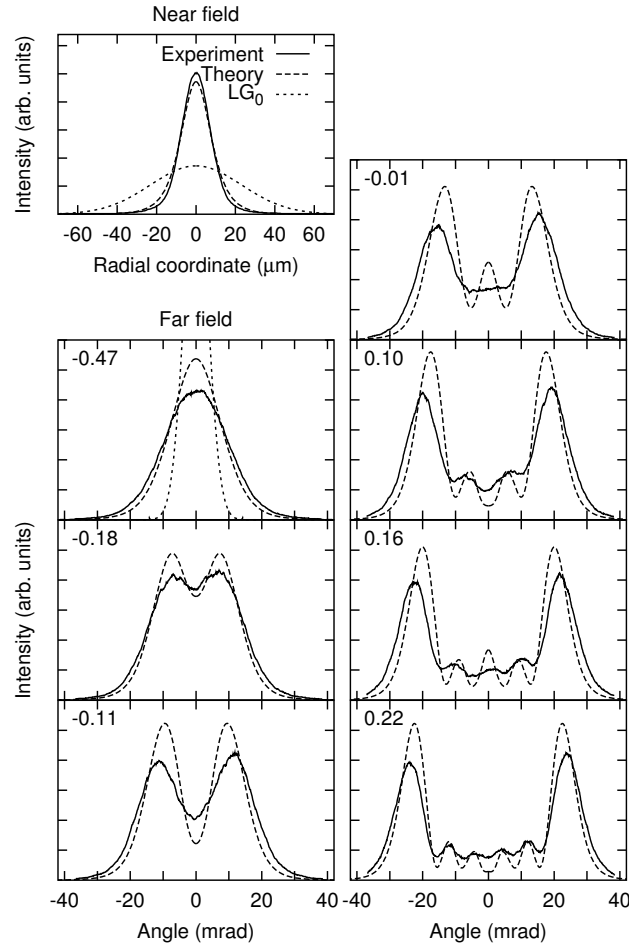


**Figure 7.10:** Near-field and far-field profiles for mirror reflectivity  $R_m = 70\%$ . The gain guide dominates (cf. Fig. 7.3) and is stronger than for  $R_m = 80\%$ ; its behaviour shown in Fig. 7.9 becomes even more pronounced. The near-field profile changes only in width as the cavity detuning is changed, and only one example is shown. Representative examples of the far-field modal profiles illustrate how the maximum intensity moves off-axis as the cavity detuning is changed. The value of the cavity detuning ( $2\Delta L/\lambda_{at}$ , cf. Fig. 7.5), is indicated for each far-field profile.

Fig. 7.3(b)). Again a single mode with a continuously changing profile as a function of detuning is observed. The shape in the near field seems to be fairly constant, it remains a more or less ringless profile (see Fig. 7.10) when the cavity is detuned. Again only the width of the profile changes.

The profiles in the far field, also shown in Fig. 7.10, are diverse. When detuning, we see the maximum intensity move outward continuously, while new maxima and minima form in the centre. This is an example of a laser showing conical emission [53]. This gives us profiles

that change from ringless to having three rings. Note that the outer ring is the strongest and the minima in the profile never go to zero. Also interesting is that the highest-gain profile in the far field has its maximum away from the centre. Once again the agreement between theory and experiment is quite satisfying, considering the complexity of the observed behaviour.

## 7.6 Discussion

The agreement between the theoretical model and the experiments, as compared in section 7.5, is surprisingly good. The large variety in observed modal profiles matches well with the model which has essentially no adjustable parameters. The only serious discrepancy is in the range of accessible cavity detunings, which we have pragmatically removed by a single scaling factor.

For decreasing mirror reflectivity, the modal profiles show a transition from the usual Laguerre-Gaussian profiles for parabolic index guiding to profiles that are typical for gain guiding. For the lowest reflectivities our observations are very similar to the predictions for a system with only gain(-related) guiding as described by Longhi and Laporta [53]: in particular we find that the cavity detuning plays a major role, and that conical emission appears for negative detuning in frequency. The similarities are striking, even though the actual transverse gain profile considered by Longhi and Laporta (a  $\text{sech}^2$  function) is different from our (Gaussian) gain profile. In fact, the present work seems to be the first experimental demonstration of the kind of conical emission predicted by Longhi and Laporta. Apparently this behaviour is a generic feature of gain guiding once the dispersive effect of the gain medium upon detuning from gain maximum (the gain-related index guide) is taken into account. As was already noted [53], conical emission occurs when the gain-related index guide actually yields anti-guiding (i.e., is equivalent to a negative lens, for negative detuning in frequency).

We now discuss the approximations made in the theoretical model, and their relevance for the observed differences with the experimental data. The most important approximation that was made in the theoretical model is describing the cavity as a longitudinally uniform waveguide, i.e., we have assumed that the gain medium, the gain and the mirror curvature are spread throughout the cavity. For this to be a reasonable approximation, the transverse profile of the field inside the cavity must not change significantly during one round trip. To satisfy this, the Rayleigh range of the field inside the cavity should be larger than the cavity length. However, since the transverse modal profiles are not really (Laguerre-)Gaussian, the Rayleigh range is not well-defined. Instead, it seems appropriate to use the waist size of the gain,  $w_g = 14 \mu\text{m}$  as the smallest near-field feature size expected (see also the curves for  $R_m = 70 \%$  in Fig. 7.3). This yields a lower boundary of about 0.98 mm for the Rayleigh range, while the optical length of the cavity is  $n_0 L = 0.51 \text{ mm}$ . Thus we expect the approximation to be reasonable but not perfect, and the observed size of the deviations (of order 10 %) seems reasonable. We expect this to be the main cause of the observed deviations.

As further evidence for this conjecture, we mention here that we have done similar experiments for the same configuration (e.g., also with  $w_g/w_0 \approx 0.3$ ) but with a more tightly curved mirror,  $R_c = 25 \text{ mm}$ . In that case, the Rayleigh range was about three times shorter, and the agreement between experiment and theory was significantly worse, in particular in terms of the number of observed modes.

An related theoretical approximation is that the cavity was folded out to make a wave-

guide, neglecting saturation. In the experiment, saturation can deform the transverse gain profile to be non-Gaussian through transverse spatial hole-burning, for example. To avoid the effects of saturation as much as possible, the experiments were performed close to threshold (with a pump parameter of less than 1.3), and the saturation effects on the transverse mode profiles are thus expected to be relatively weak. However, performing the experiments close to threshold means large intensity fluctuations as described in chapter 4. These fluctuations have been neglected in our theory, even though they could cause complicated forms of mode competition when combined with the saturation. There is some indication in chapter 8 that this actually happens at mode switches.

We have also neglected all thermally-induced guiding effects. It is possible that the heat deposited by the pump light causes an extra guide, but it will probably be weak compared to the two strong guiding mechanisms that we have included in the calculation. For instance, in a previous experiment [42], where the thermal guiding alone has been examined for a configuration similar to ours, the purely thermally guided mode would have a waist size of about  $200\ \mu\text{m}$ . Since our mirror curvature alone gives much stronger guiding, (the purely index-guided mode waist is  $46\ \mu\text{m}$ ), we can assume that the thermally induced guiding effects are indeed negligible.

A last effect that might cause the gain profile to be deformed, probably resulting in less deeply radially-modulated profiles, is the diffusion of excited states of the  $\text{Nd}^{3+}$  ions [54, 55]. The typical diffusion length of an excited state (less than  $0.5\ \mu\text{m}$ ), is about 4 % of the waist size of the gain, and neglecting diffusion seems justified.

We now briefly discuss the impact of these results on common microchip lasers. The latter typically have a planar monolithic design (while we have used an external concave mirror) and are operated far above threshold (while we have considered operation close to threshold). For a planar cavity the well-defined parabolic index guide of the concave mirror will be absent, and the index guide will be determined by thermal effects (thermal lensing and thermal curvature of the surface). Although the index guide will in principle have a non-parabolic shape, in practice approximating it as a parabolic index guide is often adequate [42] (as already noted in 7.1). Thus our description should provide a good approximation.

A more quantitative comparison between microchip lasers and our experimental laser can be based on the rescaled Eq. (7.7), which contains important dimensionless parameters such as the ratio  $w_g/w_0$  of the pump beam size and the size of the eigenmode of the index profile, and the dimensionless gain per Rayleigh range  $z_0 g_0$  (as well as the scaled frequency detuning  $\Delta\omega/\gamma_{\text{at}}$ ). The presented results are therefore directly applicable to microchip lasers, with their larger “index-guided” waist  $w_0$ , if the size of the pump spot is increased and if the mirror losses are reduced as compared to the values given in this chapter; this is indeed the case in practical microchip lasers.

To describe a laser far above threshold requires a more significant extension of the present results. Far above threshold the effects of saturation of the gain medium need to be included in the theoretical description. The amount of saturation will depend on the local intensity [51, 52, 56]. As a result, the gain profile will depend in the intensity profile of the lasing mode and on how far above threshold the laser is operated. The gain profile will deviate from the pump profile, and will generally become non-Gaussian. These complications are beyond the scope of this chapter. The results presented here do provide a good starting point for further work in that direction. We expect that the essential features noted here (e.g., the role of the mirror reflectivity in determining the relative strength of the gain guide and index guide) will remain valid far above threshold.

## 7.7 Summary and Conclusions

In this chapter we have studied theoretically and experimentally the transverse-mode formation caused by combined Gaussian gain guiding and parabolic index guiding in a microchip laser. We have used a  $\text{Nd}^{3+}:\text{YVO}_4$  crystal and a separate curved mirror to form a plano-concave configuration pumped by a narrow-width Gaussian beam, resulting in the emission of an interestingly wide variety of transverse profiles.

We have shown that at higher reflectivities ( $R_m \geq 90\%$  in our case), where we are still in the index-guide-dominated regime, higher-order modes appear with Laguerre-Gaussian-like profiles. The lowest-loss mode never has any rings, while the higher order modes each have one ring more than the mode before, i.e., the laser profile is characteristic for the mode number. Also, with a decrease in reflectivity, we see an increase in the number of visible modes. This is a consequence of the gain-related index guide, via what we have called “transverse mode pulling”. The deformation of the Laguerre-Gaussian profiles and the effects of the gain guide become stronger as well.

When lowering the reflectivity, there is a relatively sudden transition to the regime dominated by the gain-guide (in our case, for 80 % and 70 % reflectivity), where we see only one mode. The near-field profile is ringless, and only changes in width when the cavity is detuned. In contrast, the far field profile changes continuously. As the cavity length is increased, the maximum intensity moves outward, i.e., conical emission is observed, and rings appear inside. The more the cavity is detuned, the farther the high-intensity rings are from the centre. This situation is typical for gain guiding, where a single “trapped filament” is supported having a smooth amplitude profile and a rapidly varying phase profile. This near-field phase structure leads to ring structures in the far field that strongly depend on detuning.

Theory and experiment show profiles with a similar number of rings with similar strength. Also, the appearance of higher-order modes at high reflectivities and their disappearance at low reflectivities is reproduced by the theory. The deviations between theory and experiment are typically on the 10 %-20 % level. We expect that the approximation of the longitudinally uniform waveguide is the main source of these deviations. Going beyond this approximation would require a two-dimensional (radial and longitudinal) calculation, and hence a considerable additional computational effort. This is beyond the scope of this chapter.

In conclusion, we have experimentally studied transverse mode formation where several (anti-)guiding effects are present, and have used a relatively simple model for this intrinsically complicated process. Considering the simplifications made as discussed in section 7.6, we find excellent agreement between theory and experiment.



## Chapter 8

# Excess noise due to combined gain and index guiding<sup>1</sup>

*The combination of gain and index guiding can lead to non-orthogonal transverse modes and resonant excess noise. In experiments using an end-pumped Nd<sup>3+</sup>:YVO<sub>4</sub> microchip laser, we observe excess noise factors as large as 100 when tuning the cavity length towards mode crossings. An associated increase in relaxation oscillation damping demonstrates that we are indeed dealing with excess noise and not with dynamic instabilities. The laser displays strong self-pulsing due to mode hops at the mode crossings.*

## 8.1 Introduction

Excess quantum noise is the enhancement of ordinary quantum noise caused by the non-orthogonality of the cavity eigenmodes. Although all lasers have modes that are non-orthogonal to some degree, the effect is usually small unless guiding due to spatially non-uniform loss or gain is strong. Transverse excess noise theory was first developed by Peterman in 1979 [46] to explain noise effects in semiconductor lasers. Another 15 years would pass before the Petermann K (excess noise) factor was clearly demonstrated by the group of Siegman [57, 47]. Since then, most excess noise experiments have been performed with hard-edged unstable cavities, even though lasers with soft edges and smooth gain profiles can also exhibit large excess noise factors.

In this chapter we will present experiments aimed to investigate the prediction of Van Druten et al. [45] that large excess noise factors can arise in stable cavities with tightly focussed Gaussian gain, especially when gain and index guiding become comparable in strength. In their theoretical treatment, the authors make the assumption that the cavity axial loss can be tuned continuously, which would be equivalent to a continuous change in the mirror reflectivity in an experimental implementation. Since this approach is highly impractical for microchip lasers, we have instead chosen to change the modal gain by tuning the cavity length. We will show that this creates modes that display strong resonances in the noise behaviour. For cavity lengths where the modal gains become equal (so-called mode crossings) excess noise factors as high as 100 are observed.

The effect of gain and index guiding on the intensity profiles of the eigenmodes was studied extensively in chapter 7. Here we showed that the strength of the gain guide is dependent on the relative width of the pump profile  $w_g$  as compared to the width  $w_0$  of the purely index-guided mode. It also depends on the reflectivity of the mirror (see Fig. 8.1), with the high reflectivity mirrors displaying less gain-guiding.

<sup>1</sup>Y. Lien, E. van der Togt, N. J. van Druten, M. J. P. van Exter and J. P. Woerdman, "Excess noise due to combined gain and index guiding", to be published.

The reader should note that our experimental laser will be operated at non-zero detuning in this chapter. Since this allows for variations in the spontaneous emission factor, we have decided to use (and extend) the framework developed in the appendix of chapter 4. In addition to allowing for a variations in the spontaneous emission factor, this framework also differentiates between the different decay channels from the upper lasing level. The total upper-level decay is therefore  $(\gamma_1 + \gamma'_1) = 1.3(1) \times 10^4 \text{ s}^{-1}$ , where  $\gamma_1 \approx 0.61(5) \times 10^4 \text{ s}^{-1}$  is the spontaneous emission rate for ions that return to the lower lasing level and  $\gamma'_1$  is the decay rate to all other levels. Definitions for the damping rates  $\gamma'_n$ ,  $\gamma'_{NL}$  and  $\gamma'_N$  and the new oscillation rate  $\omega_{ro}$  are to be found in this chapter as well as in the appendix 4.11.

## 8.2 Experimental configuration

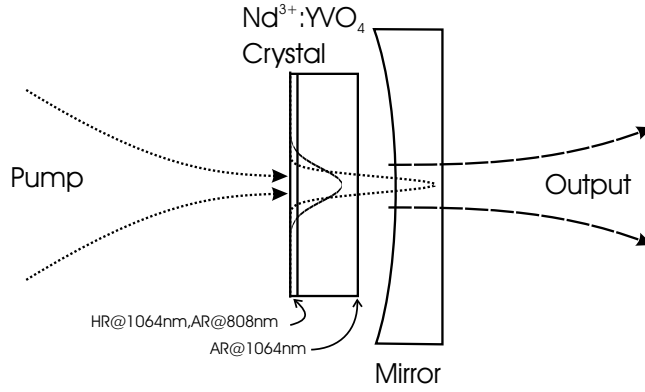


**Figure 8.1:** Laser cavity configuration. The Gaussian pump beam (dotted) is tightly focussed using a 80 mm lens. This figure shows a relatively wide Gaussian output beam (dashed), indicating a dominant index guide. The pumping region is narrow as compared to the output. This is indicated by the two intensity cross-sections (here drawn as Gaussian distributions). Crystal coatings are as indicated in the diagram.

The setup is very similar to that of the previous chapter, save the noise eater, which has been reinserted as shown in Fig. 5.1. The diagram showing the cavity configuration (Fig. 8.1) hence applies both for this chapter and the previous chapter. The pump beam is focussed onto the 0.23(3) mm thick  $\text{Nd}^{3+}:\text{YVO}_4$  crystal using a lens with a focal length of 80 mm (not shown). On one side, the crystal coating is highly reflective ( $\approx 100\%$ ) at 1064 nm and anti-reflective at 809 nm. On the opposite side it is anti-reflective at 1064 nm. A convex mirror, this time with a curvature of 200 mm, faces the anti-reflective (at 1064 nm) crystal facet. The minimum size of the air gap between crystal and mirror was  $\approx 50 \mu\text{m}$ . The crystal has a refractive index of  $n_e = 2.165$  for light polarised along the extraordinary axis. From this, we estimated that the optical cavity length is  $l_{opt} \approx 550 \mu\text{m}$ . The atomic doping level was 1 % of  $\text{Nd}^{3+}$ .

When compared to the theoretical model outlined in the previous chapter (Eqs. 7.14a)-(7.14c), we find an effective cavity length of  $L = 0.29 \text{ mm}$  and an effective base refractive index of  $n_0 = 1.87$ . Assuming that the effect of the pump-related gain guide is small as



compared to the index guide of the mirror, we find from Eq. 7.14c that the theoretical width of the (purely index-guided) mode is (approximately) equal to  $43 \mu\text{m}$ , which is similar to the value mentioned in chapter 7 for a comparable cavity.

All measurements were conducted using a mirror with a reflectivity  $R_m$  of 85 %. As gain guiding is quite strong, the eigenmodes differ significantly from the Laguerre-Gaussian modes of a cavity with quadratic index guiding<sup>2</sup>. The observed modes look very similar in the near field as they are confined by the pump profile. However, in the far field, only the fundamental mode has a Gaussian shape whereas higher-order modes take on the characteristic ringed profiles described in chapter 7.

We know from chapter 7 that various transverse (and longitudinal) modes can be brought to lase by tuning the cavity length. The output power depends on which mode is lasing in combination with the detuning of the mode from gain maximum. Fig. 8.2 shows the detuning dependency of the output power. For these experiments, a relatively slow detector

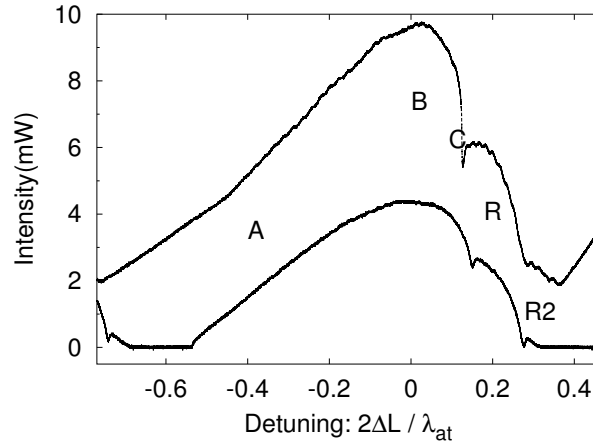


**Figure 8.2:** Average output intensity as a function of cavity detuning. Detuning is normalised according to the laser free spectral range; the length at which maximum output is observed is here set to zero. The top curve is measured at  $M = 5.0$ ; the bottom curve at  $M = 3.0$ . Here,  $\Delta L$  is the cavity length change and  $\lambda_{at}$  is the spontaneous emission wavelength. The pump parameter  $M$  is defined with respect to the point of maximum gain.

with a bandwidth of only 10 kHz – 100 kHz was used<sup>3</sup>). This detector could not follow the relatively fast relaxation oscillations as these have frequencies higher than 0.5 MHz. The pump parameters  $M = P_{in}/P_{thr}$  for the two curves in the figure are normalised to the threshold pump power at optimum detuning.

The average intensity measurements in Fig. 8.2 show several large “bumps”, where each bump represents a separate lasing mode. While the main bump, which includes labels A, B and C, represents the fundamental mode, the two shoulders to the right are two higher

<sup>2</sup>The guide is known as a quadratic index guide since the radially dependent refractive index is defined by  $n(r) = n_0 - ar^2$ , where  $a > 0$  is a constant and  $n_0$  is the base refractive index introduced in chapter 7.

<sup>3</sup>As in the previous chapters, we have used a *Centronic* OSD-15 photo-diode that was connected to a current amplifier with a variable load resistance  $R_L$ . This load resistance was set to a value between 10 k $\Omega$  and 10 M $\Omega$ , which would lead to the 10 kHz – 100 kHz maximum response.

order-modes (ring modes R and R2). For our later measurements in this chapter, we will concentrate on the main bump because of the large range of detuning available. Some measurements of the first ring mode R will, however, be included for the purpose of comparison.

As we saw in chapter 7, it is difficult to predict the actual shape of the structure as a function of detuning. Also, a comparison is complicated by the fact that we have no analytical model for the transverse modes and our interpretation is, as a consequence, based on numerical calculations.

However, it is instructive to compare the frequency detuning, in the form of the free spectral range  $\nu_{FSR} = 274$  GHz (for an optical cavity length of  $550 \mu\text{m}$ ) with the spectral bandwidth of the medium  $\gamma_{at} = 215 \text{ GHz}/\pi$ . This comparison shows that the gain is expected to drop to 40 % of the zero-detuning gain when we detune by half a free spectral range (i.e. by  $\Delta L = \lambda_{at}/4$ , where  $\Delta L$  is the detuning and  $\lambda_{at}$  is the wavelength of the spontaneous emission), which is more or less consistent with the observation that the laser turns off for detunings larger than half the free spectral range for  $M = 3$  in Fig. 8.2, but remains lasing for  $M = 5$ .

### 8.3 Laser modes and wave guiding

In our laser, the Gaussian pump-profile gives rise to an equivalent gain guide, while the mirror curvature leads to a quadratic index guide. The eigenmodes of cavities with such combined guiding are well-understood and their eigenfunctions can be predicted with good accuracy (see chapter 7). The relative strength of these two guiding effects is mainly set by the mirror reflectivity, as this determines the (modal) gain necessary to reach threshold.

When the reflectivity is high ( $> 98$  % for this cavity), the eigenmodes are primarily index guided and the eigenmodes hardly differ from Laguerre-Gaussian modes, which have the same shape in both the far- and near-fields. In all cavities with mirrors of reflectivity  $\gtrsim 90$  %, the laser output switches from one mode to another when the cavity length is changed. The transverse shape of each mode, however, is practically independent of detuning.

Once the reflectivity of the cavity mirrors is reduced, gain guiding becomes more important. For low reflectivity mirrors ( $< 80$  %), the laser only lases in one transverse mode, and there are no (transverse) mode switches. This mode, however, has a transverse profile that changes continuously with cavity detuning. As we saw in chapter 7, the transverse profile of such a mode hardly changes in the near field. In contrast, the far-field profile may change from a (near-) Gaussian to ringed mode with almost no intensity in the centre.

To obtain large K-factors we have studied the intensity noise at an intermediate reflectivity. Unlike chapter 7, where we used several mirrors of various reflectivity, we now used one mirror only with  $R_m = 85$  %. Typical cross-sections of the cavity eigenmodes are shown in Fig. 8.3. The measurements presented here are more noisy than the mode profiles of chapter 7 due to the lower quality of the imaging system used to obtain these profiles. In addition to using a different camera, additional noise was due to interference effects in the extra intensity filters. These were necessary because the measurements were conducted three times above threshold ( $M \approx 3$ ) compared to just above threshold in chapter 7.

Note how the fundamental mode has a nearly Gaussian profile in both the near- and far-fields. The first ring mode, however, has a large outer ring in the far field. The central peak is still relatively strong. For higher-order modes, the rings generally become more prominent (and numerous). The exact structure and width of each mode also varies to some extent

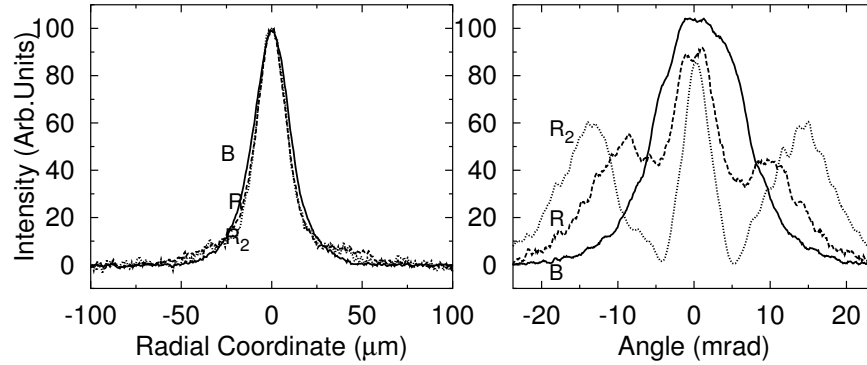


**Figure 8.3:** The eigenmodes of the cavity. On the left, we have plotted the near-field profiles of the three first eigenmodes. *B* is at gain maximum ( $2\Delta L/\lambda_{at} = 0$ ), *R* is the lowest order ring mode ( $2\Delta L/\lambda_{at} = 0.22(4)$ ), and *R<sub>2</sub>* is the next ring mode ( $2\Delta L/\lambda_{at} = 0.35(7)$ ). The far-field profiles have been plotted to the right. Measuring at the same detuning values, the mode at optimal detuning, the lowest-order ring mode, and the next ring mode are again labelled *B*, *R* and *R<sub>2</sub>*, respectively. This measurement was conducted at  $M \approx 3$ .

depending on the detuning. We will not discuss the change in structure here, but the change in width will be treated below.

The pump spot was measured to have a width  $w_g = 17(2) \mu\text{m}$  (cf. Eq. 7.6) in the near field (in the crystal). The widths of the cavity eigenmodes depend on the detuning from gain maximum due to guiding effects of the narrowly focussed gain. This can be seen in Fig. 8.4, where the width of the lowest loss mode has been plotted versus the detuning. As a reference, we also determined the width of the index-guided  $\text{TEM}_{00}$  mode using a mirror with 98 % reflectivity. Placing the cavity as close as possible to the mirror, this width was measured to be  $w = 37(2) \mu\text{m}$ , which is a little smaller than the theoretical  $w_0 = 43 \mu\text{m}$  width expected from Eq. 7.14c. This is consistent with our observation in Fig. 7.6, where the near-field mode profile also shows some narrowing due to the focussed gain. We also note that there was no significant difference between the widths in the vertical and the horizontal directions.

Using the cavity with the 85 % mirror, several cavity eigenmodes were observed to lase. However, the transverse width of the modes changes considerably with cavity length. In Fig. 8.4 the width of the fundamental mode has been plotted as a function of detuning. The width was determined by applying a *Gaussian* fit to the near-field profile, even though the shape is not exactly a Gaussian (see chapter 7). At maximum output, the overall  $22(2) \mu\text{m}$  width of the mode's near-field profile is quite a lot narrower than the  $43 \mu\text{m}$  of the purely index-guided mode mentioned above. This is due to a sizable amount of gain guiding, which is needed to provide for non-orthogonal modes. Fig. 8.4 also shows that the near-field profile narrows towards shorter cavities and widens towards longer cavities. This can be understood by considering the effect of detuning on the gain-related index guide in Eq. 7.6. Having in mind that a negative  $\Delta\lambda$  implies a positive  $\Delta\omega$ , we find that tuning towards negative  $\Delta\lambda$  creates a refractive index profile,  $\Delta n_g(r, \Delta\omega)$  that is the largest in the centre of the pump spot, hereby focussing the eigenmodes further.

The change in mode profile upon detuning also affects the dynamics of the relaxation oscillations. More specifically, the relaxation oscillation rate  $\omega_{ro}$  is expected to increase when

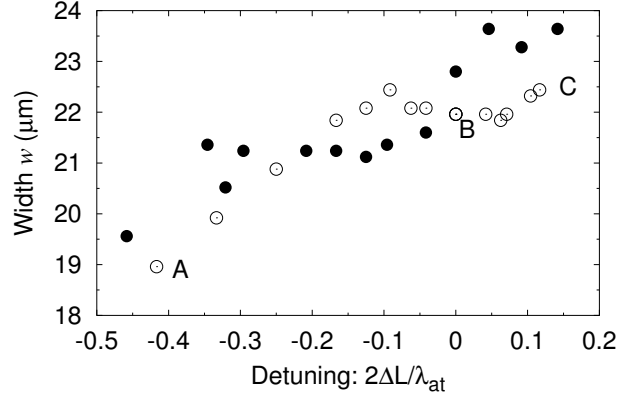


**Figure 8.4:** Laser beam waist as a function of detuning. The cavity length change ( $\Delta L$ ) has been normalised to the free spectral range of the laser ( $\Delta L_{FSR} = \lambda_{at}/2$ ). The width of the mode was found by fitting a Gaussian curve to the near-field profile. The open and filled circles denote two different data sets.

the mode profile tightens due to enhanced atom-field coupling. A plot of the relaxation os-

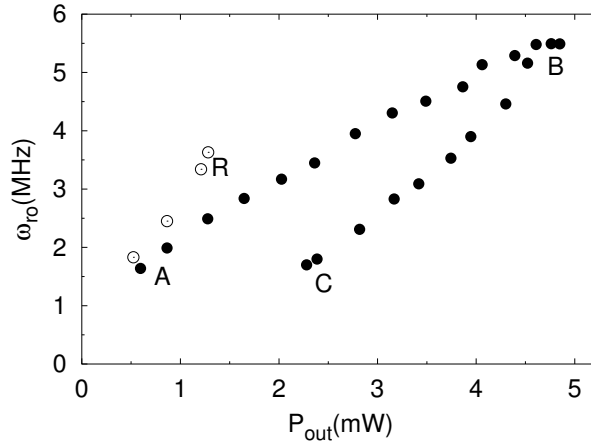


**Figure 8.5:** The relaxation oscillation frequency as a function of output intensity. The detunings A, B and C are the same as those in Fig. 8.2. R denotes the lowest order ring mode.

cillation rate  $\omega_{ro}$  is presented in Fig. 8.5. These results were obtained using a relatively fast InGaAs DC-detector (20 MHz bandwidth) in combination with a 2712 Tektronix spectrum analyser to measure the frequency of the main harmonic. We note that there are large differences in relaxation oscillation rate for the same output intensity  $P_{out} = h\nu\Gamma_c n_0$ , with  $\omega_{ro}$  being consistently larger at the same output intensity in the A segment than in the C segment

In order to interpret these differences, we restate Eq. 4.33 as

$$\omega_{ro} = \sqrt{\gamma_1 \Gamma_c n_0 \beta''}, \quad (8.1)$$

where the inversion and cavity decay rates ( $\gamma_1$  and  $\Gamma_c$ , respectively) are constant, and  $\beta''$  is a newly defined spontaneous emission factor that accounts for detuning and mode focussing. Thus, at the same output intensity, the difference in relaxation oscillation rate can only be explained by a modified spontaneous emission factor. An estimate for this change can be obtained by applying Eq. 8.1 to the points A and C in Fig. 8.5. At the same relaxation oscillation frequency  $\omega_{ro} \equiv 1.75$  MHz, we find that  $\beta''_A/\beta''_C = (n_C/n_A) = 3.5(4)$ .

Although the above argument sounds plausible, we have some reason to believe that this analysis may be too simplistic. From an experimental point of view, we could equally well have argued that the spontaneous emission factor should be proportional to the gain at a specific detuning, as the underlying spontaneous and stimulated emission rates are naturally linked. Based on Fig. 8.2, we would then find that  $\beta''$  is the largest at the point B and up to a factor 2 lower in both A and C. This is clearly a contradiction with the previous prediction. A likely explanation for this discrepancy has been given by Cheng et al. [58], who argue that the relaxation oscillation dynamics can be very complicated in cavities with non-uniform gain distributions. Their model, which involves time-dependent changes to both the shape and intensity of the lasing mode, suggests that oscillation rates  $\omega_{ro}$  can differ significantly from the value given by Eq. 8.1. Because of this uncertainty, we believe that the measured gain gives a much better estimate of  $\beta''$ .

In the appendix of chapter 4 we have introduced a modified spontaneous emission factor  $\beta'(\Delta\omega)$  that also applies for cavities that are spectrally detuned from gain maximum. However, in cavities with narrowly focussed gain, we also need to consider the effect of the mode's spatial overlap with the gain. This lead to significant changes in the spontaneous emission factor as the spatial overlap not only changes from mode to mode, but also depends on the detuning within this mode as described in relation to Fig. 8.4. It is therefore convenient to introduce a new spontaneous emission factor  $\beta''$  that takes both these effects into consideration:

$$\beta''(w, \Delta\omega) \approx \frac{\beta}{1 + (\Delta\omega/\gamma_{at})^2} \left[ \frac{w(0)}{w(\Delta\omega)} \right]^2, \quad (8.2)$$

where  $\beta$  is the reference spontaneous emission factor for the case of zero detuning and therefore optimal spectral overlap of the mode with the gain. The parameter  $w(\Delta\omega)$  refers to the waist of the laser's eigenmode at a specific frequency detuning  $\Delta\omega$ ; the tighter the waist, the larger the  $\beta''$ .

The effects of spatial and spectral overlap are of similar size and they both have to be considered. Based on Fig. 8.4, we estimate the effect of spatial overlap, i.e. the effect of the beam waist, to contribute an additional factor  $\approx 1.5$  to  $\beta''$  at the position A as compared to C of Fig. 8.4. The spectral overlap depends on the offset of the laser from the gain profile and has the same sign for both the A and the C segment. Since we do not know the position of zero detuning, we will not estimate what the effect will be on  $\beta''$  at A and C. We do, however, note again that a detuning of half a spectral range from gain maximum is equivalent to a decrease in  $\beta''$  by a factor 2.25. From chapter 7, we also know that the point C is close to the point of zero spectral detuning. Hence, when comparing the branches A and C, it is reasonable to expect the two contributions to the changing  $\beta''$  to approximately cancel out for similar output powers. Hence, we find more evidence that comparable output powers indicate similar spontaneous emission factors.

## 8.4 Self pulsing at mode crossings

Laser oscillation switches from one mode to another at mode crossings. Since the modal gain of the two modes is very similar at these two points, instabilities can easily arise. In our laser, we found that the laser would usually start emitting a periodic sequence of very intense pulses at this point. The peak intensity of these pulses is commonly more than ten times the height of the relaxation oscillations. Immediately after this pulse, the laser switches off for a short period and a particular cycle of relaxation oscillations is performed, before another pulse will be emitted again.

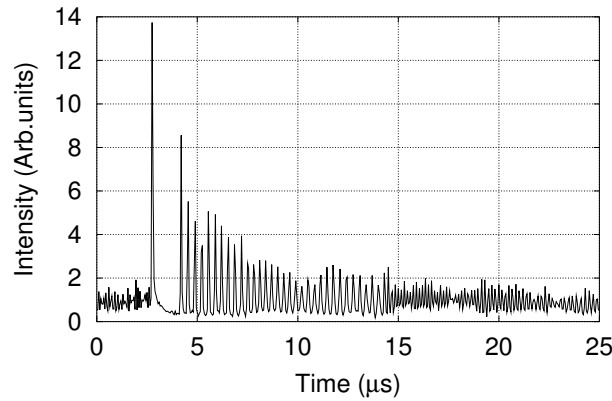


**Figure 8.6:** Typical pulsing behaviour, in which one can distinguish three regimes. The “switching cycle” starts with a very strong pulse that is followed by a time interval where the laser practically switches off. After this transient, slow relaxation oscillations give way to fast relaxation oscillations in the third regime. Please note that the measured intensity of the first strong pulse is limited by the speed of the detector.

A typical example of pulsing is presented in Fig. 8.6. The initial, strong pulse, which is seen on the left, was too fast and too strong to be measured by the 20 MHz (InGaAs) photodiode used here. Therefore, we made additional measurements using a 6 GHz AC-coupled detector (*NewFocus* 1514 fiber-coupled photo-receiver with a bandwidth of 2 MHz – 6 GHz). This revealed that each pulse has a duration of 9(2) ns with little fluctuations. The peak height was measured to be roughly 30 times the average intensity of ordinary relaxation oscillations which, in the case of the deep oscillations in Fig. 8.6, is equivalent to about 10 times the height of the oscillation peaks that directly follow.

The initial pulse of Fig. 8.6 is followed by a very low output region, in which we think that the laser has actually switched off. After approximately 1.5  $\mu$ s the laser starts operating again with a relaxation oscillation frequency of  $\approx 3.2$  MHz. After a short period it switches to a much higher oscillation frequency, 6.2 MHz. This whole scenario takes 10 – 100  $\mu$ s, where the large range in period is caused by variables such as the pump power [59]. For a certain pump and cavity configuration, however, the period was found to be quite stable and would only fluctuate by 5 – 10 %.

Although pulsing was observed at all mode crossings, we note that no pulsing behaviour was observed for  $M \lesssim 2$ . Also, the pulsing region widens for larger pump values, resulting in relatively wide pulsating detuning regions at each mode crossing.

Fig. 8.7 demonstrates that the observed intensity pulsing is related to a mode switch. This figure depicts simultaneous time traces of the total output of the experimental laser (bottom dashed curve) and the output of the fundamental mode (top solid curve) as selected with a stationary Fabry-Perot cavity. Similar Fabry-Perot traces of the first ring mode (not shown) exhibit no pulses, only regular relaxation oscillations. From this we conclude that the laser emits in the fundamental mode *both* during the initial strong pulsing and during the slow relaxation oscillations. After these events, the laser will switch back from the fundamental

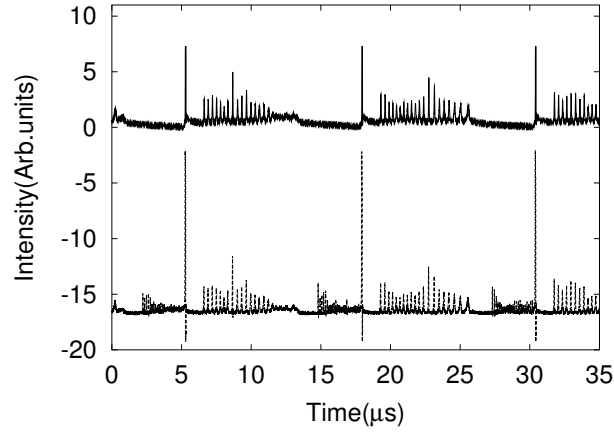


**Figure 8.7:** *Experimental demonstration of the link between pulses and mode hops. The bottom curve shows a time trace of the total intensity of the laser. The solid top curve shows a simultaneous measurement of the intensity of one of the modes only, as measured behind a stationary Fabry-Perot cavity that acts as a spectral filter and mode selector. The peak height of the strongest pulse is (again) limited by detector speed. It is also the slowness of the detector that leads to the pulse overshooting in the bottom curve. The vertical axis has an arbitrary scaling.*

mode to the lowest order ring mode. This switch occurs without pulse although the laser may sometimes stop lasing again for a short period. The laser emits in the ring mode before another pulse is emitted when switching back to the fundamental mode. Note that this figure shows somewhat different behaviour from Fig. 8.6. While the latter figure shows a direct switch from the fundamental mode to the first ring mode, Fig. 8.7 indicates that there is a short period between oscillations where the laser oscillates only weakly or switches off.

Mode hopping also explains the changes in relaxation oscillation period observed in Figs. 8.6 and 8.7. The period change corresponds roughly to jumps between C and R in Fig. 8.5 and is probably due to a difference in the spontaneous emission factor  $\beta''$  between the two modes (as discussed in section 8.3).

Pulsing behaviour similar to this has been observed by Otsuka et al. in three-mode  $\text{Nd}^{3+}:\text{YVO}_4$  lasers [60]. Using the Fabry-Perot cavity, we found no evidence of a third mode except when pumping the experimental laser far above threshold ( $M \gtrsim 10$ ). Nevertheless, we can not exclude that a third mode is involved in the mode switching process. Such a mode should then, however, be very weak or present only shortly as it was not observed. We would also like to comment that the near-degeneracy of the modes may be another cause for

pulsing as it might facilitate coupling of the modes.

Another possibility is that the pulses are related to self-focussing caused by the Kerr effect [61, 62, 59], or that they are caused by local transverse gain buildup. In either case, we believe that the sudden releases of energy are caused by slight (inter-mode) differences in the modal widths (see [59] and chapter 7). In addition, since pulses can be interpreted as extremely strong relaxation oscillations [63], relaxation-oscillations could be a plausible trigger for the pulses.

We also used the planar Fabry Perot in a further experiment, where we measured the frequency splitting between the fundamental mode and the first ring mode. This was done in order to observe frequency degeneracy as predicted by theory [45]. By tuning the laser towards mode crossings, we expected to observe a decrease of the frequency difference between the two adjacent lasing modes when tuning towards mode crossings. This was not observed.

## 8.5 Excess quantum noise

Excess quantum noise enhances the spontaneous emission into the lasing mode. It manifests itself as an additional multiplicative factor  $K$  in the laser rate equations. Referring back to the appendix of chapter 4, we see that the photon damping is changed to:

$$\gamma'_n = K \frac{\Gamma_c}{n_0}, \quad (8.3)$$

where a large factor  $K$  leads to enhanced photonic damping as there is more spontaneous emission in the lasing mode. Non-linear damping should remain as derived in chapter 4, but its value would depend on the changing  $\beta''$  as discussed on page 83. This damping can be restated as

$$\gamma'_{NL} = \frac{\Gamma_c \gamma_1 \beta'' n_0}{\gamma_2}, \quad (8.4)$$

which is expected to change much less than photonic damping  $\gamma'_n$ .

Since the lower-level decay rate is much smaller than the cavity decay rate, the inversion decay,  $\gamma'_N$ , is neglected. The total damping rate is now  $2\gamma_{ro} \approx \gamma'_n + \gamma'_{NL}$ , and the intensity fluctuations are given by

$$g_2(0) - 1 = Q_2 \approx [1 + (\gamma'_{NL}/\gamma'_n)]^{-1} = \left[1 + \frac{\beta''}{K} \frac{\gamma_1}{\gamma_2} n_0^2\right]^{-1}, \quad (8.5)$$

where the prefactor  $1/K$  contains the effect of the excess noise, whereas  $\beta''$  still exhibits a mild dependence on detuning and modal width.

In previous chapters, we measured  $g_2(0)$  as a function of the pump parameter  $M$ . However, because of the ambiguous definition of the latter parameter (it changes with detuning), it is more convenient to measure  $g_2(0)$  in terms of output power ( $P_{out} = \Gamma_c h\nu n_0$ ). This was done by pumping the laser with constant pump power, while the laser was detuned to move from point A to C via B in Fig. 8.2. Thus on the A and C segments we obtained a set of points for which  $g_2(0)$  could be compared for the same output power. Although such a noise-comparison is relatively straight-forward, one must be aware that in addition to  $K$ , also the gain (or equivalently  $\beta''$ ) changes when detuning the cavity (see Eq.8.5).

The noise in the two segments A and C has been compared in Fig. 8.8 for a pump of  $M = 3$  ( $M = 1$  was defined as the threshold of the laser at optimal detuning, i.e., point B).



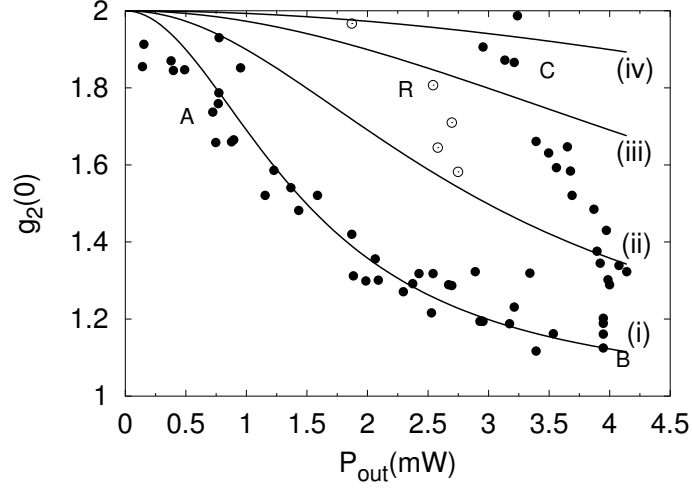


**Figure 8.8:** The second order correlation function  $g_2(0)$  versus output power  $P_{out}$  for a pump power  $M = 3$ . The points A,B and C denote the same the regimes as outlined in the discussion of Fig. 8.2. The curves correspond to different  $K$  factors: (i)  $K = 1$ ; (ii)  $K = 4$ ; (iii)  $K = 16$ ; (iv)  $K = 64$ . The open circles corresponds to the first ring mode.

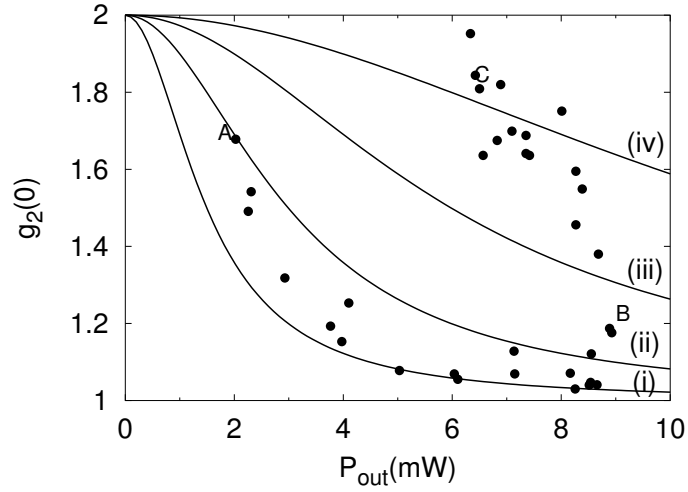


**Figure 8.9:** The second-order correlation function  $g_2(0)$  plotted as a function of output power  $P_{out}$ . This measurement was conducted for a pump power  $M = 5$ . The points A,B and C are equivalent to those in Figs. 8.8 and 8.2. Every theoretical curve corresponds to a different  $K$  factor: (i)  $K = 1$ ; (ii)  $K = 4$ ; (iii)  $K = 16$ ; (iv)  $K = 64$ . No measurement for the ring mode has been conducted at this pump power.

As is clear from the graph, the C segment lies much higher than the A segment, suggesting larger  $K$  factors for this segment. The curves (i), (ii), (iii) and (iv) are defined by  $g_2(0) - 1 =$

$[1 + (a/K)P_{out}^2]^{-1}$ , which is a rewrite of Eq. 8.5.

Curve i is a fit of this function to the A segment. This fit yields  $a = (\beta''\gamma_1/\gamma_2) \times (h\nu\Gamma_c)^{-2} = 0.45 \text{ mW}^{-2}$ . Taking reasonable estimates of  $\Gamma_c = -c/2l_{opt} \ln R = 4.4 \times 10^{10} \text{ s}^{-1}$ ,  $\gamma_1 = 0.61(5) \times 10^4 \text{ s}^{-1}$ ,  $\gamma_2 = 1.6(1) \times 10^9 \text{ s}^{-1}$  and  $K = 1$ , yields  $\beta'' \approx 3 \times 10^{-6}$ , which is in excellent agreement with previous observations for the spontaneous emission factor in a similar cavity with zero detuning  $\Delta\omega$  [5], at least when considering the difference between the upper level decay rates (see section 4.11). The curves (ii), (iii) and (iv) are similar to curve (i), but the values for  $K$  are 4, 16 and 64, respectively. The position of some of the points on the C segment indicates that  $K$  factors may come close to 100. Note that also the ring mode, marked with R in Fig. 8.8 seems to experience excess noise.

For comparison, we have also included equivalent measurements at a higher pump power,  $M = 5$ . The result of this was very similar to the above measurement. However, in this case even larger excess noise factors are observed. The curves (i), (ii), (iii) and (iv) are the same as those plotted in Fig. 8.9 with  $a = 0.45 \text{ mW}^{-2}$ .

At this point the reader should note that we have not (yet) considered how changes in the spontaneous emission factor affect the curves (i) to (iv) in Fig. 8.8. Although we have good reason to believe that the effects of spatial and spectral overlap may approximately cancel out in the two segments, we do expect to see some variations within the segments, with  $\beta''$  becoming smaller further away from the point B. However, this is expected to deliver only small changes to the noise as compared to the change in the excess noise factor  $K$ . Hence, noise enhancements that are attributable to changes in  $\beta''$  are only observed in the very detuned part of the A segment for  $M = 5$  (see Fig. 8.9). Assuming that the two segments have the same  $\beta''$  for the same output power, we find excess noise factors that approximate 100.

Based on measurements of  $g_2(0)$  only, we cannot be sure that the increase in intensity fluctuations is due to an increase in (spontaneous emission) noise and not due to decreases in damping. The latter suggestion is plausible because of the proximity of a mode crossing, where this non-linear system might become dynamically unstable. To distinguish between these theories we note that this competing theory predicts a *reduced* damping, whereas one distinctive feature of excess noise is the fact that the noise increase is accompanied by *increased* damping of the relaxation oscillations. This is seen the easiest from Eq. 8.3, where photon damping increases with  $K$ , and Eq. 8.5 where noise actually increases with increased photon damping.

The role of damping is demonstrated in Fig. 8.10, where the RF-spectra are compared for the two different segments. Especially Figs. 8.10b and 8.10d are important as these were taken for the same output power ( $P_{out} = 6.7 \text{ mW}$ ). From these two (sub)figures we see that the relaxation oscillation damping  $\gamma_{ro}$  has increased from  $8.4(9) \times 10^5 \text{ s}^{-1}$  in (b) to  $3.3(3) \times 10^6 \text{ s}^{-1}$  in (d). This is almost a factor four increase in damping.

We note that also the relaxation oscillation damping rate can be affected by variations in  $\beta''$  through Eq. 8.4 since  $2\gamma_{ro} \approx \gamma'_n + \gamma'_{NL}$ . That the observed change in  $\gamma_{ro}$  is not due to a changing  $\beta''$  is illustrated by the fact that the relaxation oscillation rate only changes by a factor of 1.4, from  $5.27(5) \times 10^7 \text{ s}^{-1}$  to  $3.7(1) \times 10^7 \text{ s}^{-1}$ , which is considerably smaller than the change in relaxation oscillation damping. Furthermore, this quantity confirms that changing  $\beta''$  cannot explain the huge increase in noise seen for the two Figs. 8.8 and 8.9.

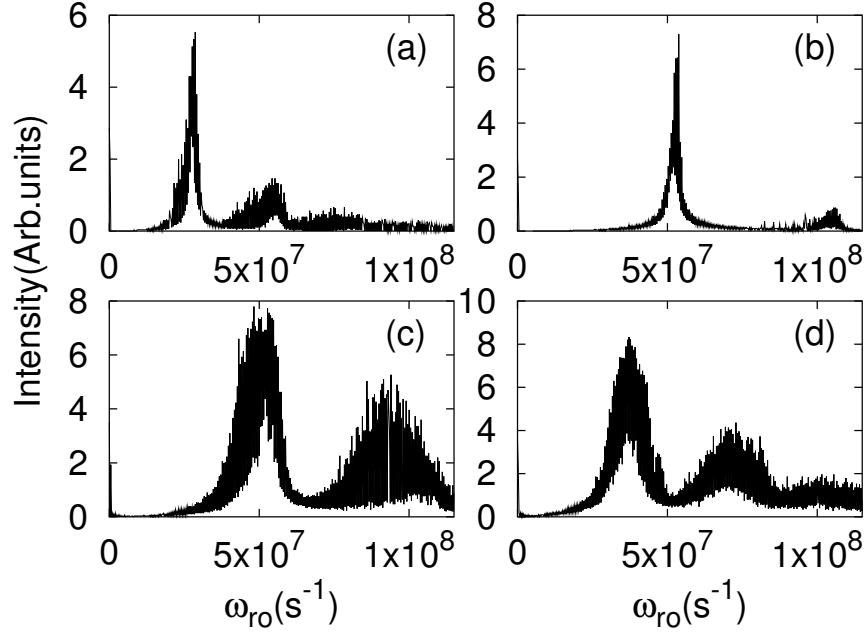


**Figure 8.10:** RF-spectra of the laser at  $M=5$ . The four figures are represented according to detuning, with (a) being the shortest cavity and (d) being the longest. The laser output power is (a)  $P_{out} = 2.9$  mW (A segment), (b)  $P_{out} = 6.7$  mW (A segment), (c)  $P_{out} = 8.3$  mW (C segment), (d)  $P_{out} = 6.7$  mW (C segment).

## 8.6 Concluding discussion

Observing the intensity dynamics of an experimental system with combined gain and index guiding showed that tuning the cavity towards mode crossings can induce mode switching as well as excess noise factors.

At mode crossings, we observed pulsing accompanied by switching between different eigenmodes of the laser cavity. We believe that this behaviour is related to self-focussing of the modes [59, 62] in the cavity. This effect probably combines with rapid changes in the mode pattern [59] made possible by gain degeneracy of the cavity eigenmodes.

However, outside the mode crossing region, we observed no evidence of dynamical instabilities. Instead, we measured enhanced noise levels that correspond to 100-fold enhancement of the fluctuations. Although also a modified spontaneous emission factor can induce enhanced noise, these changes would be negligible as compared to excess noise. Strong evidence for excess noise was given by the fact that relaxation oscillation damping *increased* with increased fluctuations. This indicates a photonic origin for the fluctuations (cf. Eq.4.11).

Our experimental system shows resonant behaviour as two modes become degenerate. This is similar to experiments with unstable hard-edged resonators [64]. However, unlike these experiments, we see no evidence of non-resonant excess noise, where many subthreshold (non-orthogonal) modes are involved.

In conclusion, we have demonstrated experimentally that large excess noise factors can

occur in lasers with a narrowly focussed Gaussian pump and weak index guiding. Observing both excess noise and modal instabilities, we differentiate between the two causes of fluctuations by measuring the relaxation oscillation damping rate, which increases for enhanced excess noise. At this stage, we have not yet made a thorough, quantitative comparison with theory [45], but we do plan to do so in the near future.

## Bibliography

---

- [1] A. E. Siegman, *Lasers* (University Science Books, Mill Valley, CA, 1986).
- [2] M. P. van Exter, G. Nienhuis, and J. P. Woerdman, "Two simple expressions for the spontaneous emission factor  $\beta$ ," *Phys. Rev. A* **54**, 3553–3558 (1996).
- [3] F. T. Arecchi, In *Instabilities and Chaos in Quantum optics*, F.T. Arecchi and R.G. Harrison, ed., Springer Series on Synergetics **34**, 9–48 (Springer, Berlin, 1987).
- [4] C. O. Weiss and R. Vilaseca, *Dynamics of Lasers* (VCH Verlagsgesellschaft mbH, Weinheim, 1991).
- [5] N. J. van Druten, Y. Lien, C. Serrat, M. P. van Exter, and J. P. Woerdman, "Laser with thresholdless intensity fluctuations," *Phys. Rev. A* **62**, 3808–3816 (2000).
- [6] J. P. Verdeyen, *Laser electronics* (Prentice-Hall, Englewood Cliffs, New Jersey, 1989).
- [7] P. P. Yaney and L. G. DeShazer, "Spectroscopic studies and analysis of the laser states of  $\text{Nd}^{3+}$  in  $\text{Nd}^{3+}:\text{YVO}_4$ ," *J.Opt.Soc.Am.* **66**, 1405–1414 (1976).
- [8] T. S. Lomheim and L. G. DeShazer, "Optical-absorption intensities of trivalent neodymium in the uniaxial crystal yttrium orthovanadate," *J. Appl. Phys* **49**, 5517–5522 (1978).
- [9] C. Bibeau, S. A. Payne, and Powell, "Direct measurement of the terminal laser level lifetime in neodymium-doped crystals and glasses," *J.Opt1995.Soc.Am. B* **12**, 1981–1992 (1995).
- [10] C. Becher and K.-J. Boller, "Low-intensity-noise operation of  $\text{Nd} : \text{YVO}_4$  microchip lasers by pump-noise suppression," *J. Opt. Soc. Am. B* **16**, 286–295 (1999).
- [11] M. Sargent III, M. O. Scully, and W. E. Lamb, Jr., *Laser Physics* (Addison-Wesley, Reading, 1974).
- [12] T. Ogawa, "Stochastic Toda-oscillator model of the bad-cavity laser," *Phys. Rev. A* **42**, 4210–4225 (1990).
- [13] P. Paoli, A. Politi, and F. T. Arecchi, "Statistical dynamics of class-B lasers," *Z. f. Phys.B* **71**, 403–410 (1988).
- [14] F. Auzel, "Multiphonon-assisted anti-Stokes and Stokes fluorescence of triply ionized rare-earth ions," *Phys. Rev. B* **13**, 2809–2817 (1975).
- [15] E. D. Reed and H. W. Moos, "Multiphonon relaxation of excited states of rare-earth ions in  $\text{YVO}_4$ ,  $\text{YAsO}_4$ , and  $\text{YPO}_4$ ," *Phys. Rev. B* **8**, 980–987 (1973).
- [16] L. A. Riseberg and H. W. Moos, "Multiphonon orbit-lattice relaxation of excited states of rare-earth ions in crystals," *Phys. Rev.* **174**, 429–438 (1968).
- [17] B. R. Judd, "Optical absorption intensities of rare-earth ions," *Phys. Rev.* **127**, 750–761 (1962).
- [18] G. S. Ofelt, "Intensities of crystal spectra of rare-earth ions," *J. Chem. Phys.* **37**, 511–520 (1962).
- [19] The Casix Crystal Guide 1999. CASIX, Inc., P.O. Box 1103, Fuzhou, Fujian 350014, China.
- [20] R. Loudon, *The Quantum Theory of Light* (Oxford University Press, Oxford, 1973), and references therein.

- [21] D. F. Walls and G. J. Milburn, *Quantum Optics* (Springer Verlag, Berlin, 1994).
- [22] M. Lax, "Quantum noise VII: The rate equations and amplitude noise in lasers," IEEE J. Quant. Electron. **QE-3**, 37–46 (1967).
- [23] D. E. McCumber, "Intensity fluctuations in the output of cw laser oscillators. I," Phys. Rev. **141**, 306–322 (1964).
- [24] P. R. Rice and H. J. Carmichael, "Photon statistics of a cavity-QED laser: A comment on the laser-phase-transition analogy," Phys. Rev. A **50**, 4318–4329 (1994).
- [25] D. R. B. Levien, M. J. Collett, "Quantum noise in two- and three-level models of the laser," Phys. Rev. A **47**, 5030–5036 (1993).
- [26] J. Arnaud, "Photon-number variance in laser diodes with quiet pumps," J. Opt. Soc. Am. B **14**, 2193–2195 (1997).
- [27] H. F. Hofmann and O. Hess, "Coexistence of thermal noise and squeezing in the intensity fluctuations of small laser diodes," J. Opt. Soc. Am. B **62**, 1926–1933 (2000).
- [28] M. O. Scully and W. E. Lamb, "Quantum theory of an optical maser. I. General theory," Phys. Rev. **159**, 208–226 (1967).
- [29] H. Haken, "A nonlinear theory of laser noise and coherence. I," Z. Phys. **181**, 96–124 (1964).
- [30] F. Arecchi, "Photocount distributions and field statistics," In *Quantum Optics*, R. Glauber, ed., pp. 57–110 (Academic Press, New York, 1969).
- [31] J. A. Armstrong and A. W. Smith, In *Progress in Optics*, E. Wolf, ed., **6**, 213 (North-Holland, Amsterdam, 1967).
- [32] H. F. Hofmann and O. Hess, "Thermal photon statistics in laser light above threshold," Phys. Rev. A **62**, 063807 (2000).
- [33] J. P. Zhang, D. Y. Chu, and S. L. Wu, "Photonic-Wire Laser," Phys. Rev. Lett. **75**, 2678–2681 (1995).
- [34] P. H. Cheng, T. D. Lee, J. S. Pan, Y. Lai, and K. Tai, "Spontaneous emission factor versus cavity volume in low dimensional photonic micro-cavities," Opt. Commun. **142**, 229 (1997).
- [35] U. Mohideen, W. S. Hobson, S. J. Pearton, F. Ren, and R. E. Slusher, "GaAs/AlGaAs microdisk lasers," Appl. Phys. Lett. **64**, 1911 (1994).
- [36] R. Loudon, 2000, private communications.
- [37] Y. Yamamoto and N. Imoto, "Internal and external field fluctuations of a laser oscillator: Part I - Quantum mechanical Langevin Treatment," IEEE J. Quant. Electron. **22**, 2032 (1986).
- [38] H. Risken, *The Fokker-Planck Equation* (Springer, Berlin, 1989), pages 45–59.
- [39] M. Toda, "Studies of a non-linear lattice," Phys. Rep. **18**, 1–123 (1975).
- [40] Y. Lien, S. M. de Vries, N. J. van Druten, M. P. van Exter, and J. P. Woerdman, "Photon statistics of a laser with slow inversion," Phys. Rev. Lett. **86**, 2786–2789 (2001).
- [41] R. Olshansky, P. Hill, V. Lanzisera, and W. Powazinik, "Universal relationship between resonant frequency and damping rate of 1.3  $\mu\text{m}$  InGaAsP semiconductor lasers," Appl. Phys. Lett. **50**, 653–655 (1987).
- [42] J. J. Zayhowski, "Thermal guiding in microchip lasers," In *Advanced Solid-State Lasers*, H. P. Jenssen and G. Dubé, eds., OSA Proceedings Series **6**, 9–13 (OSA, Washington DC, 1991).
- [43] A. J. Kemp, R. S. Conroy, G. J. Friel, and B. D. Sinclair, "Transverse mode formation in microlasers by combined gain- and index-guiding," IEEE J. Quant. Electron. **35**, 1314–1321 (1999).

- [44] T. Y. Fan, "Aperture guiding in quasi-three-level lasers," *Opt. Lett.* **19**, 554–556 (1994).
- [45] N. J. van Druten, M. P. van Exter, and J. P. Woerdman, "Resonant excess quantum noise in focused-gain lasers," *Opt. Lett.* **26**, 1176–1178 (2001).
- [46] K. Petermann, "Calculated spontaneous emission factor for double-heterostructure injection lasers with gain-induced waveguiding," *IEEE J. Quant. Electron.* **15**, 566–570 (1979).
- [47] Y.-J. Cheng, C. G. Fanning, and A. E. Siegman, "Experimental observation of a large excess quantum noise factor in the linewidth of a laser oscillator having nonorthogonal modes," *Phys. Rev. Lett.* **77**, 627–630 (1996).
- [48] A. E. Siegman, "Excess spontaneous emission in non-Hermitian optical systems. II. Laser oscillators," *Phys. Rev. A* **39**, 1264–1268 (1989).
- [49] M. P. van Exter, N. J. van Druten, A. M. van der Lee, S. M. Dutra, G. Nienhuis, and J. P. Woerdman, "Semi-classical dynamics of excess quantum noise," *Phys. Rev. A* **63**, 043801, 1–13 (2001).
- [50] C. Serrat, M. P. van Exter, N. J. van Druten, and J. P. Woerdman, "Transverse mode formation in microlasers by combined gain- and index-guiding," *IEEE J. Quant. Electron.* **35**, 1314–1321 (1999).
- [51] G. K. Harkness and W. J. Firth, "Transverse modes of microchip solid state lasers," *J. Mod. Opt.* **39**, 2023–2037 (1992).
- [52] S. Longhi, "Theory of transverse modes in end-pumped microchip lasers," *J. Opt. Soc. Am. B* **11**, 1098–1107 (1994).
- [53] S. Longhi and P. Laporta, "Longitudinal-transverse mode interplay and conical emission in microchip lasers," *J. Opt. Soc. Am. B* **12**, 1511–1515 (1995).
- [54] H. G. Danielmeyer, "Effects of drift and diffusion of excited states on spatial hole burning and laser oscillation," *J. Appl. Phys.* **42**, 3125–3132 (1971).
- [55] J. J. Zayhowski, "The effects of spatial hole burning and energy diffusion on the single-mode operation of standing-wave lasers," *IEEE J. Quant. Electron.* **26**, 2052–2057 (1990).
- [56] F. Sanchez and A. Chardon, "Pump size optimization in microchip lasers," *Opt. Commun.* **136**, 405–409 (1997).
- [57] Y.-J. Cheng, P. L. Mussche, and A. E. Siegman, "Measurement of laser quantum frequency fluctuations using a Pound-Drever stabilization system," *IEEE J. Quant. Electron.* **31**, 1498 (1994).
- [58] Y.-J. Cheng, P. L. Mussche, and A. E. Siegman, "Cavity decay rate and relaxation oscillation frequency in unconventional laser cavities," *IEEE J. Quant. Electron.* **31**, 391–398 (1995).
- [59] J. P. van der Ziel, J. L. Merz, and T. L. Paoli, "Study of intensity pulsations in proton-bombarded stripe-geometry double-heterostructure  $\text{Al}_x\text{Ga}_{1-x}\text{As}$  lasers," *J. Appl. Phys.* **50**, 4620–4637 (1979).
- [60] K. Otsuka, H. Utsu, R. Kawai, K. Ohki, Y. Asakawa, S.-L. Hwang, J.-Y. Ko, and J.-L. Chern, "Self-induced spiking oscillations and associated instabilities in a laser-diode-pumped three-mode Nd : YVO<sub>4</sub> laser," *Jap. J. Appl. Phys.* **38**, 1025–1028 (1999).
- [61] M. B. Willemsen, A. S. van de Nes, M. P. van Exter, and J. P. Woerdman, "Self-pulsations in vertical-cavity semiconductor lasers," *Appl. Phys. Lett.* **77**, 3514–3516 (2000).
- [62] R. Lang, "Intensity pulsation enhancement by self-focusing in semiconductor injection lasers," *Jap. J. Appl. Phys.* **19**, L93–L96 (1979).

- [63] C. R. Mirasso, G. H. M. van Tartwijk, E. Hernández-García, D. Lenstra, S. Lynch, P. Landais, P. Phelan, J. O’Gorman, M. S. Miguel, and W. Elsässer, “Self-pulsating semiconductor lasers: Theory and experiment,” *IEEE J. Quant. Electron.* **35**, 764–770 (1999).
- [64] M. A. van Eijkelenborg, A. M. Lindberg, M. S. Thijssen, and J. P. Woerdman, “Resonance of quantum noise in an unstable-cavity laser,” *Phys. Rev. Lett.* **77**, 4314–4317 (1996).



## Samenvatting

---

Deze samenvatting is een populair-wetenschappelijke uitleg van dit proefschrift en de achterliggende fysica. Het proefschrift behandelt meerdere aspecten van de quantumruis in een laser, met nadruk op de effecten van trage emissie en ruisoverdaad. Een uitleg van deze concepten volgt na een korte behandeling van de principes van de laser.

### De laser

Een van de meest centrale vragen van de laserfysica is wat het verschil is tussen het door de laser en door andere lichtbronnen (zoals gloeilampen) uitgezonden licht. Het antwoord ligt in het ontstaan van het licht: terwijl bij een lamp bijna enkel *spontane* emissie produceert, domineert *gestimuleerde* emissie het uitgezonden licht van een laser.

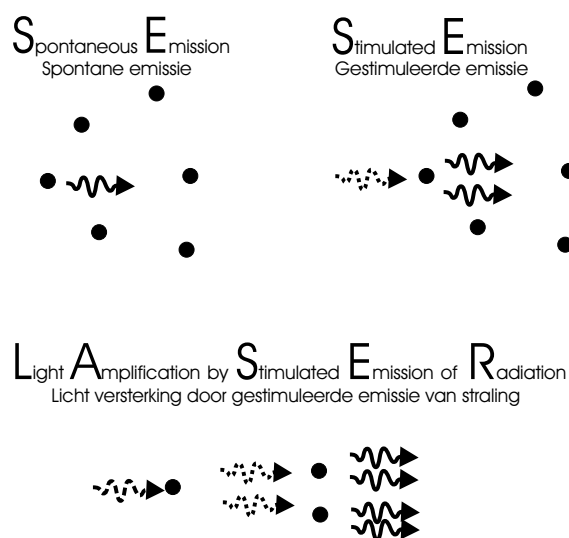
In het kort gezegd is spontane emissie het spontaan uitzenden van een foton (een licht-deeltje) door een aangeslagen atoom (zie linksboven Fig. 1). In dit geval vindt de emissie van een foton plaats zonder invloed van buitenaf. Wanneer dit precies gebeurt wordt helemaal door toeval bepaald, net zoals de uitkomst van een dobbelsteen. (Dit toevalsprincipe kan wel wat vreemd lijken. Zelfs Einstein had er enige bezwaren mee, vandaar zijn beroemde uitspraak “God does not play dice”).

Gestimuleerde emissie treedt op wanneer een foton een aangeslagen atoom passeert met het gevolg dat dit atoom nog een foton uitzendt. Dit tweede foton is volledig identiek aan het inkomende foton (een soort kloon dus) en neemt de zelfde ruimte in, heeft dezelfde richting én dezelfde golflengte als het oorspronkelijke foton. Deze twee fotonen kunnen zich nu weer vermenigvuldigen bij het passeren van andere aangeslagen atomen (zie onderaan Fig. 1). Op deze manier zouden dus oneindig veel identieke fotonen kunnen ontstaan, als tenminste er geen verliezen zouden zijn.

Het vermenigvuldigingsproces wordt tegengehouden door twee soorten verliezen. Eén is de absorptie van fotonen in het medium. De ander is het verlies ten gevolge van fotonen die uit de zijkanten van het versterkende medium gaan verdwijnen. Dit laatste is te verhelpen door spiegels neer te zetten zodat de fotonen terug het medium ingaan.

In het geval waar het ontstaan van identieke fotonen door gestimuleerde emissie groter dan de verliezen is, hebben wij het over lasers. Omdat zo goed als ieder foton in een laser identiek is, heeft dit licht zeer bijzondere eigenschappen die ideaal zijn in veel hightechnologische toepassingen.

Het is hier misschien verhelderend op te merken dat het bouwen van een laser uit een gewone gloeilamp niet mogelijk is, zelfs wanneer spiegels worden neergezet om de gestimuleerde emissie terug in het medium te kaatsen (het medium is in dit geval de gloeidraad). Dit komt doordat de absorptie van gestimuleerde emissie in het medium van de gloeilamp altijd (veel) groter zal blijven dan de creatie van identieke gestimuleerde fotonen. Het licht van een gloeilamp bestaat dus bijna uitsluitend uit spontane emissie.



**Figuur 1:** Linksboven: Een atoom in een aangeslagen toestand zendt licht uit zonder invloed van buitenaf (spontane emissie). Dit licht kan allerlei richtingen en golflengtes hebben. Rechtsboven: Een aangeslagen atoom zendt een foton uit dat identiek is aan het inkomende foton (gestimuleerde emissie). Onderaan: meer gestimuleerde emissie leidt tot meer identieke fotonen. De identieke fotonen worden in het medium gehouden door het neerzetten van spiegels.

## Quantumruis

Wanneer fotonen dezelfde golflengte en richting hebben, zoals in het geval van gestimuleerde emissie, wordt gezegd dat zij in dezelfde toestand zijn. Fotonen die ontstaan door spontane emissie hebben allerlei verschillende golflengtes en richtingen, en deze verkeren dus in verschillende toestanden. Sommige spontane emissie fotonen verkeren toevallig in dezelfde toestand als het gestimuleerde laserlicht in de laser.

Quantum ruis komt doordat het tijdstip van dit soort emissie helemaal door toeval bepaald wordt. Deze ruis leidt tot fluctuaties in het uitgezonden laserlicht. Er zijn twee verschillende types fluctuaties: fase- en intensiteitsfluctuaties. Fasefluctuaties zijn kortstondige veranderingen in de golflengte van de laser; intensiteitsfluctuaties treden op wanneer het aantal fotonen in de trilhaute niet stabiel is. Ik behandel hier alleen de intensiteitsfluctuaties.

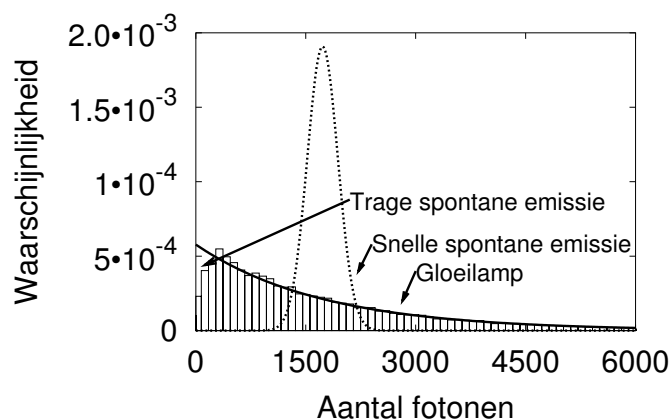
Doordat een lamp bijna uitsluitend spontane emissie uitzendt, zal het licht van een lamp heel veel intensiteitsfluctuaties bevatten. In laserlicht, waar bijna alle laserfotonen klonen van elkaar zijn, zit meestal heel weinig ruis, zowel wat betreft golflengte als intensiteit. Dat lamplicht veel meer ruist dan laserlicht is (in principe) met een snelle intensiteitsmeter te zien.

## Trage spontane emissie

We weten dat het tijdstip van spontane emissie door toeval bepaald wordt, maar dat betekent niet dat spontane emissie even vaak in alle soorten atomen optreedt. Men kan zich afvragen hoe dit kan als spontane emissie door toeval bepaald wordt. Het werpen van een dobbelsteen geeft hier een goed analogon. Als spontane emissie zou plaatsvinden bij de uitkomst 1 van het gooien van een dobbelsteen, zou je een zestigzijdige dobbelsteen gemiddeld 10 keer meer moeten gooien dan een zeszijdige dobbelsteen. Spontane emissie treedt dan niet zo vaak op en dit wordt dus trage spontane emissie genoemd.

In de laser van dit proefschrift is de spontane emissie heel traag. Dit heeft tot gevolg dat alles wat gebeurt in de laser, heel langzaam is. Een van de belangrijkste gevolgen van de trage dynamica is dat de damping van de intensiteitsfluctuaties ook veel trager wordt, waardoor deze fluctuaties veel groter worden. De laser, die zich kenmerkt door heel weinig fluctuaties, wordt op deze manier veel ruiziger dan normaal.

De sterkte van de fluctuaties van een laser met trage spontane emissie is niet uitsluitend afhankelijk van de traagheid van de emissie, maar ook van de grootte van de laser. Wij nemen waar dat hoe kleiner de laser is, des te meer fluctuaties er zijn. Dit komt doordat er gemiddeld precies één spontaan uitgezonden foton in de laser toestand voorkomt, terwijl het aantal gestimuleerde uitgezonden fotonen in het algemeen evenredig met de grootte van de trilhaute is.



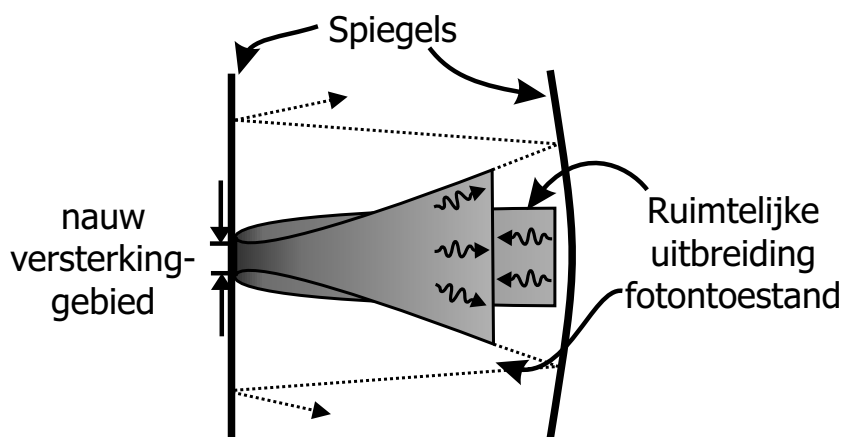
**Figuur 2:** Foton waarschijnlijkheidsverdeling. De verticale as toont de waarschijnlijkheid om een bepaald aantal fotonen, af te lezen op de horizontale as, aan te treffen op een willekeurig moment. De gestippelde curve is de intensiteitsverdeling van een laser met snelle spontane emissie, de doorgetrokken curve is die van een gloeilamp. Het histogram laat experimentele data voor een laser met trage emissie zien.

In dit proefschrift wordt onder andere aangetoond dat een laser met trage spontane emissie in veel opzichten van een gewone gloeilamp lijkt. In Fig. 2 heb ik een grafiek gemaakt van de waarschijnlijkheid van verschillende intensiteiten. Kleine fluctuaties zijn herkenbaar aan een smalle distributie, zoals in het geval van lasers met een snelle emissie. Als er meer fluctuaties zijn, is het verschil tussen het minimaal en het maximaal aantal te verwachten fotonen nog extremer, zodat de verdeling zeer breed is. Zowel de gloeilamp als een laser met trage emissie

hebben een zeer brede distributie, zoals in de grafiek te zien is.

## Ruisoverdaad

Tot nu toe hebben we het gebruikelijke geval van een laser besproken, waarbij er altijd één spontaan uitgezonden foton per toestand is. Er zijn niettemin gevallen waarin er meer dan één spontaan uitgezonden foton in de laser aanwezig is. Dit geval, dat *ruisoverdaad* wordt genoemd, vindt plaats wanneer het verlies of de versterking in de trilhaute ruimtelijk beperkt is.



**Figuur 3:** Trilhaute met een nauw versterkingsgebied. De pijltjes tonen de richting van de fotonen in de laserende toestand aan. Zoals te zien is, wordt dichtbij het beperkte versterkingsgebied de fotontoestand smaller, wat er verder weg toe leidt dat de fotontoestand divergeert (groveweg kan men zeggen dat het licht verandert van dat van een platte golffront naar dat van een divergerende puntbron). Bij opeenvolgende rondes neemt deze divergentie verder toe totdat je beperkt wordt door de eindige reflectie van de spiegel. De fotonen in de adjoint toestand zijn convergent en lopen tegen de fotonen in de hoofdtoestand.

In dit soort lasers wordt de ruis in de fotontoestand met het gestimuleerde licht, hier de laserende toestand genoemd, beïnvloedt door een zogenoemde “adjoint” toestand. Spontane emissie in de adjoint toestand is aanvankelijk convergent, maar na een paar rondes in de trilhaute eindigen deze adjoint fotonen eveneens in de divergente, laserende toestand. In de loop van dit proces wordt de spontane emissie versterkt, waardoor de quantum ruis veel groter kan worden.

In het experiment bekijken we trilhautes waar het licht slechts in een heel klein gebied versterkt wordt. Wij passen de breedte van de versterking zo aan dat wij een soort “ruisresonantie” vinden waar de adjoint fotonen tot honderd keer versterkt worden voordat zij in de laserende toestand komen. Hoe dit experiment werkt is verder te lezen in de laatste twee hoofdstukken van dit proefschrift.

## Sammendrag

---

Dette sammendraget er ment som en populærvitenskapelig beskrivelse av de emner som blir behandlet i denne doktorgradsavhandlinga. Hovedemnet i avhandlinga er kvantestøy i lasere. Jeg konsentrerer meg spesielt om treg spontan emisjon og eksess kvantestøy (=excess quantum noise), to fenomén som begge kan lede til store fluktuasjoner. Før jeg begynner med disse konseptene vil jeg først forklare de fundamentale prinsippene bak lasere.

### Hva er en laser?

De fleste har nok hørt om lasere og vet at de har enkelte egenskaper som skiller dem fra andre lyskilder som for eksempel ei vanlig lampe. Men hva er disse forskjellene, og hvordan oppstår de? Disse spørsmålene er nok best besvart ved å se på hvordan lyset blir til. Her skiller vi mellom *spontan emisjon*, som gir sitt opphav til vanlig lampelys, og *stimulert emisjon* som gir laserlys.

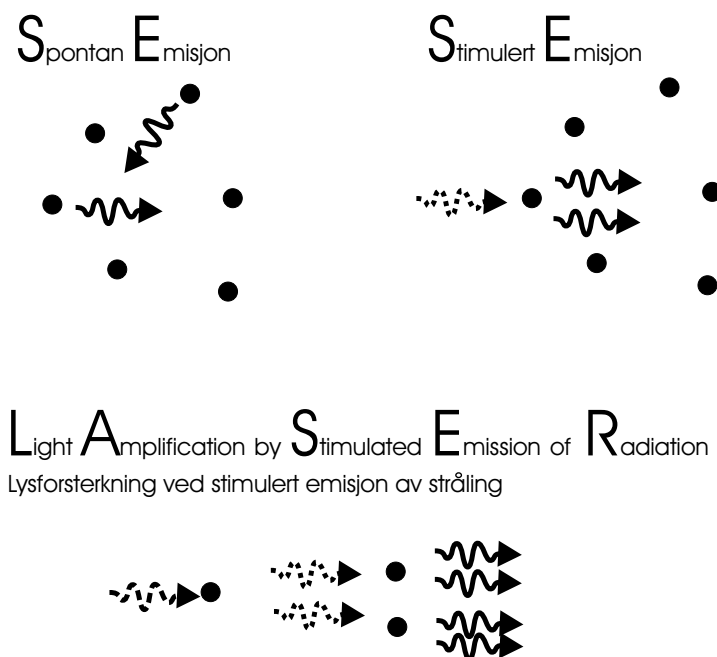
Spontan emisjon finner sted når et eksitert atom gir ifra seg et foton uten påvirkning utenfra. Tidspunktet for slik emisjon er kun gitt ved tilfeldighet, noe som igjen har gitt sitt opphav til Einsteins berømte utsagn “God does not play dice” (Gud spiller ikke med terninger). Selv om Einstein ikke likte dette tilfeldighetsprinsippet, mener de aller fleste av dagens vitenskapsmenn (og kvinner at det virkelig blir “kastet terning”). Fotoner fra spontan emisjon er alle forskjellige og kan ha alle slags retninger og forskjellige bølgelengder.

Stimulert emisjon finner sted når et foton passerer et eksitert atom med den følge at dette atomet gir ifra seg et foton før det går til den ikke-eksiterte tilstanden. Dette andre fotonet er helt identisk med det første fotonet og kan derfor betegnes som en slags klon. Der hvor de identiske fotonene kommer i kontakt med flere eksiterte atomer, kan en kjedereaksjon oppstå, der et stort antall identiske fotoner blir skapt.

Det er naturligvis en grense for hvor mange identiske fotoner som kan bli til. I en laser finnes det også fotontap. Denne begrensninga kan være at noen fotoner blir absorbert i det forsterkende mediumet, eller ved at fotoner forsvinner ut mediumets sider. Absorbasjonen er gitt av mediumet og dette tapet kan man ikke gjøre noe med. Tap ut sidene kan forhindres ved å bruke speil som reflekterer lyset tilbake inn i det forsterkende mediumet.

I en laser oppstår identiske fotoner fort nok til å gjøre opp for tapene. Her er så godt som alle fotoner identiske og dette lyset har derfor meget spesielle egenskaper som gjør det ideelt i mange “høyt teknologiske” anvendelser.

For å vike litt fra hovedtråden, vil jeg her bemerke at det ikke er mulig å bygge en laser fra ei vanlig lyspære, selv om man skulle bruke speil til å reflektere lyset tilbake inn i mediumet (som i dette tilfellet vil være glødetråden). Grunnen til dette er at absorbasjon i slike medium alltid vil forbli større enn forsterkningsevnen ved stimulert emisjon. Siden mediumet til lamper ikke er tilpasset for stimulert emisjon, kommer spontan emisjon alltid til å dominere.



**Figur 1:** Spontan emisjon finner sted på et vilkårlig tidspunkt uten påvirkning utenfra. Ved stimulert emisjon er det det innkommende fotonet som utløser emisjonen av et nytt foton. Hvis fotonetapet er lite, begynner en kjedereaksjon hvor flere identiske fotoner blir skapt.

## Kvantestøy

Når to fotoner har samme bølgelengde og retning, slik som ved stimulert emisjon, sier man at de er i samme fotontilstand. Dette betyr videre at spontant emitterte fotoner er å finne i mange forskjellige fotontilstander da disse kan ha forskjellig retning og bølgelengde. Fordi spontant emitterte fotoner har alle slags forskjellige tilstander, hender det også at fotoner fra spontan emisjon ender opp i fotontilstanden med stimulert emisjon.

Tidspunktet for slik emisjon er tilfeldig, og det er dette som gjør at spontan emisjon fører til fluktueringer i antallet fotoner inne i laseren. Vi kaller dette kvantestøy; og effekten kan måles i laserens avgitte lys.

Det må presiseres at kvantestøy som oftest har en veldig liten effekt i lasere, da nesten alt lys er skapt gjennom stimulert emisjon. I ei lampe derimot, er det en masse fluktueringer siden lamper nesten bare avgir spontan emisjon. Denne forskjellen kan man måle med en veldig snar detektor.

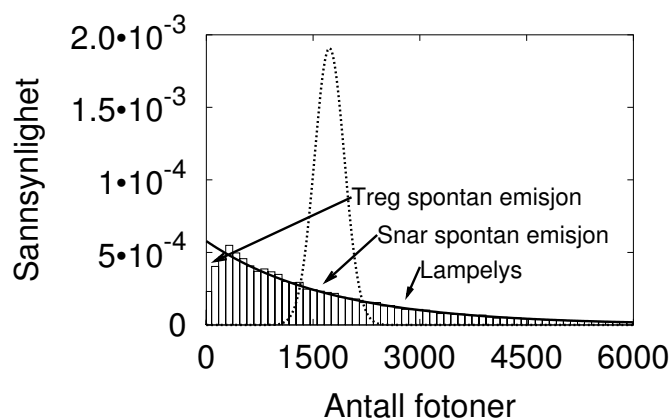
## Treg spontan emisjon

Selv om det spontane emisjonsforløpet er tilfeldighetsbetinget, betyr det ikke at den spontane emisjonen foregår like hyppig i alle typer atomer. For å gå tilbake til terningkast kan man si at en får tallet 1 (eller 2 eller 3) mye snarere med en sekssiders terning enn, la oss si, en

sektisiders terning. Når den spontane emisjonen er lite hyppig, sier vi at laseren har treg inversjon.

Laserene i denne avhandlinga har alle utrolig treg spontan emisjon. Dette har til følge at alt som skjer i denne laseren, foregår veldig langsomt. En av de største følgene av denne tregheten er at *dempingen av fluktueringene blir mye tregere*. Dette fører til at fluktueringene blir mye større enn i lasere med snar spontan emisjon.

Hvor mye fluktueringer det er i en laser er ikke bare avhengig av hvor treg inversjonen er, men det kommer også an på størrelsen til laseren. I denne avhandlinga viser jeg at jo mindre laseren er, desto mer fluktueringer. Grunnen til dette er at det (i gjennomsnitt) alltid er ett spontant emittert foton i alle lasere uavhengig av størrelsen, mens antallet stimulerte fotoner er proporsjonal med laserstørrelsen. Spontan emisjon har derfor større effekt i små lasere.



**Figur 2:** Forventet sannsynlighetsfordeling for antallet fotoner med sannsynligheten vist på den vertikale aksen. Antallet fotoner er på den horisontale aksen. Striplekurven viser fordelinga for en laser med snar emisjon og den gjennomtrukne kurven tilsvarer lys fra ei lampe. Histogrammet viser målingene for en laser med treg spontan emisjon.

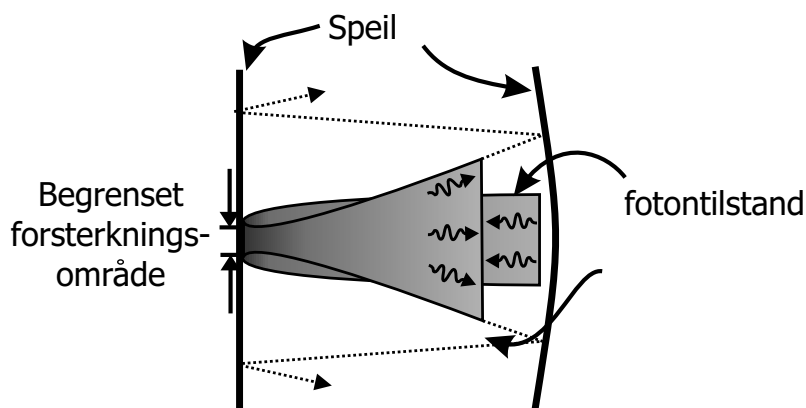
Jeg har videre vist at en liten laser med treg inversjon ligner på en vanlig lampe på mange måter. I figur 2 har jeg tegnet inn sannsynlighetsfordelingene for forskjellige typer lyskilder. Et system med små fluktueringer kan man gjenkjenne ved at fordelinga er helt smal som i tilfellet med lasere med snar emisjon. Ved større fluktuasjoner blir fordelinga veldig bred som vist for lasere med treg inversjon og for vanlige lamper.

## Eksess kvantestøy

Inntil nå har vi antatt at det alltid vil være gjennomsnittlig ett spontant emittert foton i hver tilstand. Selv om dette vanligvis er tilfelle, finnes det lasere hvor det er mange spontant emitterte fotoner. Dette, som vi kaller eksess kvantestøy, finner man i lasere som har en svært begrenset område med fotontap eller forsterking.

I en slik laser blir støyen i fotontilstanden med det stimulerte lyset, det jeg kaller hovedtilstanden, påvirket av en såkalt “adjoint” fotontilstand. Spontan emisjon i adjointtilstanden konvergerer og går til å begynne med imot lyset i hovedtilstanden. Likevel, etter noen runder

mellom speilene, ender fotonene i adjointtilstanden opp i den divergerende hovedtilstanden. Som en del av denne prosessen blir dette lyset forsterket, noe som kan lede til en uvanlig sterk kvantestøy. Herav betegnelsen *eksess kvantestøy*.



**Figur 3:** Et smalt forsterkningsområde fører til eksess kvantestøy. Pilene viser retningen til fotonene i hovedtilstanden. Fra figuren kan man til venstre se at det begrensede forsterknings-området fører til at lasertilstanden blir mye smalere. Dette fører igjen til at denne tilstanden divergerer (man kan si at tilstanden er forandret fra en flat bølgefront til en sterkt divergerende punktkilde). Etter flere runder frem og tilbake i laseren, hvor lyset divergerer mer og mer, inntreer en slags likevekt hvor divergeringen blir holdt igjen av tap gjennom speilene.

I vårt eksperiment behandler vi lasere hvor fotonene bare blir forsterket i et veldig lite område. Vi tilpasser områdets bredde slik at en slags "støyresonans" oppstår hvor vi får veldig mye forsterkning av adjointtilstanden. Ved å gjøre dette, oppnår vi å forsterke spontan emisjon i adjointtilstanden omtrent hundre ganger før den ender opp i hovedtilstanden.



## Curriculum Vitae

---

### Yngve Lien

**Born on the 26th of October 1974 in Trondheim, Norway.**

After receiving my International Baccalaureate at Trondheim Katedralskole in 1994, I started my studies at Imperial College in London, choosing the four-year Masters programme in Physics. As a part of my degree, I spent one year at the Universität Freiburg, where I worked on measuring the energy levels of defects in semiconductor materials using photo induced current transient spectroscopy. In the final year at Imperial College my main study interests were atomic physics and geophysics.

Graduating in 1998, I moved to Leiden in the Netherlands to conduct a Ph.D. in laser physics. Here I studied the intensity fluctuations in lasers with very slow inversion decay. In particular, the extreme oscillations in very small lasers and the excess quantum noise in lasers with both gain and index guiding were of interest. It is this work that is presented here.



## Acknowledgements

---

This thesis would not be complete without a word to everyone who helped during my four years in Leiden.

Firstly, I owe my parents many thanks for putting me into this world and for their support during my studies and then during my Ph.D..

The work presented here would be impossible without the nimble fingers of the instrument makers. Here I would especially like to mention Koos Benning, Jan Post, Ewie de Kuiper and Wilfred van der Geest of the *Fijnmechanische Werkplaats* and Paul Junger from the *LiS*. To extract the data from the measurement apparatus and to give it a presentable form, I was dependent on the computer support of Arno van Amersvoort and Leendert Prevo. Any electronics problems were quickly sorted out by René Overgauw. Our two very efficient secretaries, Anneke Aschoff and Henriette van Leeuwen made sure that the rest of us could continue doing our research.

My roommates Marnix, Peter, Silvania, Erwin and Thijs have all livened up the workplace and have been ready at hand for questions. I came to understand many concepts in discussions with fellow students such as Jorrit, Hayk, Frans, Krista, Gerwin, Alexander, Javier, Jos, Steven and Sumant. I would also like to mention the Post-Docs, Carles, Cyriaque, Sergio and Andrea, who possess impressive knowledge of quantum optics.

I have also worked with two students, Sander de Vries and Elsbeth van der Togt, whose many hours in the lab have given invaluable results. Chapter 7 was done in cooperation with Sumant who has also been more than willing to share his knowledge of computers with me.

Finally, I am grateful to those who have entertained me out of the lab. You know who you are!